Vibrational Sum Frequency Generation Spectroscopy (VSFG) Studies of Organic Electronic Molecules

A DISSERTATION SUBMITTED TO THE FACULTY OF
UNIVERSITY OF MINNESOTA
BY

Zahra Sohrabpour

IN PARTIAL FULFILLMENT OF THE REQUIREMENTS
FOR THE DEGREE OF
DOCTOR OF PHILOSOPHY

Professor Aaron M. Massari, adviser

December 2016

Acknowledgements

My interest in chemistry started with a sixth grade science project in Mrs. Seyedahmadian's class. I started to admire the beauty of it through Mrs. Ghavami and Mr & Mrs. Sadghi's Chemistry classes in high school. And Mr. Karimi's general chemistry lab in college reconfirmed my discussion to major in Chemistry. However, it was Dr. Shafiee's Quantum class that got me thrilled about physical chemistry and Dr. Fattahi's guidance that helped me pursue my education in the US.

When I arrived here, I joined Aaron's group and felt at home. Aaron, I have learned a lot from you both as a scientist and as an advisor. I have learnt from you to treat students as peers and make them feel comfortable to open up. Your endless sense of optimism, your crazy skills with the laser and your unrealistically tight deadlines have always been admirable. I have enjoyed my time in your group immensely and have learnt much more than I thought I ever would.

Tim, taught me how to do SFG and how to think like a scientist. Dan, taught me the rest of the things I know about SFG and everything I know about the OVD chamber and in the process we became very good friends. Audrey and Brynna, were always there for me with their wise advice, smart tips and most importantly their beautiful friendship. Chris, Patrick, Ivan, Courtney, Cindy, Isaac and Spencer thank you for all the great conversations, brain-storming sessions and memories that we have had together.

If it wasn't for my friends, my second family away from home, life would have been very hard. You have inspired me, empowered me, made me laugh, offered your shoulders for a good cry and believed in me when it was hard to believe in myself. Negar, Maral, Sanaz, Pantea, Farzaneh, Roushanak, Narges and Fati thank you! I'm blessed to have you all in my life.

My sister, Zeinab I am so proud of the young woman you have become; kind-hearted, smart and gritty, confident and wise beyond your age. You have been one of my main sources of optimism and positivity. Your words of encouragement mean a world to me. Abbas, my brother, my partner in crime, my room-mate and one of my best friends, I thank you. Our discussions about our projects and science through the years have always been

inspirational and enlightening. Your kind and sensitive heart, your always-smiling face, your patience and perseverance have, are and will always be things I look up to.

Mom and dad, you have inspired me, supported me, trusted me and believed in my power to pursue my dreams. Baba, I love our discussions about science, you are always excited to tell me about the new things you have learned and curiously like to learn about what I have to say. You started your PhD when you were already a father of two, that has always inspired me and made me extra proud of what you did for yourself and us. You set the bar pretty high man! You are my pride, one of my best supporters and critics, my weak-spot and my club-mate! I love you and I thank you. Madar-e-asemani, where I am today as a woman is all because of you. You have always been the wind behind my sails. You bring such love, joy and warmth to my life. You are one of the strongest women I know; you support your family so they can reach their dreams and yet this has not kept you from chasing your own. Every time we talk you make the hard situations sound so amazing with your endless source of optimism. The most important lesson I have learnt from observing you is to stay true to myself. Maman, you are my endless source of inspiration, my rock, my constant and my biggest fan. I love you and I thank you.

Last but not least, my husband, Sadegh. You are the best listener I have known in my life, who thought lawyers could be good listeners?! You hear me so well and make me feel safe to open my heart to you. You have seen me go through tough times and you have supported me through it all, even if that meant tough love from time to time! Your jokes and dead-on impressions make me laugh like none other. In the past two and a half years I have become a happier, more present and kinder person because of you. You are my confidant, my peace, my hope and my funny goofball! Love you.

Dedication

To my parents, Soudabeh and Majid

my siblings, Zeinab and Abbas

& my husband, Sadegh

Abstract

This dissertation describes the application of vibrational sum frequency generation (VSFG) spectroscopy to the study of molecules utilized in organic solar cells (OSC). Two known molecules were chosen for this study, sexithiophene (6T) and fullerene (C_{60}).

In the first study VSFG is employed to probe C_{60} on dielectric surfaces. The SFG activity of this centrosymmetric molecule (theoretically SFG silent) is hypothesized to be from the surface perturbation, resulting an interruption in the symmetry and causing SFG activity. This suggestion is confirmed by experimental VSFG and calculations as well. This study also offers a unique method for estimating surface charge.

In the second study the orientation of 6T molecules at different thicknesses is investigated using a combination of VSFG spectroscopy and atomic force microscopy (AFM). The results confirm previous X-ray studies that, 6T has two very different thickness-dependent orientations. At submonolayer thickness, 6T has an edge-on orientation which changes to an end-on orientation with increase in thickness. Additionally, using VSFG and the thin film interference model it is demonstrated that the orientation of 6T molecules are not the same on the two interfaces, 6T/air and substrate/6T. This study highlights the capability of SFG as a surface probe technique to analyze submonolayer thicknesses.

The last study showcases electrical measurements on organic photovoltaic devices. The effect of different donor and acceptor materials and donor/acceptor modification through positioning a layer of a modifier molecule at the interface is examined.

Table of Contents

Vibrational Sum Frequency Generation of Fullerene on Dielectric Surfaces

Vibrational Sum Frequency Generation Spectroscopy of 6T on glass

Electrical Measurements on Bilayer Heterojunction Organic Solar Cells

List of Tables

Vibrational Sum Frequency Generation of Fullerene on Dielectric Surfaces

Vibrational Sum Frequency Generation of 6T on Glass

Electrical Measurements on Bilayer Heterojunction Organic Solar Cells

List of Figures

Introduction

Vibrational Sum Frequency Generation of Fullerene on Dielectric Surfaces

Vibrational Sum Frequency Generation of 6T on Glass

Electrical Measurements on Bilayer Heterojunction Organic Solar Cells

Introduction

1. Sum Frequency Generation (SFG) Spectroscopy

Sum Frequency Generation (SFG) spectroscopy is a second-order nonlinear optical technique, consisting of two beams with frequencies ω_1 and ω_2 that spatially and temporally overlap to generate an output at the sum of the two frequencies, $\omega_1+\omega_2$. Second Harmonic Generation (SHG) is a special case of SFG, where $\omega_1= \omega_2$.[1] Under the electric-dipole approximation it is shown that this technique is forbidden in media with inversion symmetry.[1] This means SFG is allowed at surfaces and interfaces, since inversion symmetry is necessarily broken at these places. Hence, SFG is a surface-specific technique when the electric-dipole approximation holds and the higher order multipole (specifically quadrupole) contributions or magnetic dipole contributions from the bulk are negligible.[1] This technique has been widely used since 1987 to study the surfaces and interfaces of various samples and reactions.[2]

1.1. A Historical Overview

1.1.1. The Dawn of SHG and SFG

The field of nonlinear optics came into being when the ruby laser was invented. The first demonstration of optical SHG and SGF in a quartz crystal was done by Franken and coworkers.[3] Later in 1962, Armstrong and coworkers worked on the theoretical explanation of wave mixing in nonlinear media.[4] The theory was further improved when proper boundary conditions were taken into account by Bloembergen and Pershan.[5] Later Bloembergen and coworkers worked further on the theory of SHG from media with inversion symmetry where they treated the interface as a thin layer with optical constants

different from the bulk; this is still the basic model followed to this day.[6] For years scientists were more interested to make theoretical predictions about SHG than to use it as a probe for nonlinear optical properties of a medium.[7] However, in 1973, Chen and coworkers published the first paper on SHG as a surface probe technique where they detected Na atomic adsorption on clean Ge under ultrahigh vacuum.[8] Even after this publication, it took a couple of years for the community to take notice of the capability of SHG as a surface probe and its applications.

1.1.2. SFG and SHG as Surface Probe Tools

In 1974, surface-enhanced Raman scattering (SERS) was discovered by Fleischmann and coworkers from pyridine adsorbates on a roughened silver surface.[9] It was shown that with this technique the Raman output could be increased by 10^6 compared to a smooth surface, partly due to local-field enhancement. Raman scattering can be considered a two-photon process, a nonlinear optical effect. At this point a novel idea was born: if one nonlinear optical effect experiences local-field enhancement, so would the others. A follow-up experiment on a roughened silver interface by Chen and coworkers showed that this was indeed the case.[10] In their experiment they showed that SHG could be produced from a bare roughened silver surface, concluding that the enhancement must result from the enhanced local fields. At the same time SHG, like SERS, could be used for detecting adsorption and desorption of molecules on a roughened metal surface and experimental data for this was shown by Chen and coworkers.[11] They also observed adsorption of AgCl and pyridine on silver in an electrochemical cell.[12] The insight that was provided from SERS, that there is local field enhancement at a surface in a nonlinear optical technique,

enabled SHG to be employed as a surface probing tool. Heinz and coworkers expanded this notion by showing that SHG could be applied to obtain spectral and orientational information of organic molecules (rhodamine dyes) adsorbed on a substrate (fused silica).[13]

During the 1980's, several papers were published showing the applicability of SHG as a surface probing technique.[14-17] One of its biggest advantages was that it could be used to probe any surface accessible to light, even buried interfaces. In the SHG measurement the input beam is frequency-doubled, which introduces limitations since the two photons in the process have the same energy. Also the SHG in the IR region has inherently lower signal do this limits SHG to the visible and near-IR region where electronic transitions happen.[7] Yet, in surface sciences, vibrational data is desirable due to its molecular selectivity. Thus, instead of using a single input laser beam, two input beams with different frequencies can be used. This technique is called SFG and can be tuned to study vibrational frequencies (VSFG). The first experimentally successful VSFG data were collected by Zhu and coworkers in 1987 when they managed to collect the vibrational spectrum of the coumarin 504 dye monolayer on quartz.[2]

1.1.3. Broadband SFG

Since the late 1980's SFG spectroscopy has been developing tremendously. In the early days of SFG spectroscopy, picosecond and nanosecond pulses with narrowband laser beams were available for experiments. Thus a spectrum was recorded by tuning the narrowband IR frequency over the spectral window of interest.[1] With the dawn of commercial femtosecond lasers, broadband IR beams started to be utilized. Richter and coworkers[18] and Star and coworkers[19] were the first to report this new scheme. The sum

frequency signal generated from mixing the broadband IR beam with the narrowband visible was recorded in parallel by a CCD after passing through a spectrograph leading to a significant decrease in the data collection time.

1.2. SFG Theory

When a light wave propagates through a material the electric field of the wave applies a force on the electrons of the molecules in the material.[20] If the light is low intensity and non-coherent, then the force is small and in an isotropic medium the induced electric dipole, μ, is given by:

$$\vec{\mu} = \overrightarrow{\mu_0} + \alpha\vec{E} \qquad (1)$$

where μ_0 is the permanent electric dipole of the material, α is the polarizability and E is the electric field of the light wave. This equation holds true for one molecule. If we were to extend this to an ensemble of molecules the induced bulk polarization, $\vec{P}$, would be:

$$\vec{P} = \varepsilon_0\chi^{(1)}\vec{E} \qquad (2)$$

where $\chi^{(1)}$is the macroscopic average of α, known as the first-order or linear susceptibility. ε_0, is the vacuum permittivity.

As the intensity in the light wave is increased the nonlinear terms, which are usually small, should be accounted for and included in the original equation:

$$\vec{\mu} = \overrightarrow{\mu_0} + \alpha\vec{E} + \beta\vec{E}^2 + \gamma\vec{E}^3 \qquad (3)$$

where β and γ are the first and second order hyperpolarizabilities. Again, extending equation 3 to the bulk and averaging over many molecules we have:

$$\vec{P} = \varepsilon_0(\chi^{(1)}\vec{E} + \chi^{(2)}\vec{E}^2 + \chi^{(3)}\vec{E}^3 + \cdots) \qquad (4)$$

$\chi^{(2)}$and $\chi^{(3)}$are the second and third order nonlinear susceptibilities, which are orders of magnitude smaller than $\chi^{(1)}$. The nonlinear term in these equations become significant when the applied electromagnetic field is comparable to the field that is experienced by the electrons in the molecules. These types of fields that cause the nonlinear terms of equation 3 to be significant can be attained with pulsed lasers leading to nonlinear optical techniques.[21]

SFG is a second-order nonlinear process, measuring the second-order susceptibility of the sample. It involves two electric fields, E_1 and E_2, at frequencies ω_1 and ω_2, respectively. So for an SFG process we have:

$$\vec{P}(\omega_{SFG}) = \varepsilon_0 \chi^{(2)} \overrightarrow{E_1}(\omega_1)\, \overrightarrow{E_2}(\omega_2) \qquad (5)$$

$\chi^{(2)}$, the second-order nonlinear susceptibility, is a third-rank tensor with 27 elements. The majority of these elements vanish because of symmetry rules and in the case of SFG only four non zero and independent elements remain.

Figure 1 shows an SFG reflection geometry setup. The solution of the wave equation for this system is:[22]

$$E_p(\omega) = i\left(\frac{2\pi\omega}{c}\right)\Big[L_{xx}(\omega)\chi^{(2)}_{S,xjk}L_{jj}(\omega_1)L_{kk}(\omega_2) + \left(\frac{k_x(\omega)}{k_{1z}(\omega)}\right)L_{zz}(\omega)\chi^{(2)}_{S,zjk}L_{jj}(\omega_1)L_{kk}(\omega_2)\Big] \times E_{1j}(\omega_1)E_{1k}(\omega_2)$$

$$E_s(\omega) = i\left(\frac{2\pi k_1^2(\omega)}{k_{1z}(\omega)\epsilon_1(\omega)}\right) \times L_{yy}(\omega)\chi^{(2)}_{S,zjk}L_{jj}(\omega_1)L_{kk}(\omega_2) \times E_{1j}(\omega_1)E_{1k}(\omega_2) \qquad (6)$$

In the above equation the subscripts, p and s, refer to the beam polarizations. When the electric field of a beam can be resolved into two elements parallel to the plane of incidence

(x-z plane in Figure 1) the beam is p-polarized. If the electric field of the beam can be resolved into an element perpendicular to the plane of incidence it is s-polarized.

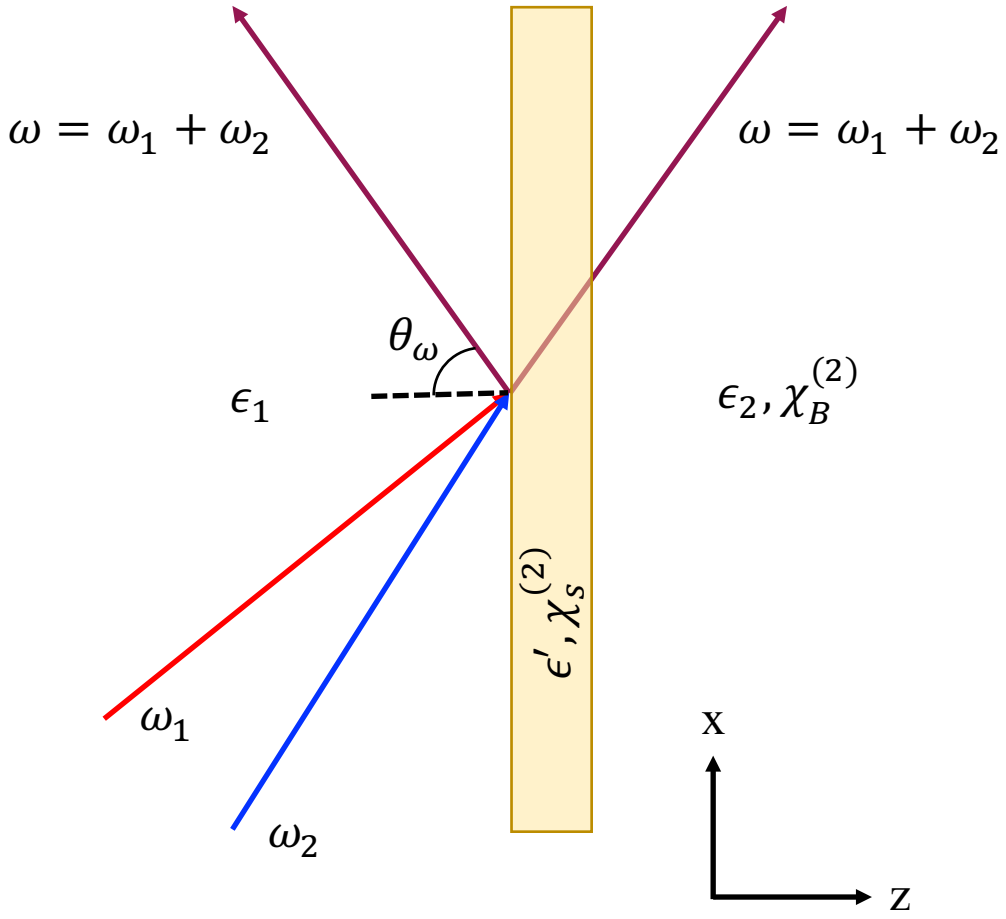

Figure 1. SFG reflection geometry setup. Medium 1 and 2 have dielectric constants of ϵ_1 and ϵ_2, respectively. The interface (dielectric constant of ϵ') has a radiating polarization sheet enclosed in it.

The indices i, j and k are indices for the unit vector of the lab coordinate system (Figure 1). $k_1(\omega)$ is the wave-vector in medium 1 at frequency ω, $E_1(\omega_i)$ the incoming field at frequency ω_i in medium 1. L_{ii} is the transmission Fresnel coefficient for the field. [23]

$$L_{xx}(\omega_i) = \frac{2\epsilon_1(\omega_i)k_{2z}(\omega_i)}{\epsilon_2(\omega_i)k_{1z}(\omega_i)+\epsilon_1(\omega_i)k_{2z}(\omega_i)} \quad (7a)$$

$$L_{yy}(\omega_i) = \frac{2k_{1z}}{k_{1z}+k_{2z}} \quad (7b)$$

$$L_{zz}(\omega_i) = \frac{2\epsilon_1(\omega_i)k_{1z}(\epsilon_2/\epsilon')}{\epsilon_2 k_{1z}+\epsilon_1 k_{2z}} \quad (7c)$$

If $\epsilon_1 = \epsilon' = \epsilon_2$, equation 6 would simplify to a well-known result of a radiating dipole sheet surrounded by a uniform dielectric medium.[23] So the physical image for this equation and in general in the SFG process is that the radiation field is a result of an induced polarization sheet, $\vec{P}(\omega_{SFG})$ from a medium (the interface), between media 1 and 2, with a linear dielectric constant of ϵ'. The induced polarization has contributions from both the interface ($\chi_S^{(2)}$) and the bulk ($\chi_B^{(2)}$). However, in the electric-dipole approximation, if the bulk (medium 2) lacks inversion symmetry its contribution to $\vec{P}(\omega_{SFG})$ is zero and the signal is generated by the interface.

Using equation 6, the SFG output signal can be calculated. If the incoming light beams are pulses with width T and their overlapping cross section at the interface is A then the output SFG signal in units of number photons per pulse is predicted by [23]

$$S(\omega) = \frac{8\pi^3\omega sin^2\theta_\omega}{c^3\hbar[\epsilon_1(\omega)\epsilon_1(\omega_1)\epsilon_1(\omega_2)]^{1/2}} \times \left|e(\omega).\chi_S^{(2)}:e(\omega_1)e(\omega_2)\right|^2 \times I_1(\omega_1)I_1(\omega_2)AT \quad (8)$$

In this equation θ_ω is the reflection angle from the surface normal of the SFG, c is the speed of light, $e(\Omega) = L.\hat{e}(\Omega)$, where $\hat{e}(\Omega)$ is the unit vector for the field polarization at frequency Ω, and $I_1(\omega_i)$ is the incoming laser intensity at frequency ω_i.

This equation can be further simplified to:

$$I(\omega) = \frac{8\pi^3\omega^2 sec^2\theta_\omega}{c^3 n_1(\omega)n_1(\omega_1)n_2(\omega_2)}\left|\chi_{eff}^{(2)}\right|^2 I_1(\omega_1)I_1(\omega_2) \quad (9)$$

where $n_i(\Omega)$ is the refractive index for medium i at Ω. $\chi_{eff}^{(2)}$ is the effective nonlinear susceptibility that expands to give the second term in equation 8. In equation 9 it can easily be seen that SFG intensity depends critically on the effective susceptibility. The second

order susceptibility is a macroscopic average over all the molecules in a given volume, and is related to the molecular hyperpolarizibility, $\beta_{x'y'z'}$, through this equation:

$$\chi^{(2)}_{XYZ} = N \sum_{x',y',z'} \langle R_{Xx'} R_{Yy'} R_{Zz'} \rangle \beta_{x'y'z'} \qquad (10)$$

The X, Y, Z indices refer to the lab coordinates and the x′, y′, z′ indices the molecular coordinates. Also $\langle R_{Xx'} R_{Yy'} R_{Zz'} \rangle$ is the ensemble average of the product of Euler transformation matrices that project the molecular coordinates into the lab frame. This matrix contains three Euler angles, θ, ϕ and ψ, which are shown in Figure 2.

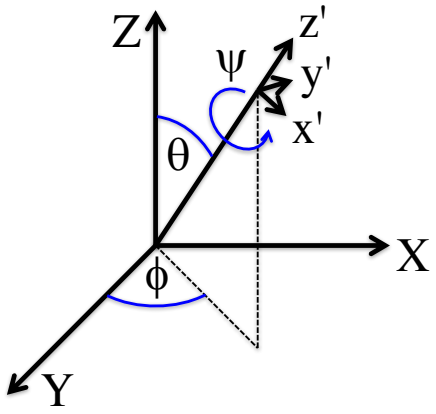

Figure 2. Euler angles, lab and molecular coordinates

The quantum mechanical expression for $\beta_{x'y'z'}$ can be simplified when the electric-dipole approximation holds, neither ω_{Vis} or ω_{SFG} are on resonance with an electronic transition, and ω_{IR}, is on resonance with a vibrational resonance:

$$\beta_{x'y'z'} = -\frac{1}{2\hbar} \sum_k \{ \{ \frac{\langle g_k | \mu_{x',k} | s_k \rangle \langle s_k | \mu_{y',k} | v_k \rangle}{\hbar(\omega_{SFG} - \omega_{sg})} - \frac{\langle g_k | \mu_{y',k} | s_k \rangle \langle s_k | \mu_{x',k} | v_k \rangle}{\hbar(\omega_{Vis} + \omega_{sg})} \} \times \{ \frac{\langle v_k | \mu_{z',k} | g_k \rangle}{\omega_{IR} - \omega_{0,k} + i\Gamma_k} \} \} \qquad (11)$$

In this equation g is the ground state, v the excited vibrational state and s the other state. Γ^{-1}, is the relaxation time for the excited vibrational state and μ the electric dipole

operator.[20] The numerator of the first term on the right hand side of this equation is the Raman transition dipole moment and the numerator of the second term in the bracket is the IR transition dipole moment. This equation shows that a molecule will be SFG active ($\beta_{x'y'z'}$ is nonzero) if it is both Raman and IR active.[21] $\beta_{x'y'z'}$ can be maximized if in the denominator of the second bracket in this equation, $\omega_{IR} = \omega_0$ or when the IR frequency is in resonance with the molecular vibration. When β from equation 11 is replaced into equation 9, it is squared and shows a Lorentzian line shape.

The experimental SFG spectra that are collected are a convolution of the nonresonant susceptibility of the substrate (frequency-independent), $\chi_{NR}^{(2)}$ and the resonant susceptibility, $\chi_R^{(2)}$, of the molecules on the substrate. So the overall signal depends on the amplitude of both these parameters and also the relative phase between these two complex quantities:

$$I_{SFG} \propto \left|\chi_{NR}^{(2)} + \chi_R^{(2)}\right|^2 = \left[\left|\chi_{NR}^{(2)}\right| \exp i\varepsilon + \left|\chi_R^{(2)}\right| exp\ i\delta(\omega)\right] \times \left(\left|\chi_{NR}^{(2)}\right| \exp(-i\varepsilon) + \left|\chi_R^{(2)}\right| \exp[-i\delta(\omega)]\right) = \left|\chi_{NR}^{(2)}\right|^2 + \left|\chi_R^{(2)}\right|^2 + 2\left|\chi_{NR}^{(2)}\right|\left|\chi_R^{(2)}\right| \cos[\varepsilon - \delta(\omega)] \qquad (12)$$

The resonant susceptibility is modeled by a Lorentzian peak shape, as mentioned before. The nonresonant susceptibility is fitted to a single value with amplitude and phase. However, the peak shapes measured in an experimental setup are often directly related to the line width of the laser beams involved.[21] In a broadband IR SFG system the IR peak is shaped as a Gaussian and thus the nonresonant is usually modeled as a Gaussian function.

1.3. Global Thin Film Interference Model for SFG Fitting Routine

When coherent surface-specific techniques are applied to a planar and layered thin film systems, data interpretation can get difficult due to interference effects. The local fields present at the interfaces of interest are affected not only by the geometry of the whole system but also by the emitted fields at those interfaces. Typical approaches to overcome this complication have been techniques to eliminate thin film system dependence completely such as a method of amplitude ratio[24] or experimentally separating the contributing signals.[25-27] Other direct approaches include approximation by simple reflections,[28] modified summation for infinite reflections,[29-33] directly solving it with boundary conditions for a specific sample[34] and transfer matrix methods using Green's functions.[35-38] The current model, which utilizes a fully transfer matrix approach, is more general and inclusive. The transfer matrix presents a direct analytical solution for the fields in an arbitrary layered thin film system.[39-42] This model was built on the assumption that the dipole approximation holds true for the system.

As mentioned before, the second order susceptibility is a third rank tensor with 27 elements, four of which are nonzero and independent under the symmetry rules of SFG; $\chi^{(2)}_{xxz} = \chi^{(2)}_{yyz}$, $\chi^{(2)}_{xzx} = \chi^{(2)}_{yzy}$, $\chi^{(2)}_{zxx} = \chi^{(2)}_{zyy}$ and $\chi^{(2)}_{zzz}$. These elements can be measured using the following experimental beam polarization combinations, respectively: ssp, sps, pss and ppp. It is noteworthy that the ppp polarization does not measure $\chi^{(2)}_{zzz}$ alone, rather a combination of all four susceptibilities. In the polarization combination, the first polarization indicates that of the sum frequency beam, the second one the visible, and the last the IR.

Equations 9 and 10 can be used to write an equation for the SFG signal of a two-layered system using the transfer matrices for the two most common polarization combinations, ssp and sps:

$$I_{ssp} \propto \left|\left(\sum_{v=1}^{3} T_{yyz}\chi_{yyz}^{(2)}\right)\tilde{\tilde{E}}_{Vis,s}\tilde{\tilde{E}}_{IR,p}\right|^2 \propto \left|\left(\sum_{v=1}^{3} T_{yyz}\chi_{yyz}^{(2)}\right)\right|^2 I_{Vis}I_{IR} \quad (13a)$$

$$I_{sps} \propto \left|\left(\sum_{v=1}^{3} T_{yzy}\chi_{yzy}^{(2)}\right)\tilde{\tilde{E}}_{Vis,p}\tilde{\tilde{E}}_{IR,s}\right|^2 \propto \left|\left(\sum_{v=1}^{3} T_{yzy}\chi_{yzy}^{(2)}\right)\right|^2 I_{Vis}I_{IR} \quad (13b)$$

These equations show that the SFG signal intensity depends on an interfacial transfer product factor T_{ijk}. The transfer products report all thin film interference effects. Further detail on how they are constructed can be found elsewhere.[39] The transfer matrix can be constructed with total knowledge of the incoming beam angles, thickness of all the film layers and the optical constants of all the materials in the system.

2. Organic Solar Cells

2.1. A Historical Overview

When a material is exposed to electromagnetic radiation above a certain threshold frequency, the radiation is absorbed and electrons can be emitted; this effect is called the photovoltaic (PV) effect. Becquerel is thought to be the first to discover the photovoltaic effect in 1839.[43] He observed a photocurrent when platinum electrodes, covered with silver bromide or silver chloride, were illuminated in an aqueous solution. Photoconductivity can happen both in organic and inorganic materials. In 1873 and 1876, Smith and Adams, respectively, made the first reports on photoconductivity of selenium.[44-45] However, an efficient inorganic solar cell was not developed until 1954 at Bell Laboratories.[46] It was

based on silicon and had an efficiency of 6%. Nowadays, Si-based solar cells are by far the dominant type of cells used and account for 99% of all PVs.[47]

Pochettino[48] and Volmer,[49] recognized anthracene as the first organic compound to show photoconductivity. In the late 1950s and 1960s organic materials were realized as potential photoreceptors.[50-51] The scientific as well as commercial potential of these materials led to an increased amount of research in photoconductivity and related subjects. In the late 1950s, it was reported that many common dyes, such as methylene blue, had semiconducting properties.[52] These dyes were later among the first organic materials to show photoconductivity. The PV effect was also noticed in many important biological molecules, such as chlorophylls [53] and carotenes.[54]

In the 1980s, polymers (including poly (sulphur nitride)[55-56] and polyacetylene[57]) were first studied in PV cells. However, these simple PV devices based on dyes or polymers yielded limited power conversion efficiencies (PCE) (output power divided by the incident power), typically well below 0.1%. A major development took place in 1986 with Tang's discovery that bringing electron donor and acceptor materials together in one cell could efficiently increase the PCE to 1%.[58] This heterojunction concept has since been applied extensively to a number of donor-acceptor cell types such as dye/dye, polymer/dye, polymer/polymer and polymer/fullerene blends. For example, in 1991 Hiramoto made the first dye/dye bulk heterojuncion PV using co-sublimation.[59] In 1993 Sariciftci made the first polymer/C_{60} heterojunction device[60] and a year later Yu made the first bulk polymer/C_{60} heterojunction PV cell.[61] Yu[62] and Halls[63] independently made the first bulk polymer/polymer heterojunction PV cells later in 1995.

2.2. Principles of Operation

Almost every organic solar cell has a layered structure where the organic light-absorbing material, composed of an electron donor and acceptor, is sandwiched between two electrodes. The donor (acceptor) can either be simply casted on top of the acceptor (planar heterojunction) or a mixture of the donor and acceptor can be sandwiched between the electrodes (ordered or disordered bulk heterojunctions). One of the electrodes should be a material that is semi-transparent to the light, such as indium tin oxide (ITO). However, a thin metal layer can alternatively be used.[64] The other electrode is usually aluminum (or occasionally calcium, magnesium or gold).

Generally, in organic photovoltaic devices, when light is absorbed an electron is promoted from the HOMO of the organic material to its LUMO, forming a bound electron and hole pair called an exciton. For electricity to be generated this exciton must be dissociated. Then, the electron must flow to one electrode while the hole travels to the opposite electrode. In inorganic PVs, electrons and holes are readily separated by the electric field generated by the asymmetrical work functions of the electrodes. The situation in heterojunction OPVs is different. Organic materials have a lower dielectric constant (2-4) than inorganic semiconductors, which leads to a strong Coulomb interaction between the photo-generated electron and hole. This in turn requires a much higher energy input than the thermal energy (kT) to dissociate these excitons (roughly 500 meV).[65] The electric field provided by the asymmetrical work functions of the electrodes is insufficiently strong to break up excitons in organic photovoltaics.[66] To cause better exciton dissociation, researchers had the idea to use materials with different electron affinities and ionization potentials. The electron is accepted by the material with the larger electron affinity and the

hole by the material with a lower ionization potential, at the donor/acceptor (D/A) interface (Figure 3).[47]

2.3. Characteristics of Organic Photovoltaic Devices

One of the standards that is used to measure PV device performance is the current-voltage graph (Figure 4). The definition of electrical power (P) is

$$P=VI \qquad (14)$$

where V and I are the current and voltage. It shows the amount of energy absorbed per one coulomb of charge to move from the positive to the negative terminal in standard labeling. So in the 4th quadrant, the voltage is positive and the current negative which

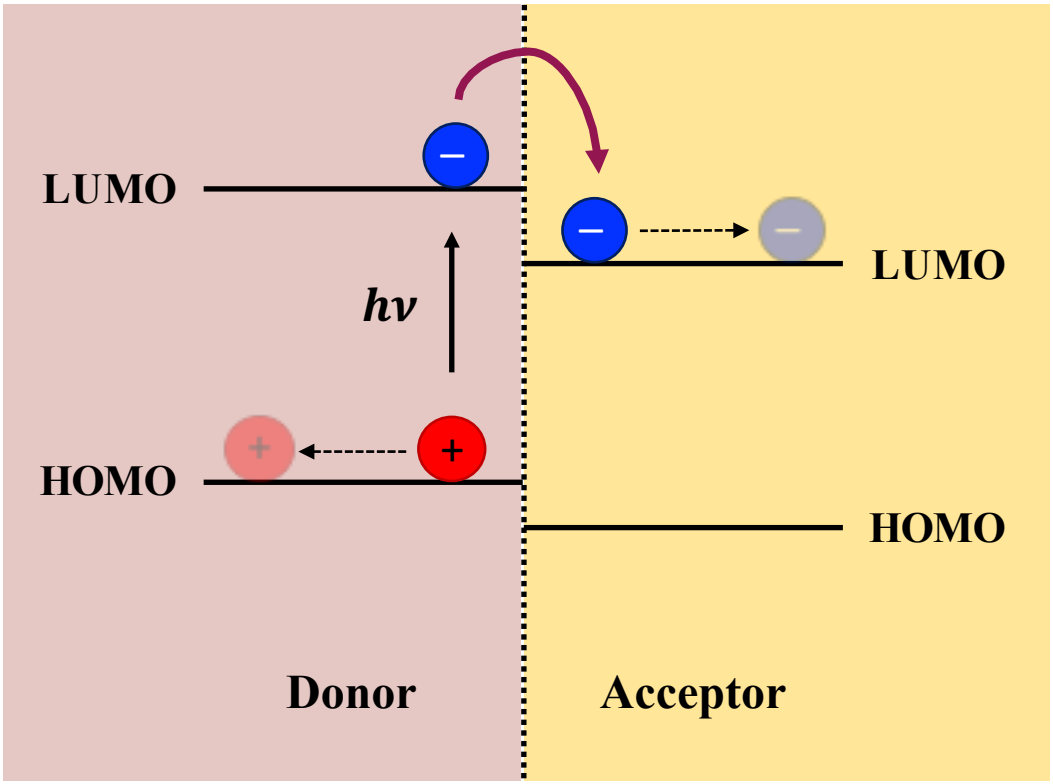

Figure 3. Energy level diagram of a D/A interface showing exciton generation upon photoexcitation and exciton dissociation at the interface due to difference in the LUMO of the two materials.

results a negative power by equation 14 definition. By standard labelling a negative power means that the device is delivering power. Thus the device delivers power both in the 4th and 2nd quadrant, but for convenience current-voltage graphs are usually depicted in the 4th quadrant.[67]

The short circuit current density I_{SC} and the open circuit voltage V_{OC} are two quantities that can be determined experimentally when the cell is illuminated.[65] I_{SC} is the intersection of the I-V graph with the vertical axis and V_{OC} with the horizontal axis. V_{OC} is the maximum voltage difference empirically accessible between the two electrodes. Experimentally, the cell is connected to a voltage source (the resistance of this source is so large that the circuit can be assumed as an open-circuit) and illuminated. The electrons and holes separate and flow to their respective electrodes. At some applied voltage the amount of energy per coulomb is enough to stop the net flow of charges in the circuit. This voltage is called the V_{OC}. I_{SC} is the maximum current that can run through the cell without load. This current is determined by connecting the two electrodes and setting the potential across the cell equal to zero. Then the cell is illuminated and the current is measured. The amount of this current provides information about the charge separation and transport efficiency in the cell. The magnitude of this quantity depends on the illumination strength.

The maximum attainable power from the cell is determined by the product of I_{max} and V_{max}. This maximum power is usually addressed by the fill factor (FF). The FF is defined as:

$$FF = (I_{max}).(V_{max}) \,/\, (V_{OC}).(I_{SC}) \qquad (15)$$

and is typically 0.2-0.95 for photovoltaic devices. A reasonably efficient device has an FF of higher than 0.75.[68] For polymeric heterojunction cells FF is usually 0.25 - 0.6.[69]

Another characteristic of OPVs is the external quantum efficiency (EQE), which is the number of electrons generated per absorbed photons. The external quantum efficiency is the product of the efficiencies of four sequential steps: 1- Photon absorption and thus

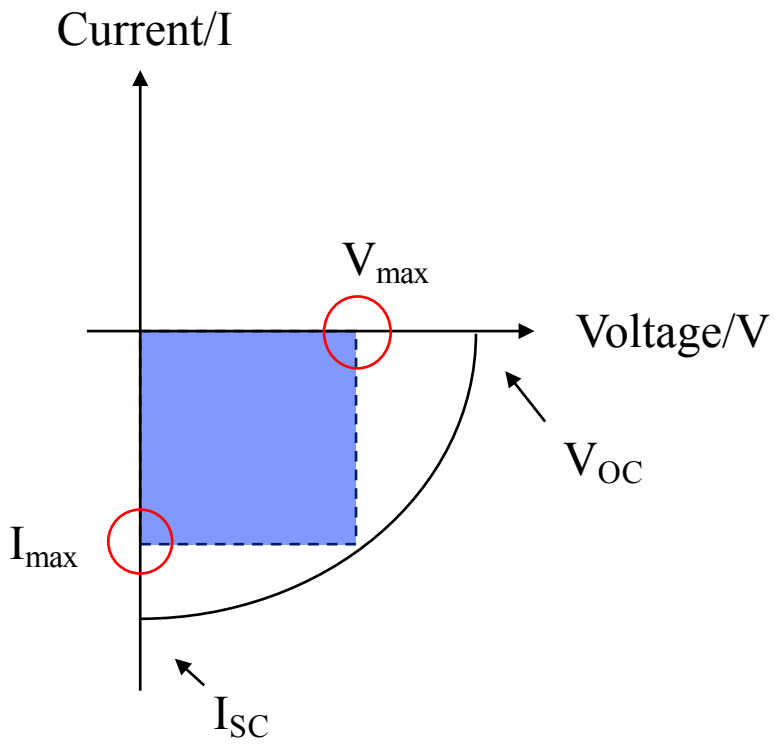

Figure 4. I-V (current-voltage) graph for an OPV cell under illumination

exciton generation (η_A), 2- Exciton diffusion to the D/A interface (η_{ED}), 3- Exciton dissociation by charge transfer at the interface (η_{CT}), 4- Collection of the free charge carriers at the electrodes (η_{CC}). That is:[69]

$$\eta_{EQE} = \eta_A \eta_{IQE} = \eta_A \eta_{ED} \eta_{CT} \eta_{CC} \qquad (16)$$

In this equation η_{IQE}, is the internal quantum efficiency defined as the ratio of the number of carriers collected at an electrode to the number of photons absorbed. For OPVs it has been found that the charge transfer and collection mechanisms at the D/A interface are nearly 100% efficient. However, the exciton diffusion efficiency, the probability of the

generated exciton reaching the interface before recombination (relaxation), is lower. Since in organic materials, the exciton diffusion length (~10nm) is typically shorter than the optical absorbance depth (~100nm), this step is often efficiency limiting.[70]

Another characteristic is the power conversion efficiency (PCE), the power output of the cell divided by the incident light power. PCEs for OPVs are still below 12%[71] whereas those of single crystal Si cells can reach 25%.[72] Not only does the exciton diffusion efficiency have to improve for OPVs to be more efficient but also an effective response over a larger range of the solar spectrum is necessary. Because of the large band gap in organic materials, only a small portion of the incident solar energy is absorbed. A band gap of 1.1 eV (1100 nm) is capable of absorbing 77% of the solar radiation but most of the semiconducting polymers have a band gap of ~2 eV (620 nm). This limits the solar harvesting to 30%.[73]

2.4. Molecular Understanding of the Principles of Operation

From the previous discussion the importance of the D/A interface and its electronic and molecular properties in OPVs is evident. The key to understanding electronic structure at this interface is the difference between the energy of the LUMOs and that of the HOMOs. Experiment-based models have shown that there is a clear relation between V_{OC} and the energy gap between the LUMO of the acceptor (LUMO(A)) and the HOMO of the donor (HOMO(D));[74] V_{OC} increases as the gap widens. The LUMO(A) - HOMO(D) gap can be estimated by the difference between the ionization energy of the donor, IE(D) and the electron affinity of the acceptor, EA(A). The energy step between the LUMO(A) and LUMO(D) at the interface is the difference between their electron affinities (EA),

represented by Δ (Figure 5). The Δ deviates from 0.1eV to 1eV for the organic D/A interfaces.

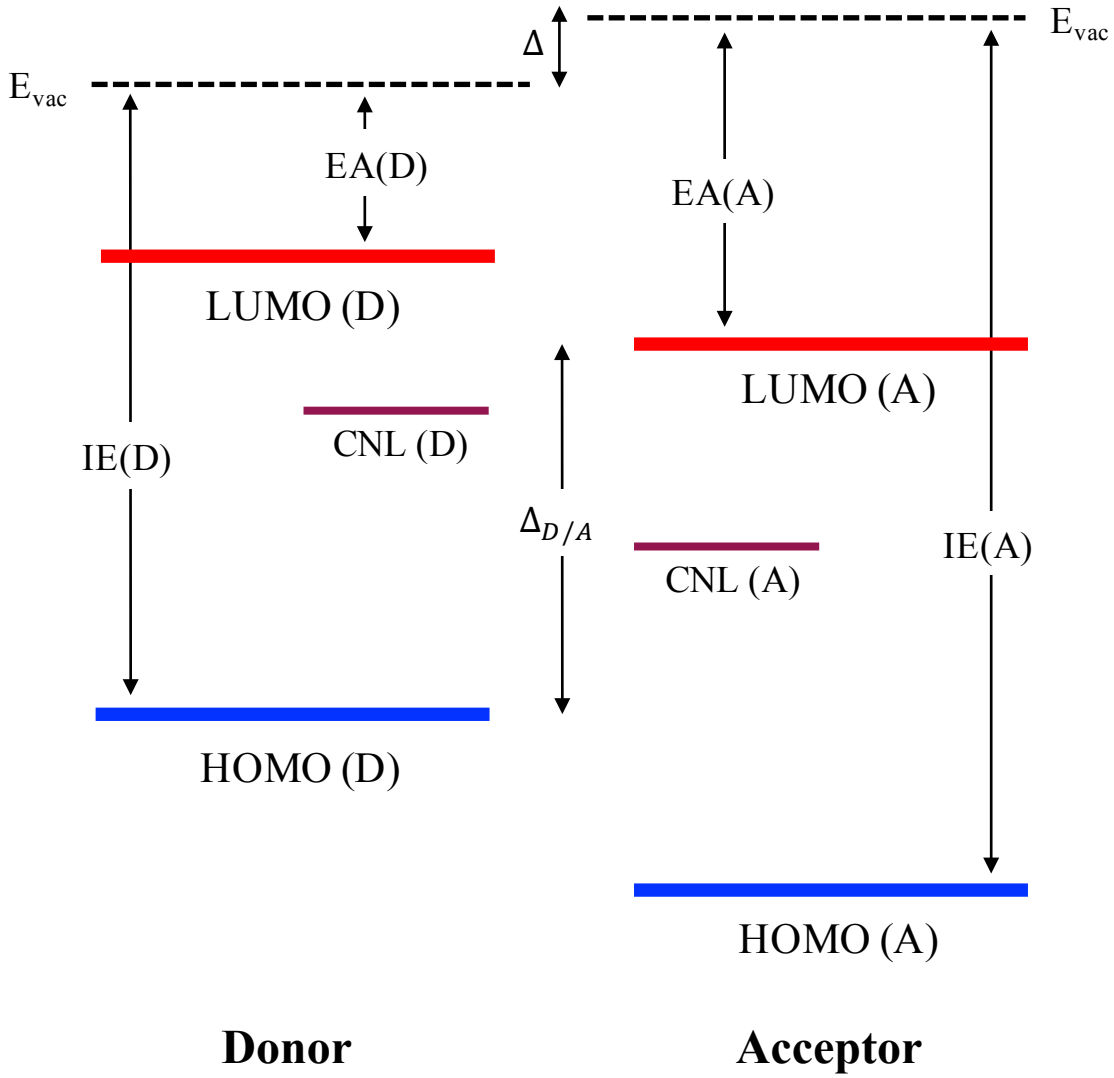

Figure 5. Energy diagram of the D/A interface in an OPV, IE: Ionization energy, EA: Electron affinity and CNL: Charge neutrality level

Excitonic solar cells (OPVs) have a staggered gap electronic configuration. In this arrangement there is little interaction when the two gaps overlap and LUMO(A) is well above HOMO(D), or EA(A) << IE(D). However, When LUMO(A) approaches HOMO(D) they would have a strong interaction with a significant amount of mixing between the filled

states and the empty ones. This results in a charge displacement between the donor and acceptor and thus an interface dipole that would counteract further charge displacement.[75] This dipole forms inherently due to the difference in the chemical nature of these materials and will always be present even with lack of illumination.

A recent approach that helps to provide a rationale for the electronic structure of the interface is based on the minimization of the difference between the charge neutrality levels (CNLs) of the donor and acceptor. The energy level at which the surface is electrically neutral is called, CNL. When the surface is electrically neutral the CNL and the Fermi level are the same, however the Fermi level changes relative to the CNL when surface charge is present.[76] The CNL plays the role of an effective Fermi level.

In this approach the dipole barrier is expressed as: $\Delta = (1 - S) \times (CNL_1 - CNL_2)$, where CNL_1 and CNL_2 are the position of the CNLs of the donor and acceptor with regard to their vacuum levels. S, is an interface screening parameter that is a function of the dielectric of the materials.[77]

3. Conclusion

In this chapter background knowledge about SFG was presented. SFG is constantly used as an important surface-specific nonlinear spectroscopic technique. Also, in this chapter basic information about OPVs was discussed. It was mentioned that in this class of solar cells upon illumination an exciton is generated in the donor phase. This exciton has to diffuse to the D/A interface in order to dissociate and generate electricity. The D/A interface and its molecular characteristics plays a crucial role in powering these solar cells. However, the relationship between molecular structure and cell efficiency is not well

understood. In this regards, we applied SFG to study interfaces of a well-known donor and acceptor, α-sexithiophene (6T) and fullerene (C_{60}). We also attempted to manufacture OPVs and measure their electrical properties by recording current-voltage curves.

Vibrational Sum Frequency Generation Spectroscopy of Fullerene on Dielectric Interfaces

1. Introduction

As described in Chapter 1, vibrational sum frequency generation (VSFG) spectroscopy is a second-order nonlinear optical technique in which the measured signal is forbidden in a centrosymmetric environment within the electric-dipole approximation.[78] This selection rule enables VSFG (and other second-order techniques) to be exquisitely sensitive to the structure of molecules at material interfaces where centrosymmetry breaks down.[21, 79-87] Initially, it was believed that a thin film of centrosymmetric molecules would not be VSFG active, but experiments and calculations have shown that this is not the case.[88-89] This is qualitatively understood as a breaking of the molecular symmetry at material interfaces due to the chemical asymmetry of the interfacial environment.

In exploring the symmetry breaking influence of interfaces, an important case to consider is one of the most symmetric molecules: fullerene (C_{60}). Previous reports have shown that C_{60}, a well-known electron acceptor, shows VSFG activity when deposited on metallic surfaces and when doped by alkali metals.[90-93] In those cases, VSFG activity was attributed to charge transfer of electrons from the metal or dopant, causing molecular symmetry breaking. Similarly, functionalized C_{60} films were shown to be VSFG active, presumably due to the symmetry lowering effect of the functional group.[94-95] However, to date there has been no report of VSFG from C_{60} molecules on insulating surfaces.

In this chapter, we demonstrate that unfunctionalized C_{60} films are in fact VSFG active as well. By calculating the influence of a unidirectional electrostatic perturbation, we are

able to predict the activity differences for two common dielectric substrates, a silicon wafer and a CaF_2 window.

2. Experimental

2.1. Materials

Buckminsterfullerene (C_{60}) was used as received from Sigma-Aldrich (99.5% pure). The water that was used for the RCA and piranha cleaning methods was HPLC grade from Sigma-Aldrich. Hydrogen peroxide used in the RCA and piranha cleaning methods was 30% from Fisher Scientific and was stored in the fridge after opening. Hydrogen peroxide that was stored for longer than six months in the fridge was never used in these experiments due to losing oxidation ability from being reduced. Ammonium hydroxide (NH_4OH), used in the RCA cleaning method, was 28-30% as NH_3 from Macron Chemicals. Hydrochloric acid (HCl), which was used in the RCA cleaning method, was 36.5-38% from BDH Chemicals. Sulfuric acid (H_2SO_4) was 95-98% from BDH Chemicals and used in the piranha cleaning procedure.

2.2. Sample preparation

C_{60} was pressed into a KBr pellet for FTIR measurements. The sample for the Raman measurement was made by preparing a solution of 21 mg of C_{60} in 8 mL of toluene which was stirred on a hot plate at 70 °C for 30 min and then drop-cast on a glass substrate that was previously cleaned by the piranha method.[96] The sample was left on the hot plate to dry for 30 min and then stored under high vacuum overnight for solvent evaporation before Raman measurements.

For VSFG samples, two different substrates were used, a silicon wafer and a CaF_2 window. The silicon wafer substrates had a native oxide layer (SiO_2) of about 2-3 nm thick and were cleaned with a modified RCA method.[97-99] New CaF_2 windows were used without any further cleaning procedures. A C_{60} layer of about 10 nm thickness was vapor deposited under high vacuum with an average pressure of 5×10^{-6} Torr at room temperature.

2.3. Cleaning Procedures

As mentioned previously, for the Raman measurements the glass substrate was cleaned by the piranha method. The piranha cleaning method involves washing the substrate in a 1:1 (H_2SO_4: H_2O_2) solution for 15 minutes followed by three 5 minute washes in DI water. An important point is that the piranha cleaning solution dissolves all organics so none of the containers or tools used in this cleaning process can be plastic.

The modified RCA method involves first blowing the substrate free of particles and then sonication in DI water for 10 minutes. The second step involves 5 minutes of sonication in the first standard clean solution; a 5:1:1 (H_2O: H_2O_2:NH_4OH) solution heated to 80 °C. The next step involves 10 minutes of sonication in DI water followed by another 10 minutes of sonication in the second standard cleaning solution which is a 20:1 (H_2O: HCl) solution. The last step is 10 minutes of sonication in DI water followed by drying the substrate on a hot plate (at about 100 °C) for 30-45 minutes.

2.4. Measurement and Instrumentation

FTIR spectra were collected on a Thermo-Electron Nicolet 6700 spectrometer, with a resolution of 1.0 cm^{-1} and an average of 16 scans.

Raman spectra were collected on a home-built Raman microscope using a 785 nm diode

laser (Innovative Photonics) in 70:30 geometry and an Olympus 10× Plan objective to focus the scattered output onto a Princeton Instruments Acton Pro 2500i spectrograph and finally to a Princeton Instruments PIXIS 400BX detector.

For the VSFG instrument, laser pulses from a Ti: Sapph laser (Spectra-Physics, 800 nm, 40 fs pulse duration fwhm, 30 nm bandwidth fwhm, 600 mW) were regeneratively amplified and used to pump an optical parametric amplifier (Spectra-Physics, OPA-800C) at a repetition rate of 1 kHz. In the OPA, a near-IR signal and idler were generated by a β-barium borate (BBO) crystal and then difference frequency mixed in a silver gallium sulfide ($AgGaS_2$) crystal to generate tunable pulses in the mid-IR region, with roughly 175 cm^{-1} of bandwidth at fwhm. To produce the visible pump beam, the unconverted 800 nm light from the OPA was spectrally narrowed in a 4f pulse shaper to about 1nm fwhm centered at 800.75 nm with pulse energies of 4 μ J at the sample.

The mid-IR (centered at 1480 cm^{-1}) and visible pulses were focused onto the sample surface, and the resulting VSFG signal was collected in a reflective setup using a pair of 60° off –axis parabolic mirrors. Spectra were collected in the ssp and sps polarization combinations (s = VSFG signal, s = visible beam, and p = mid-IR beam polarizations). VSFG spectra for each sample were collected on three different spots, using an average of five exposures, where each exposure was 20 and 30 min for ssp and 30 and 45 min for sps polarization combinations on silicon wafer and CaF_2 substrates, respectively. Between every spot a reference VSFG spectrum was collected from a zinc oxide sample that was prepared by atomic layer deposition on the same substrate as the respective sample. The spectra from the samples were then normalized by these reference spectra.

3. Computation

Computations were carried out on Gaussian®09 software,[100] using the DFT model with the B3LYP functional and 6-31G(d) basis set. This basis was chosen for expediency and since there is literature precedent showing good agreement between theory at this level and experimental spectra.[101-102] Limited calculations were performed at the 6-311G(d) level and gave better frequency agreements to experiment but showed the same trends in IR and Raman activity, which are the focus of this chapter.

For these calculations, a C_{60} molecule was placed in the vicinity of a virtual negative (-1) or positive (+1) point charge. The distance was fixed between the virtual charge and the farthest six-membered ring (on the far side of the C_{60} molecule), and the molecule was geometrically optimized. Then the output file for the geometry optimization was used to perform a separate frequency calculation (including Raman) with the keyword iop(7/33 = 1). Several calculations with different charge-molecule distances were performed (the distances used to present the results below refer to those between the charge and the closest six-membered ring).

3.1. Finding SFG Response from Computation Results

The VSFG intensity is directly related to the square of the effective second-order susceptibility, as seen previously in Chapter 1: [103]

$$I(\omega) = \frac{8\pi^3\omega^2 sec^2\beta}{c_0^3 n_1(\omega)\, n_1(\omega_1) n_2(\omega_2)} \left|\chi_{eff}^{(2)}\right|^2 I(\omega_1) I(\omega_2) \propto \left|\chi_{eff}^{(2)}\right|^2 I_{vis} I_{IR} \qquad (1)$$

where ω is the sum frequency of the IR and visible beams (1 and 2), β is the angle of the

sum frequency with the surface normal, $n_i(\omega)$ is the refractive index of medium "i" at frequency ω. $I(\omega_1)$ and $I(\omega_2)$ are the intensities of the input beams (IR and visible).

For the polarization combinations used in this study (ssp and sps) the effective second-order susceptibilities are [103]

$$\chi^{(2)}_{eff,SSP} = L_{YY}(\omega)L_{YY}(\omega_1)L_{ZZ}(\omega_2)sin\beta_2\chi_{YYZ} \propto \chi^{(2)}_{YYZ} \qquad (2.1)$$

$$\chi^{(2)}_{eff,SPS} = L_{YY}(\omega)L_{ZZ}(\omega_1)L_{YY}(\omega_2)sin\beta_1\chi_{YZY} \propto \chi^{(2)}_{YZY} \qquad (2.2)$$

where $L_{ii}(\omega_j)$ is the tensorial Fresnel factor at ω_j. The macroscopic second-order susceptibility is an ensemble average of the microscopic hyperpolarizibility via Euler transformation [103]

$$\chi^{(2)}_{XYZ} = N\sum_{x',y',z'}\langle R_{Xx'}R_{Yy'}R_{Zz'}\rangle\,\beta_{x'y'z'} \qquad (3)$$

The X, Y, Z indices refer to the lab coordinates and the x′, y′, z′ indices the molecular coordinates. Also $\langle R_{Xx'}R_{Yy'}R_{Zz'}\rangle$ is the ensemble average of the product of Euler transformation matrices that project the molecular coordinates into the lab frame. This matrix contains three Euler angles, θ, ϕ and ψ, which are shown in Figure 1.

For ssp polarization combination and with the assumption that the film has a random

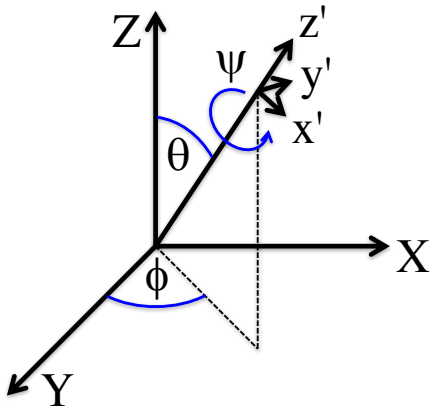

Figure 1. Euler angles, lab and molecular coordinates

orientation distribution within the surface plane (Φ), equation (3) changes to:[104]

$$\chi_{XXZ} = \frac{1}{2}N\times\{\langle sin^2\theta cos\theta\rangle(\beta_{z'z'z'}) + \langle cos\theta\rangle(\beta_{x'x'z'} + \beta_{y'y'z'}) - \langle sin^2\theta cos\theta sin^2\psi\rangle(\beta_{y'y'z'} + \beta_{y'z'y'} + \beta_{z'y'y'}) - \langle sin^2\theta cos\theta cos^2\psi\rangle(\beta_{x'x'z'} + \beta_{x'z'x'} + \beta_{z'x'x'}) + \langle sin^2\theta cos\theta sin\psi cos\psi\rangle(\beta_{x'y'z'} + \beta_{x'z'y'} + \beta_{y'x'z'} + \beta_{y'z'x'} + \beta_{z'x'y'} + \beta_{z'y'x'}) + \langle sin\theta sin\psi\rangle(\beta_{y'y'y'} + \beta_{x'x'y'} - \beta_{y'z'z'} - \beta_{z'y'z'}) + \langle sin\theta cos\psi\rangle(-\beta_{x'x'x'} - \beta_{y'y'x'} + \beta_{x'z'z'} + \beta_{z'x'z'}) + \langle sin^3\theta sin\psi\rangle(-\beta_{x'x'y'} - \beta_{x'y'x'} - \beta_{y'x'x'} + \beta_{y'z'z'} + \beta_{z'y'z'} + \beta_{z'z'y'}) + \langle sin^3\theta cos\psi\rangle(\beta_{x'y'y'} + \beta_{y'x'y'} + \beta_{y'y'x'} - \beta_{x'z'z'} - \beta_{z'x'z'} - \beta_{z'z'x'}) + \langle sin^3\theta sin^3\psi\rangle(-\beta_{y'y'y'} + \beta_{x'x'y'} + \beta_{x'y'x'} + \beta_{y'x'x'}) + \langle sin^3\theta cos^3\psi\rangle(\beta_{x'x'x'} - \beta_{x'y'y'} - \beta_{y'x'y'} - \beta_{y'y'x'})\} \quad (4.1)$$

And for sps it transforms into:[104]

$$\chi_{XZX} = \frac{1}{2}N\times\{\langle sin^2\theta cos\theta\rangle(\beta_{z'z'z'}) + \langle cos\theta\rangle(\beta_{x'z'x'} + \beta_{y'z'y'}) - \langle sin^2\theta cos\theta sin^2\psi\rangle(\beta_{y'y'z'} + \beta_{y'z'y'} + \beta_{z'y'y'}) - \langle sin^2\theta cos\theta cos^2\psi\rangle(\beta_{x'x'z'} + \beta_{x'z'x'} + \beta_{z'x'x'}) + \langle sin^2\theta cos\theta sin\psi cos\psi\rangle(\beta_{x'y'z'} + \beta_{x'z'y'} + \beta_{y'x'z'} + \beta_{y'z'x'} + \beta_{z'x'y'} + \beta_{z'y'x'}) + \langle sin\theta sin\psi\rangle(\beta_{y'y'y'} + \beta_{x'y'x'} - \beta_{y'z'z'} - \beta_{z'z'y'}) + \langle sin\theta cos\psi\rangle(-\beta_{x'x'x'} - \beta_{y'x'y'} + \beta_{x'z'z'} + \beta_{z'z'x'}) + \langle sin^3\theta sin\psi\rangle(-\beta_{x'x'y'} - \beta_{x'y'x'} - \beta_{y'x'x'} + \beta_{y'z'z'} + \beta_{z'y'z'} + \beta_{z'z'y'}) + \langle sin^3\theta cos\psi\rangle(\beta_{x'y'y'} + \beta_{y'x'y'} + \beta_{y'y'x'} - \beta_{x'z'z'} - \beta_{z'x'z'} - \beta_{z'z'x'}) + \langle sin^3\theta sin^3\psi\rangle(-\beta_{y'y'y'} + \beta_{x'x'y'} + \beta_{x'y'x'} + \beta_{y'x'x'}) + \langle sin^3\theta cos^3\psi\rangle(\beta_{x'x'x'} - \beta_{x'y'y'} - \beta_{y'x'y'} - \beta_{y'y'x'})\} \quad (4.2)$$

in both equations, N is the number density of the chromophores.

The microscopic hyperpolarizibility is related to the polarizability and the electric dipole moment via:

$$\beta_{ijk} \propto \frac{\partial \alpha_{ij}}{\partial Q_q} \frac{\partial \mu_k}{\partial Q_q} \qquad (5)$$

In this equation α_{ij} is the polarizability, μ_k is the electric dipole moment, and Q_q is the normal mode coordinate for the q-th mode.

From the Gaussian frequency calculation outputs, including the iop(7/33 = 1) keyword, one can find the derivative of polarizabilities and the electric dipole moments with respect to the normal mode coordinate. Using equations 4.1 and 4.2 and then equations 2.1 and 2.2, one can calculate $\left|\chi_{eff}^{(2)}\right|^2$, which is proportional to the VSFG intensity. We note that the normal mode coordinates from Gaussian are mass-weighted, thus the hyperpolarizabilities obtained in this work are not absolute.

3.2. Choosing Euler Angles

To be able to calculate the polarizability in the lab frame from the molecular frame the correct Euler angles are needed. For a uniaxial film one can assume there is random orientation distribution within the surface of the film. With this assumption the average over functions containing ϕ (in-plane rotation angle, Figure 1) will be $\langle sin^2\phi\rangle = \langle cos^2\phi\rangle = 1/2$ and $\langle sin\emptyset cos\emptyset\rangle$=0, which can be separated and the hyperpolarizibility equations can be simplified into equations (4.1) and (4.2). It was found that the calculated SFG spectra are insensitive to ψ (Figures 2 and 3), so this was maintained at zero.

Analysis of our calculations shows that the A_g mode (centered at 1469 cm^{-1}) has a transition dipole that always orients along a line connecting the virtual point charge to the

center of the C_{60}. For our simulations, this means that this mode is always oriented perpendicular to the substrate plane. Thus, in the calculation model, where the distance and position of the virtual point charge is fixed from the molecule, θ is always zero.

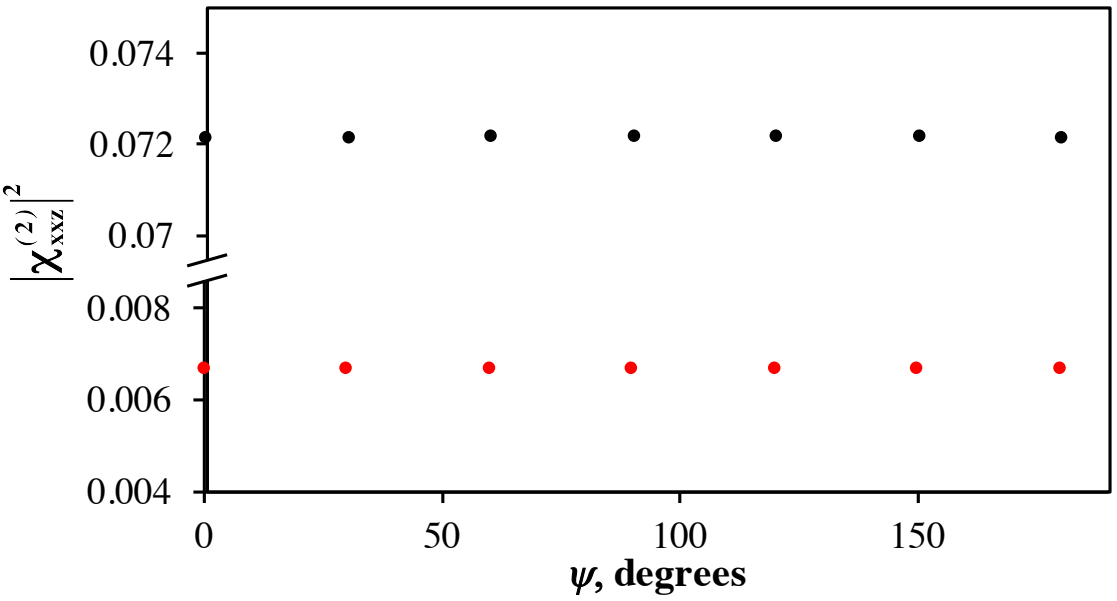

Figure 2. $|\chi^{(2)}_{xxz}|^2$ as a function of ψ angle for the F_{1u} (black) and A_g (red) modes. Virtual charge at a distance of 5 Å.

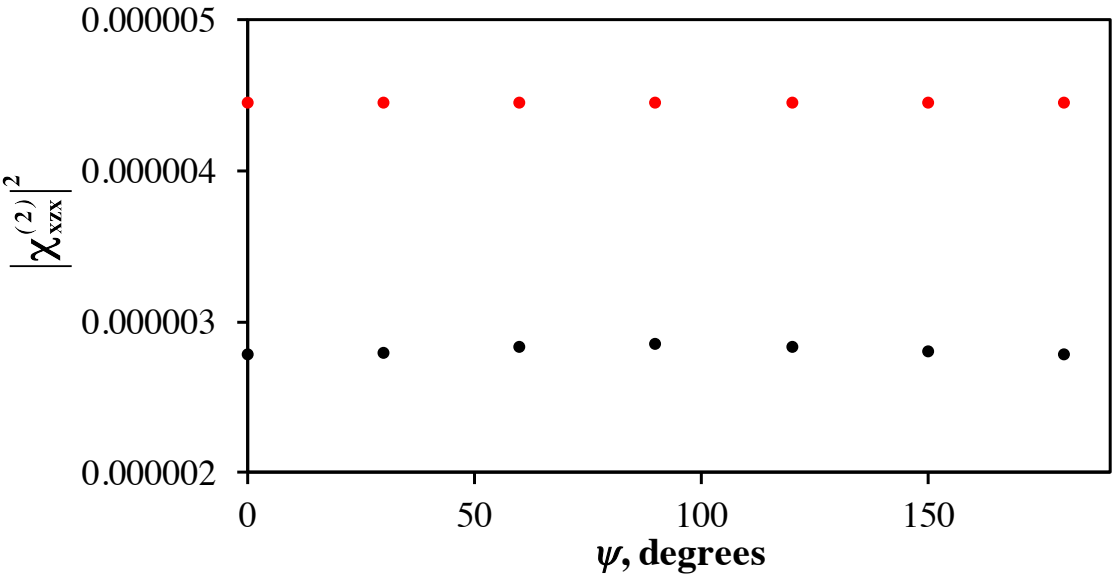

Figure 3. $|\chi^{(2)}_{xzx}|^2$ as a function of ψ angle for the F_{1u} (black) and A_g (red) modes. Virtual charge at a distance of 5 Å.

4. Results and Discussion

4.1. IR and Raman Spectra of Fullerene

VSFG activity requires both IR and Raman activities;[21] therefore, we begin by examining the linear vibrational spectroscopies of fullerene thin films. Figure 4a shows the FTIR and Raman spectra collected for C_{60} in a KBr pellet and a drop-cast film on glass, respectively. The IR spectrum exhibits a single peak in this range at 1429 cm^{-1}, as has been reported previously.[105-106] This transition has been previously assigned in the literature as the F_{1u} vibrational mode.[107-110] The corresponding IR spectrum for gas phase C_{60} as calculated by DFT is shown in Figure 4b and exhibits a single strong peak at 1421 cm^{-1}.

The frequency axis in the lower frame was scaled by a scale factor of 0.9613 based on the literature report for our method and basis set.[111] The focus here is not on the accuracy of the frequency correction between experiment and theory rather on the relative activity of specific modes. Only the F_{1u} mode is predicted to be IR-active in the gas phase, and this is confirmed by the experimental spectrum in the condensed phase in Figure 4a.

In the measured Raman spectrum (Figure 4a) there is a pronounced peak at 1469 cm^{-1}, which is consistent with previously reported values for the A_g pentagonal pinch mode. [107, 112-113] The Raman spectrum was generated with a near-IR pump source (800 nm) to remain off-resonance with the electronic absorption in fullerene that has been shown to drive a structural transition that red-shifts the A_g mode.[114-116] This is also the same wavelength as the visible pump beam in the VSFG instrument used below.

The calculated Raman spectrum in Figure 4b also shows a single peak at 1465 cm^{-1}, which is again slightly red-shifted from the experimental value but consistent with the

experimental result. On the basis of the calculated IR and Raman spectra, one would predict little to no VSFG activity for the isolated highly symmetric C_{60} molecule. Clearly the gas-phase calculations do not capture the symmetry breaking that occurs at the interfaces of a film of C_{60} since VSFG spectra have been reported by others.

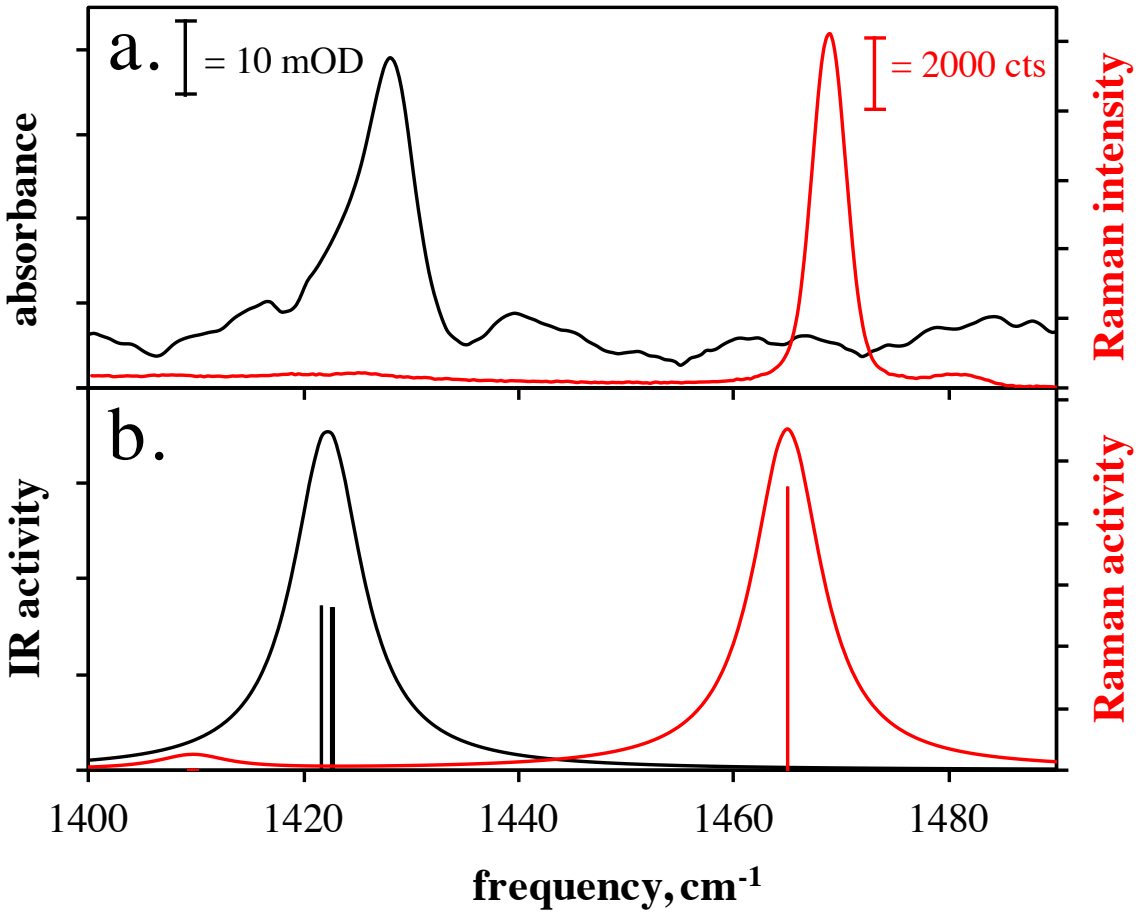

Figure 4. (a) Experimental IR absorption (black) and Raman (red) spectra for KBr pellet and drop-cast C_{60} thin films deposited on glass, respectively, and (b) calculated gas phase IR (black) and Raman (red) spectra in which stick spectra have been artificially broadened by a $4cm^{-1}$ (HWHM) Lorentzian line shape.

4.2. Experimental VSFG Spectra

Figure 5a shows the VSFG spectra collected in the current study with an ssp polarization combination on native oxide (SiO_2) over silicon and on a CaF_2 substrate. The spectra on dielectric substrates are quite different from those reported by others on metal surfaces,[90-

[93] and the spectrum on CaF_2 is also surprisingly different from that of the SiO_2 sample. In both cases, the F_{1u} and A_g modes exhibit some VSFG activity, but the A_g mode is notably stronger on the CaF_2 surface, such that the ratio of the peaks is switched between these two substrates. Spectra reported on metal substrates unanimously showed only a single peak in this frequency range, which was assigned as the A_g mode.[90-93]

The ssp polarization combination probes the out-of-plane tensor element of the second order susceptibility, $\chi^{(2)}$; therefore, the VSFG spectra indicate a fundamental difference in the mode activities orthogonal to the substrate plane. On the other hand, the sps polarization combination reports on the mode activities in the plane of the film, and Figure 5b shows that the spectra of C_{60} on SiO_2 and CaF_2 are qualitatively similar. It has been shown,[94] and our data support that the transition dipole for the A_g mode is perpendicular to the substrate. This means that the transition dipole is parallel to the "z -axis", and thus this peak cannot be seen in the sps polarization combination in Figure 5b, where the IR is s-polarized.

In order to quantify the spectral differences in Figure 5, $\chi^{(2)}$should be determined for each mode by taking into account multilayer interference during propagation of all three beams.[117-120]

For both sample types, interface 1 is the air/C_{60} interface. The silicon substrate has a native SiO_2 overcoating that is in contact with C_{60} (C_{60} /SiO_2 = interface 2), leaving the SiO_2/Si junction as interface 3. For the sample on CaF_2 the CaF_2 /C_{60} is interface 2.

4.2.1. Finding the Frequency-dependent Refractive Indices

The frequency-dependent complex refractive index for silicon was found by fitting experimental data to a three-term Sellmeier equation.[121] SiO_2 and CaF_2 real and imaginary

refractive indices (from 1200 to 1700 cm^{-1})[122] were fitted to a polynomial equation, which

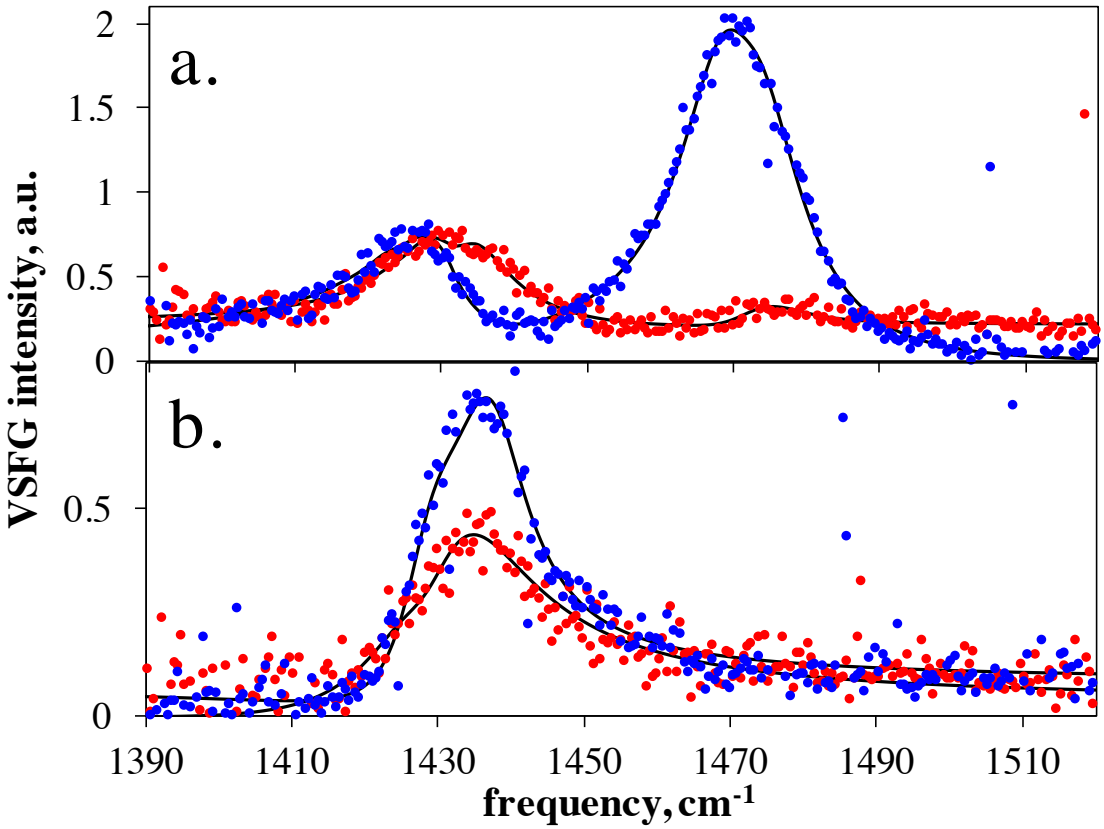

Figure 5. Experimental VSFG spectra of C60 on silica (red markers) and CaF2 (blue markers) overlaid with the multilayer interference fits (black line) for the (a) ssp polarization combination and (b) sps polarization combination.

was applied in the multilayer model. The experimental dielectric spectrum of C_{60}[123] and the Kramers−Kronig relation[124] were used to calculate the real and imaginary parts of the refractive index.

To find the refractive index of C_{60} the amplitude of the imaginary component of the refractive index was estimated from previous experimental data for the dielectric function of fullerene. [123] The complex dielectric function:

$$\varepsilon(\omega) = \varepsilon_1(\omega) + i\varepsilon_2(\omega) \qquad (6)$$

is related to the refractive index by:

$$\varepsilon_1 + i\varepsilon_2 = (n + ik)^2 \qquad (7)$$

The components of the refractive index can be solved as:

$$n = \sqrt{\frac{\varepsilon_1 + \sqrt{\varepsilon_1^2 + \varepsilon_2^2}}{2}} \qquad (8)$$

$$k = \sqrt{\frac{-\varepsilon_1 + \sqrt{\varepsilon_1^2 + \varepsilon_2^2}}{2}} \qquad (9)$$

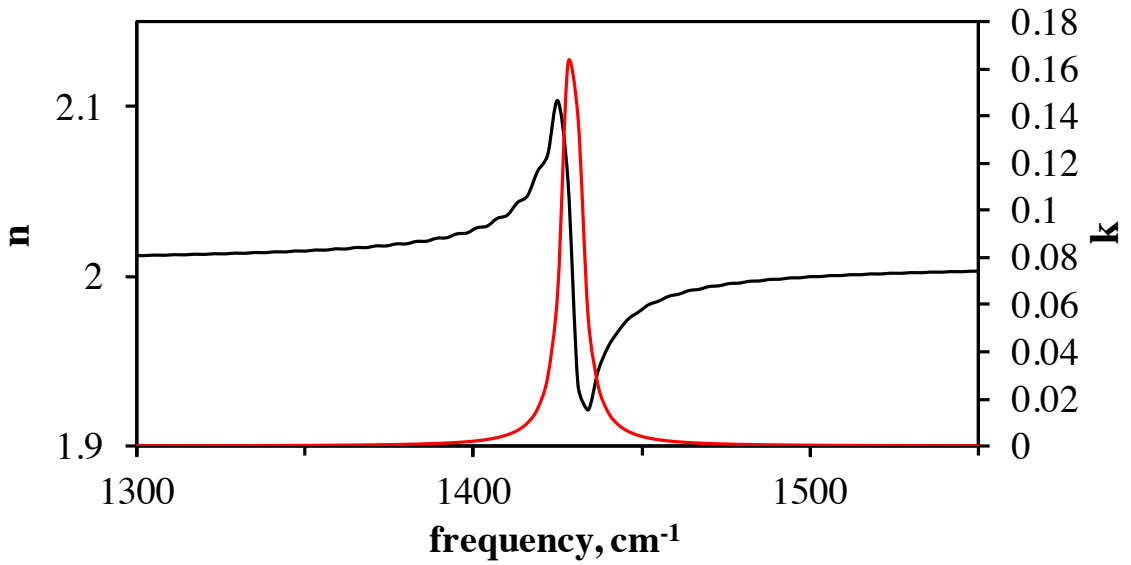

Figure 6. Real (black) and imaginary (red) components of C_{60} complex refractive index.

Specifically, the peak value for the imaginary part of the dielectric function was read from Figure 1b in reference 2 between 1200 and 1550 cm^{-1}.[123] This peak value was converted to k using Equation 9. A Lorentzian lineshape was created with this k value as its amplitude and a HWHM matching that of the experimental IR spectrum (Figure 4a). The real component was calculated from the imaginary component using the Kramers-Kronig relation. [124] Figure 6 shows how the real and imaginary components of the refractive index vary with frequency.

4.2.2. Experimental VSFG Spectra Fit Results

The global fitting routine, that was explained in Chapter 1, was used to analyze the VSFG spectra in Figure 5. Since interface 1 was the same for both samples (air/C_{60}) the frequency, amplitudes, and line widths (HWHM) of both resonances (F_{1u} and A_g) at this interface were fixed to be the same between both substrate types. The parameters for buried interface resonances (C_{60}/SiO_2 or C_{60}/CaF_2) were adjusted independently. The best fit parameters for the ssp VSFG spectra are compiled in Table 1. The sps and nonresonant background fit parameters are also given in Tables 2 and 3.

Table 1. Best fit parameters to VSFG data with ssp polarization combination (Figure 5a).

		$\nu = F_{1u}$			**$\nu = A_g$**		
surface	**interface**	**amplitude $\times 10^4$**	**frequency cm^{-1}**	**HWHM cm^{-1}**	**amplitude $\times 10^4$**	**frequency cm^{-1}**	**HWHM cm^{-1}**
SiO_2	outer	2.668 (+3/-2)	1430.8 (+3/-3)	5.25 (+4/-3)	-2.586 (+2/-5)	1471.3 (+2/-3)	7.86 (+?/-3)
	inner	-4.051 (+2/-3)	1432.4 (+3/-3)	6.26 (+3/-3)	-6.870 (+4/-4)	1474.7 (+7/-17)	7.95 (+8/-5)
CaF_2	outer	2.668 (+3/-2)	1430.8 (+3/-3)	5.25 (+4/-3)	-2.586 (+2/-5)	1471.3 (+2/-3)	7.86 (+?/-3)
	inner	-3.188 (+2/-5)	1429.8 (+3/-3)	7.17 (+3/-3)	0.702 (+2.5/-0.8)	1471.7 (+3/-3)	5.58 (+3/-6)

Table 2. Best fit parameters to VSFG data with sps polarization combination (Figure 5b).

		$\nu = F_{1u}$		
surface	**interface**	**amplitude $\times 10^4$**	**frequency cm^{-1}**	**HWHM cm^{-1}**
SiO_2	outer	0.978 (+0.5/-1.3)	1429.7 (+4/-4)	4.53 (+5/-3)
	inner	-6.304 (+2/-2)	1431.0 (+3/-3)	8.17 (+4/-3)
CaF_2	outer	0.978 (+0.5/-1.3)	1429.7 (+4/-4)	4.53 (+5/-3)
	inner	-1.499 (+0.6/-0.8)	1436.5 (+4/-3)	5.97 (+3/-2)

Table 3. Best fit parameters to non-resonant background in VSFG data with ssp and sps polarization combination (Figure 5).

surface	polarization	A_{NR}	Φ_{NR}
SiO_2	ssp	0.0149014 (+0.002/-0.002)	-6.51931 (+0.4/-1.1)
	sps	-0.00796245 (+0.002/-0.002)	6.4766 (+0.3/-0.3)
CaF_2	ssp	-0.0065535 (+0.003/-0.003)	-8.15306 (+1.1/-0.7)
	sps	0.00773902 (+0.002/-0.002)	16.3631 (+0.6/-0.9)

The VSFG spectra obtained by this fitting process are overlaid on the data points in Figure 5, and the agreement is excellent. The first salient point from the parameters in Table 1 is that the relative amplitudes of $\chi^{(2)}$ from the modes at outer and inner interfaces are on the same order of magnitude. The negative sign convention on the amplitudes indicates the polar order relative to the same mode on the other interface. This does not indicate that a mode is pointed "up" or "down", just that this transition is opposite in phase to the transition with which it is interfering. This demonstrates that macroscopic centrosymmetry breaks down even at the air/C_{60} interface and that the spectra are well modeled by inner and outer resonances that interfere at the electric field level. A common rationalization of such behavior invokes bulk and/or interfacial quadrupolar moments; however, we show by this modeling and the calculations that follow that even within the dipole approximation both interfaces are VSFG-active. Furthermore, our previous work has shown that the quadrupolar contributions should be quite small for films of this thickness.[120]

A qualitative look at the VSFG spectra in Figure 5 suggests a ratio of smaller than one for the F_{1u} to A_g modes on a CaF_2 substrate, but taking into account interference effects

through the multilayer model the results turn out to be very different. In fact, although the A_g mode is qualitatively stronger in the VSFG spectrum on CaF_2, Table 1 shows that this resonance is actually smaller than the same mode at the buried interface on SiO_2. On the other hand, the F_{1u} mode appears similar in magnitude in Figure 5, and the fit parameters are comparable. This again highlights the importance of properly modeling beam propagation into and out of the sample in VSFG measurements. The frequency separation and the relative phase of each resonance play important roles in the interference of the inner and outer modes that make it difficult to qualitatively interpret the spectra.

4.3. Calculated IR, Raman and VSFG Spectra

Fullerene in the gas phase should have no VSFG activity for either of these vibrational modes; thus, we must conclude that the interactions with the substrate and air break the symmetry of the molecule and introduce some IR and/or Raman activity where there previously was none. Considering that the interfacial C_{60} molecules are perturbed from one side by the dielectric substrate, we used DFT calculations to investigate the role of a unidirectional electrostatic perturbation on the C_{60} structure and mode activities. Virtual negative and positive charges were placed at a range of distances from a C_{60} molecule. For each calculation, the distance between the charge and the molecule was maintained while the molecule was geometrically optimized. The output file of this optimization was then used in frequency calculations to determine the Raman and IR activities of the vibrational modes.

Figure 7 shows the calculated IR and Raman spectra for selected distances between a virtual negative charge and the C_{60} molecule (shown in different colors). The negative point

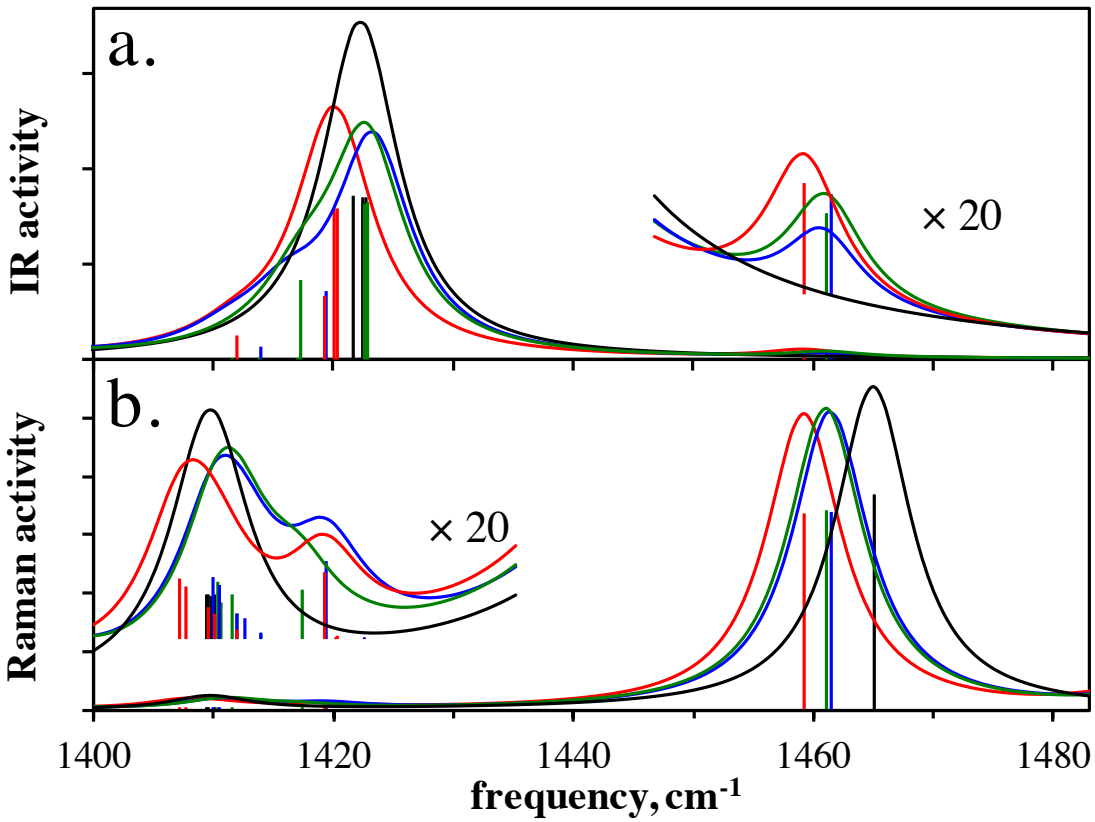

Figure 7. Calculated (a) IR and (b) Raman spectra for C60 with a virtual negative charge at selected distances (black = no charge, red = 3Å, blue = 6 Å, green = 20 Å). Calculated stick spectra have been artificially broadened by 4 cm^{-1} (HWHM) Lorentzian line shapes.

charge causes the IR activity to redistribute among modes that are predicted with F_{1u} symmetry (note changes in stick spectra), but more importantly, there is a gain in IR activity in the A_g mode region. Conversely, in the calculated Raman activity we find that the F_{1u} mode at 1420 cm^{-1} gains activity while the A_g mode exhibits a red-shift so that its frequency matches more closely with that of the IR activity plot in Figure 7a. It has been shown experimentally that by doping C_{60} with alkali metals (similar to having a negative point charge) the A_g mode shifts to the red.[125-126] This is due to electron transfer into an antibonding orbital on C_{60} that causes the C−C bonds to contract and the C=C bonds to expand.[127-129] Overall, these calculations begin to paint a picture of how fullerene might

gain VSFG activity due to a unidirectional electrostatic perturbation that enables the F_{1u} and A_g modes to become both IR- and Raman-active.

Taking this one step further, we calculate the VSFG spectra for perturbed fullerene using the transition dipole and polarizability derivatives to calculate the hyperpolarizibility tensor using equation 5. Assuming ψ and θ to be zero and using equations 1−5, the VSFG intensity for a given polarization combination will be estimated by $\left|\chi_{eff}^{(2)}\right|^2$. Figure 8a shows the calculated ssp VSFG spectra for C_{60} with a negative point charge at 3 Å (black) and with no virtual charge (red). As expected, the unperturbed spectrum shows negligible VSFG activity since the F1u and A_g modes are exclusively IR- or Raman-active.

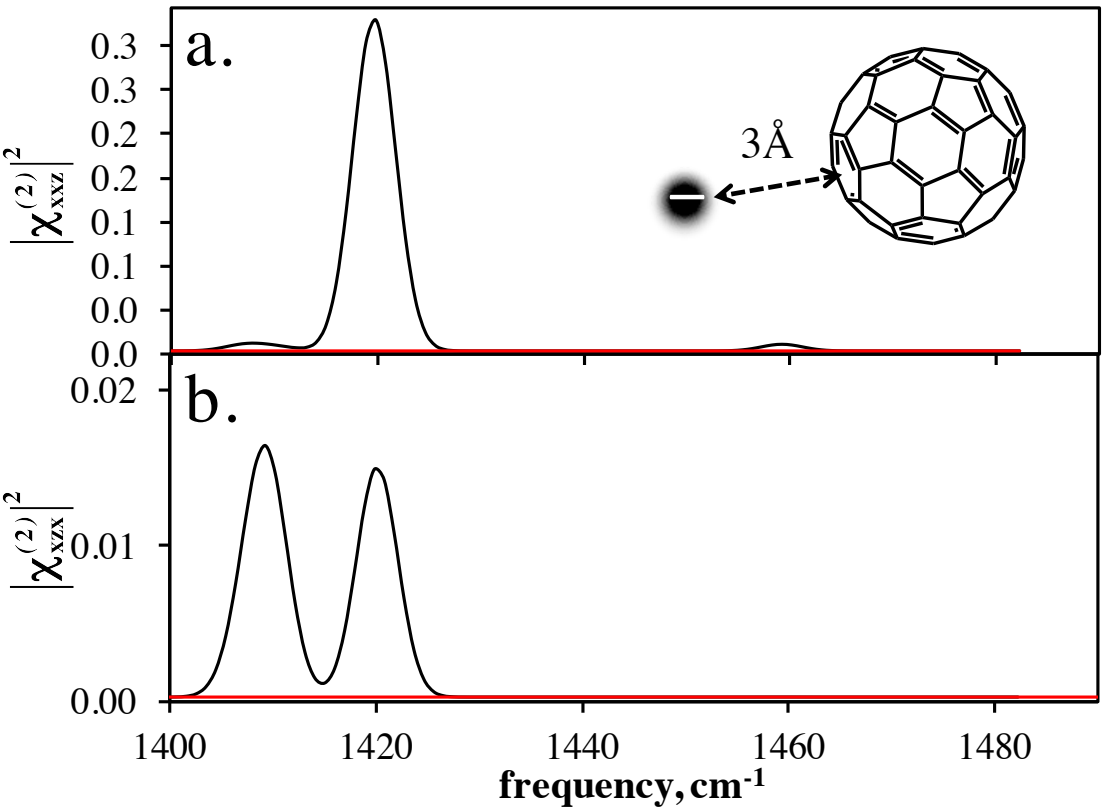

Figure 8. Calculated hyperpolarizabilities squared for the (a) $\left|\chi_{xxz}^{(2)}\right|^2$ and (b) $\left|\chi_{xzx}^{(2)}\right|^2$ tensor elements with a virtual negative charge at 3 Å (black traces) and no virtual charge (red traces).

Likewise, Figure 8b shows that the sps VSFG spectrum, although about an order of magnitude weaker than the ssp spectrum at the susceptibility level, is still many orders of magnitude larger when the fullerene is perturbed by a negative charge at 3 Å. In both polarization combinations, the electrostatic perturbation breaks the molecular symmetry of C_{60}, activating both modes in the VSFG spectrum. Comparing Figure 8a to Figure 5a, the experimental ssp VSFG spectra also have two peaks at ~1430 and ~1470 cm^{-1}. The 1470 cm^{-1} peak is negligible for the sps spectra (Figures 5b), and the calculations capture this difference as well.

At this point, we examine the distance dependence of the virtual charges in the VSFG activity of these modes in order to understand the spectral differences that we observe on different dielectrics. Figure 9a demonstrates that the F_{1u} mode VSFG activity is sharply peaked at a distance of around 3.25 Å and then decreases exponentially with distance, whereas the A_g mode VSFG activity only increases slightly over this range. This indicates that the F_{1u} mode in the VSFG spectra should be particularly sensitive to perturbations by the substrate. Referring back to the experimental spectra in Figure 5, it is tempting to initially conclude that the A_g mode is perhaps the more sensitive of the two since it appears to change the most between SiO_2 and CaF_2. But, for the case of an electrostatic perturbation, our calculations indicate that this is not the case. It is important to remember that the VSFG spectra are highly sensitive to the optical constants of the substrate, and it is often found that slight differences in material type lead to large differences in spectral intensities. [117-120] For example, the A_g mode VSFG activities could be similar, but the beam propagation across different material interfaces makes the CaF_2 appear larger in this region. In that case, the F_{1u} would have to be significantly smaller on CaF_2.

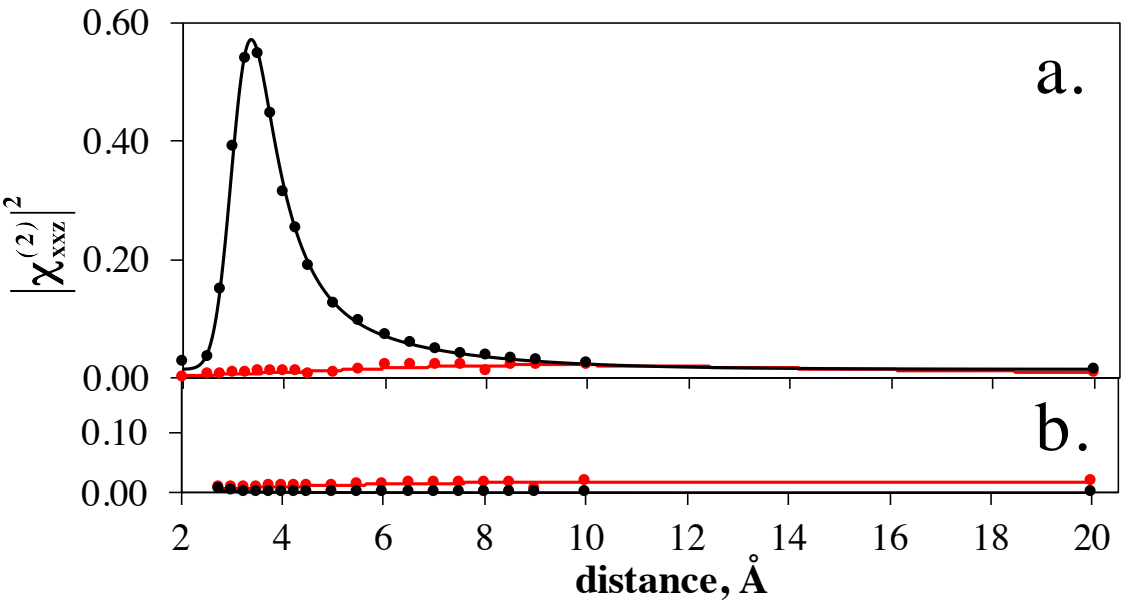

Figure 9. Sum of calculated $\left|\chi^{(2)}_{xxz}\right|^2$ for C60 in the F1u (black) and Ag (red) spectral regions as a function of distance from (a) negative and (b) positive virtual charge. Solid lines are an exponential convolved with a Gaussian fit to the calculated data points.

The positive virtual charge had a notably weaker influence on $\left|\chi^{(2)}_{xxz}\right|$ in our calculations (Figure 9b). Note that the vertical scales on the upper and lower frames in Figure 9 are the same, showing that the behavior of the A_g mode is similarly weak with positive and negative virtual charges, while the F_{1u} mode is barely responsive to the positive charge. Recalling that C_{60} is a good electron acceptor, it is not surprising that the structure is more readily perturbed by the presence of a negative charge.

4.4. Comparing Experimental and Calculated VSFG Spectra

Once again returning to the experimental VSFG spectra (Figure 5) and best fit parameters (Table 1), we see that the ratios for the squared second-order susceptibilities (F_{1u}/A_g) at interface 2 are 0.35 and 20.6 for SiO_2 and CaF_2, respectively. The squared susceptibility

ratios can be compared directly to the calculated VSFG activity ratios, which are plotted in Figure 10 as a function of the distance of the positive and negative virtual charges. As expected, the negative charge plot is notably more dynamic than that of the positive charge.

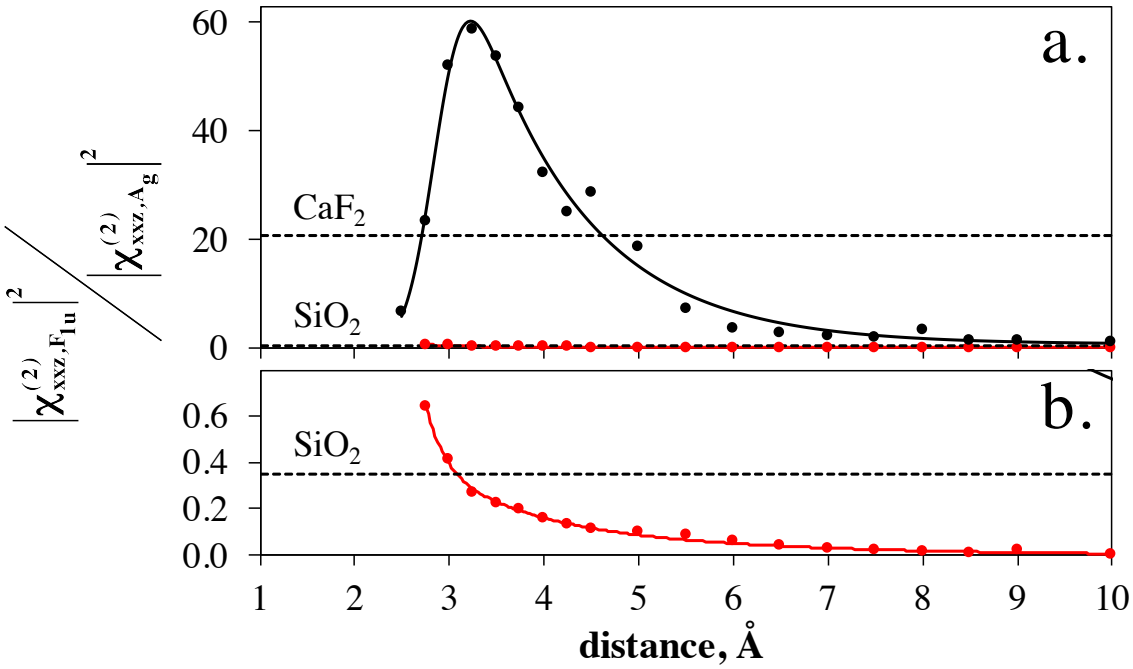

Figure 10. (a) Squared susceptibility ratio of the F_{1u} to A_g modes for C_{60} as a function of distance from negative (black) and positive (red) virtual charges and (b) the same data shown on an expanded y-axis to highlight the positive charge results. Overlaid solid lines are an exponential convolved with a Gaussian fit to the calculated data points.

The perturbation of C_{60} by the CaF_2 surface is equivalent to the molecule sitting at a closer distance from a negative charge. On silica, the VSFG spectrum is much less perturbed, equivalent to the molecule sitting very far from a negative point charge or near a positive point charge. The only crossing point with calculated ratios is found with the positive charge ratio at around 3 Å. This is not to say that the experimental values do not cross the negative charge curve, just that they do not intersect over the range of distances that we simulated. In contrast, there is no reasonable distance along the positive charge

curve that ever reaches a VSFG activity ratio near the experimental value of CaF_2 at 20.6.

It is important to reiterate that the signal amplitudes from the inner and outer interfaces are comparable for most of the resonances in this study. Our calculations show that the dielectric influence on the VSFG activity falls off by 2 nm; thus, for a 10 nm film we should not expect that the outer interface is affected by the dielectric. This means that the comparable amplitude at the outer interface arises solely from the abrupt change in going from fullerene to air, while at the buried interface the ratio of the F_{1u} and A_g modes are modulated differently by the different dielectrics. The fact that the CaF_2/C_{60} interface has a VSFG peak ratio that is larger than the SiO_2/C_{60} interface shows that the CaF_2 perturbs the fullerene molecule more strongly. There is a native thin layer of silica on the substrate of the silicon samples, which has a neutral or slightly negative surface charge due to the RCA cleaning method.[96]

CaF_2, on the other hand, is an ionic solid with a fluorite crystal structure.[130] It is known that for this type of crystal structure, if dry cleaved, the terminal interface should be charged by the fluoride anions and thus has a local negative charge.[130] This however is for an ideal and pristine surface. In reality determining the charge is more complex. If the surface has been in contact with water, during polishing or cleaning procedures, then the surface charge depends on the pH of the water and under neutral pH the surface charge is positive.[131-132] When CaF_2 is in contact with water even though it might have a positive surface charge, the fluoride ions dissolve and reside near the interface as a counter ion to the positive surface charge.[132] For a dry interface, the case for this experiment, the fluorine vacancies generated during the cleaning procedure could be refilled with other species leaving some ambiguity about the surface charge. Our unidirectional perturbation calculations support a

model in which dielectrics with negative surface charges perturb the fullerene structure and change its IR, Raman, and therefore VSFG activity. This local negative charge is hypothesized to cause the strong interaction with C_{60}, an electron acceptor relative to the neutrally charged surface of SiO_2. This stronger perturbation results in a larger amplitude ratio between the F_{1u} and A_g peaks.

Finally, we note that Wei and co-workers reported ssp and sps VSFG spectra of [6,6]-phenyl-C_{61}-butyric acid methyl ester (PCBM) deposited on CaF_2 that looked remarkably similar to the spectrum of C_{60} on SiO_2.[18] In that case, the VSFG activity was attributed to functionalization breaking the molecular symmetry, but the current study shows that even unfunctionalized C_{60} films generate nonlinear signals when deposited on dielectric substrates.

Furthermore, a phase-segregated fluorocarbon functionalized PCBM in that study gave a spectrum that looked very much like that of C_{60} on CaF_2 in Figure 4. Hence, the VSFG spectrum of C_{60} on SiO_2 looks like that of PCBM on CaF_2, and the spectrum of C_{60} on CaF_2 resembles fluorinated-PCBM on top of PCBM. However, a fundamental difference between these two studies is that PCBM has a molecular axis that is largely defined by its butyric acid functional group, which may be oriented differently from the substrate normal. This allows differences in the F_{1u} and A_g mode amplitudes to be explained by orientational changes. In contrast, the molecular axis of C_{60} is defined by the substrate itself, requiring that the mode heights in the VSFG spectra be differentiated by the perturbation strength for each dielectric type.

5. Conclusion

Fullerene has been previously shown to be VSFG active on metal surfaces and when its molecular structure has been modified to eliminate centrosymmetry. Here we showed that depositing C_{60} onto common dielectric surfaces leads to differences in VSFG activity that depend on the nature of the material. We modeled these changes as a unidirectional electrostatic perturbation using virtual positive and negative charges in gas-phase DFT calculations. This is admittedly a simplified view of a surface, which likely has a fair amount of surface charge heterogeneity, but it is nonetheless successful at qualitatively reproducing the results of our ensemble averaged measurements. The results in this chapter underscore the necessity of proper spectral fitting in VSFG spectroscopy to take into account multilayer interference and highlight the complex interplay between IR and Raman activities leading to a VSFG spectrum. Although the IR activity of the F_{1u} vibrational mode is more sensitive to the electrostatic perturbation, subtle changes in the A_g mode have a profound influence on the VSFG spectra. We found that CaF_2 had a significantly stronger influence on the nonlinear spectrum than SiO_2 due to its ionic nature and negative surface charge. The sensitivity of fullerene to the surface negativity indicates that many common materials could have markedly different interfacial vibrational spectra depending on substrate preparation.

Vibrational Sum Frequency Generation Spectroscopy of 6T on glass

1. Introduction

Organic materials have been used extensively and successfully in electronics in the past four decades.[133-142] One group of organic materials used vastly are conjugated oligomers[143-145] and one of the most famous group of these materials is the thiophenes. Oligo- and polythiophenes have been used in transistors[146-151] and photovoltaics[152-155] since the 1980's.

Oligothiophenes are small molecules and thus have the potential to be vapor deposited as thin film samples without degradation, unlike polythiophenes that are usually spin-cast from solution. Vapor deposition is desirable when working with a laser system; the samples are more homogeneous on a molecular level and they are systematically more reproducible from one sample to another.

α-sexithiophene (6T) is a well-known oligothiophene that was first synthesized in 1987 at CNRS, Thiais, France.[156] It has been shown that a polycrystalline film of 6T has a higher carrier mobility than disordered polythiophenes samples.[156] It has also been shown that 6T structure varies significantly with evaporation rate[157], substrate type[158-161] and substrate temperature.[156, 162-164] It was of specific interest to us to understand how 6T structure grew on an RCA-cleaned glass substrate, understand how topological structures are different at different thicknesses and tie this back to any change in average orientation on the two different interfaces (6T/glass and air/6T) at various thicknesses.

Vibrational Sum Frequency Generation (VSFG) spectroscopy, a surface-specific analytical technique introduced in Chapter 1, is suitable for such studies since it provides insight into the orientation of molecules at interfaces.[21, 78] Atomic Force Microscopy (AFM) was also used to gain information about the topography of the outer interface (air/6T) of the thin film samples. Information from VSFG in combination with data from AFM offers a more complete picture of 6T structure on a glass substrate.

2. Experimental

2.1. Materials

α-sexithiophene (6T) was used as received from Sigma-Aldrich. The water that was used for the RCA cleaning method was HPLC grade from Sigma-Aldrich. Hydrogen peroxide used in the RCA cleaning method was 30% from Fisher Scientific and was stored in the fridge after opening. Hydrogen peroxide that was stored for longer than six months in the fridge was never used and disposed of due to losing its oxidation ability. Ammonium hydroxide (NH_4OH), used in the RCA cleaning method, was 28-30% as NH_3 from Macron Chemicals. Hydrochloric acid (HCl), which was used in the RCA cleaning method, was 36.5-38% from BDH Chemicals.

2.2. Sample Preparation

IR spectra were collected in the attenuated total reflection (ATR) setup on 6T powder. Raman spectra were collected on a thin film sample of 6T. The sample was made on a silicon substrate that was cleaned with a modified RCA cleaning method[97-99] (described in Chapter 2) prior to the deposition of 6T. This substrate had a 2-3 nm thin layer of native

oxide (SiO_2). A 6T layer of about 30 nm was then vapor deposited on the silicon substrate under high vacuum with an average pressure of 5×10^{-6} Torr at room temperature.

The VSFG and AFM data were collected on thin film samples of 6T on glass. The glass substrate was cleaned by the modified RCA cleaning method and then 6T was vapor deposited under high vacuum with an average pressure of 5×10^{-6} Torr at room temperature. The samples were 19, 28, 38, 47.5, 76 and 105nm thick.

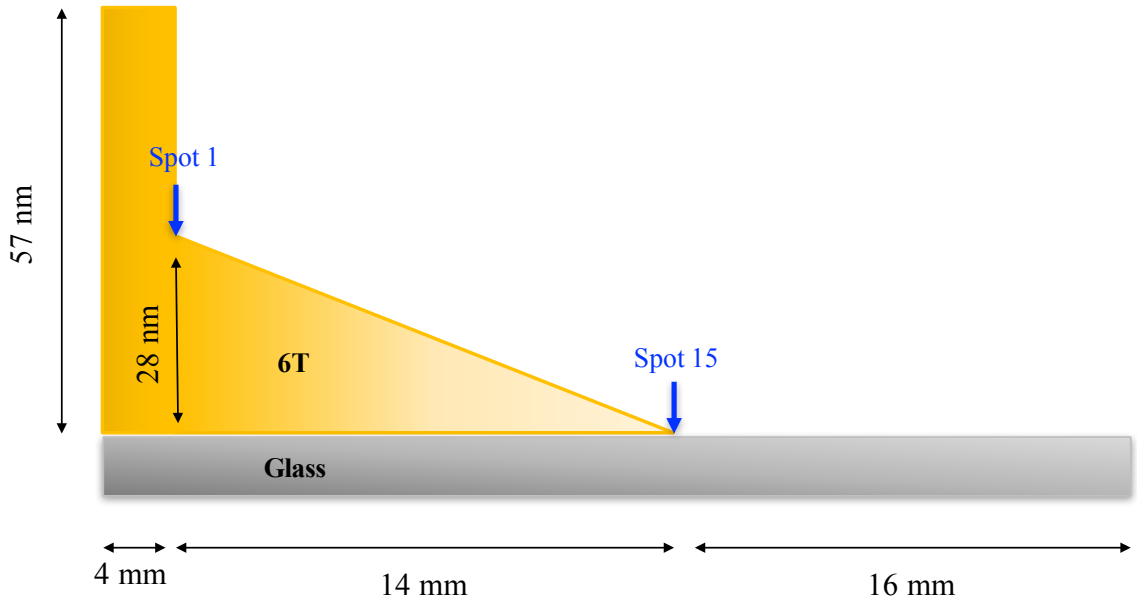

Figure 1. 6T gradient sample on glass substrate

For the second set of AFM and VSFG data a linear thickness gradient 6T thin film sample was prepared (Figure 1). The sample had a thicker 4 mm edge with a 57 nm thickness that served as a visual aid to mark the spot where the gradient started. The gradient was 28 nm thick at the maximum thickness and 14 mm long. The gradient sample was made by an automated shutter that moved back and forth along 14 mm of the sample, enabling a gradient deposition and blocking the rest (16 mm) from deposition.[165]

2.3. Measurement and Instrumentation

The IR spectrum was collected on a Thermo-Electron Nicolet 6700 spectrometer, with a resolution of 1.0 cm^{-1} and an average of 16 scans. Raman spectra were collected at the University of Minnesota Characterization Facility, on a Witec Alpha300 R confocal Raman microscope with a UHTS300 spectrometer and a DV401 CCD detector. A Nikon 100× objective was used prior to sending the data to the detector. The light source was a 532 nm diode-pumped Nd: YAG solid state laser coupled with an 1800 g/mm grating. The optical resolution was diffraction limited to 250 nm laterally and 500 nm vertically. The spectral resolution on this instrument is 0.02 cm^{-1}. The spectrum was collected for 10 accumulations with an integration time of 2 seconds for each accumulation.

The VSFG instrument has already been described in Chapter 2. The slight difference here is that, to produce the visible pump beam, the uncompressed 800 nm light from the regenerative amplifier was spectrally narrowed in a 4f pulse shaper (Figure 2a) to about 1 nm FWHM centered at 792.2 nm with pulse energies of 5 μJ at the sample.

The mid-IR (centered at 1460 cm^{-1}) and visible pulses were focused onto the sample surface, and the resulting VSFG signal was collected in a reflective setup using a pair of 60° off-axis parabolic mirrors. Spectra were collected in the ssp and sps polarization combinations. The VSFG spectra for each single-thickness sample were collected on three different spots, using an average of five exposures, where each exposure was 5 minutes for ssp on all samples. For the sps polarization on the 19 and 47.5 nm samples exposure was 40 minutes and for the 105 nm samples it was 30 minutes. Between every spot a reference VSFG spectrum was collected from a zinc oxide reference sample that was prepared by atomic layer deposition on a glass substrate. The spectra from the samples were then

normalized by these reference spectra.

The VSFG data for the gradient sample were collected on a slightly different VSFG setup, the frequency comb SFG.[166] In this setup the 4f pulse shaper is modified to create a simple frequency comb, where two visible pulses were separated spectrally but aligned temporally and spatially (Figure 2b).

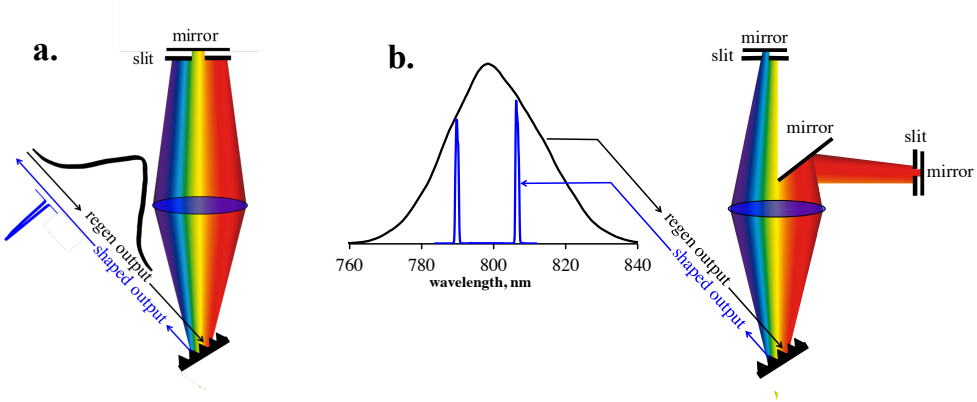

Figure 2. (a) 4f pulse shaper in the initial VSFG setup, (b) 4f pulse shaper in the frequency comb SFG setup.

This setup enables the collection of different polarization combinations simultaneously on the monochromator since the visible pulses are separated in frequency. However, the data on the gradient sample were only collected in the ppp polarization combination since the signals on the ssp and sps polarizations were too weak to detect. These spectra were also collected on three different spots, using an average of five exposures, where each exposure was 10 minutes long.

Atomic force microscopy (AFM) was performed on an Agilent 5500 environmental scanning probe microscope using tapping mode. AFM cantilevers were bought from Nano World innovative technologies ® and were made of monolithic silicon which is highly doped to dissipate static charge. The sample chamber was purged with N_2 gas and the

relative humidity was kept under 10% at all times. We found that by eliminating humidity we could obtain better quality AFM images. All images were collected at room temperature with scan speeds of 0.5 line/s.

Variable angle spectroscopic ellipsometry (VASE) measurements were performed for calibration purposes using a J.A. Woollam Co. instrument. Three angles of incidence 65°, 70° and 75° were used in the 800-1100 nm spectral range. The Cauchy relationship was used for modelling the 6T layer when solving for the film thickness.[167] Each thickness was averaged over three spots. All mean squared errors for the fit (to find thickness) were less than 0.55.

2.4. Calibration of the Quartz Crystal Microbalance (QCM)

Typically to measure the thickness of a vapor deposited thin film sample a Quartz Crystal Microbalance (QCM) is used, a piezoelectric material. In these materials, in the presence of mechanical stress an electric field or signal is generated and vice versa. In the vapor deposition chamber an alternating electric field is applied to the QCM electrodes which in turn causes the crystal to oscillate. During a deposition the change of mass at the crystal's surface causes a change in the crystal's oscillation frequency that can mathematically be related back to the thickness of the deposited material. However, this measurement method needs to be calibrated for each material using samples of that material made with different thicknesses.

To calibrate the QCM for 6T, a thin film sample of 6T on RCA-cleaned silicon (with a thin native oxide layer) was used. The calibration sample had four different thicknesses. Each thickness was registered by the QCM and then measured using the spectroscopic

ellipsometer. Figure 3 shows the calibration function obtained from these measurements. This calibration function was used for finding the correct film thickness which was subsequently used when fitting all the VSFG data.

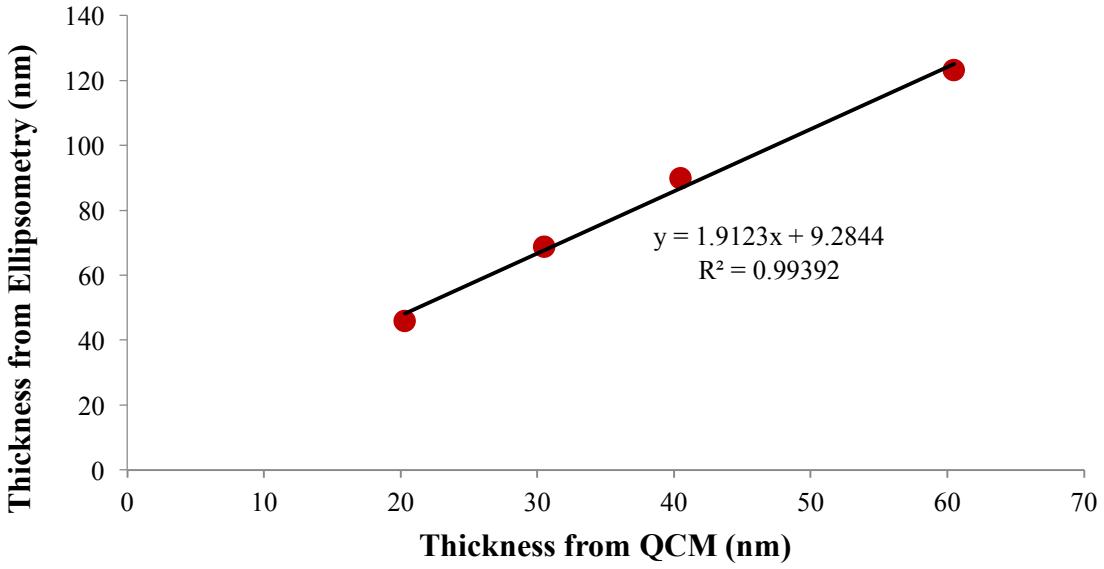

Figure 3. QCM calibration function using ellipsometric measurements

2.5. Determining Optical Constants of 6T

In order to quantify the VSFG spectral differences, $\chi^{(2)}$should be determined for each mode by taking into account multilayer interference during propagation of all three beams (described in Chapter 1).[117-120] For all samples, interface 1 (outer interface) is the air/6T interface and interface 2 (inner interface) is 6T/glass. SiO_2 (glass) real and imaginary refractive indices (from 1200 to 1700 cm^{-1})[122] were obtained by fitting experimental measurements to a polynomial equation, which was applied in the multilayer model. 6T optical constants were found by applying ellipsometric spectroscopy to 6T thin film samples on gold substrates. The samples were made on a gold substrate since gold had the

minimum interference spectrum in the region that ellipsometry was being measured, the mid-IR region. Samples were prepared and sent for measurement to J.A. Woollam Co. located in Lincoln, NE. The optical constants for 6T (real and imaginary components) were obtained from these measurements.

3. Results and Discussion

3.1. IR and Raman Spectra of 6T

VSFG activity requires both IR and Raman activities, as shown previously in Chapter 1.[21] Thus, it is of importance to study the linear vibrational spectroscopy of the molecule

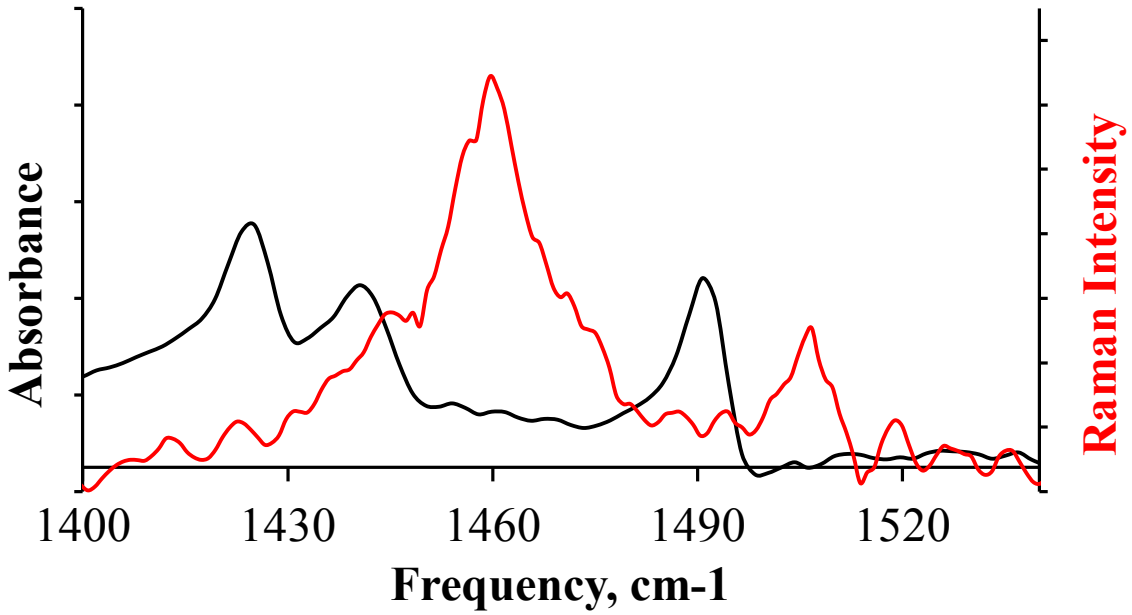

Figure 4. IR spectrum of 6T powder (black) and Raman spectrum of a 6T thin film sample on a silicon substrate with native oxide (red)

of interest prior to doing VSFG. Figure 4 shows the IR and Raman spectra of the 6T molecule.

The IR spectrum shows three peaks at 1425, 1440 and 1490 cm^{-1}, which have all been

reported in the literature previously.[168-171] The 1490 cm^{-1} peak is assigned to the C=C asymmetric stretching band and the 1425 and 1460 cm^{-1} peaks to the C=C symmetric stretches.[168] Within the resolution of our instrument the Raman spectrum shows two peaks centered at 1460 and 1507 cm^{-1}, which have both been reported in the literature before. [168-172] The higher frequency peak at 1507 cm^{-1} is assigned to the asymmetric C=C stretch and the 1460 cm^{-1} peak to the C=C symmetric vibration.[168]

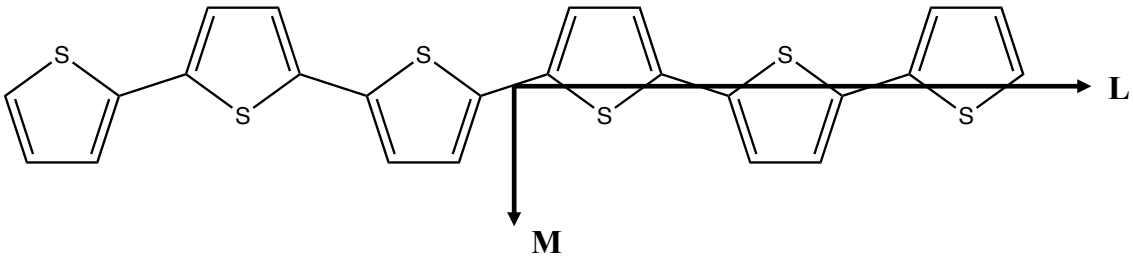

Figure 5. 6T molecule and the long(L) and short (M) molecular axis

It has been previously shown[170] that the symmetric stretch is polarized along the molecular short axis (M) and the asymmetric stretch along the molecular long axis (L) (Figure 5). Both the symmetric and asymmetric modes seem to be IR and Raman active on these 6T samples so we expect to be able to see at least one of these modes in the VSFG measurement. Having the ability to see both modes depends on the polarization combination that is used.

3.2. VSFG and AFM data of 6T Single-thickness Thin Film Samples

Figure 6 shows the VSFG spectra of thin film samples of 6T on glass substrates with thicknesses of 19 nm, 47.5 nm and 105 nm. The data were collected in two polarization combinations, ssp (Figure 6a) and sps (Figure 6b). The data show that the symmetric peak

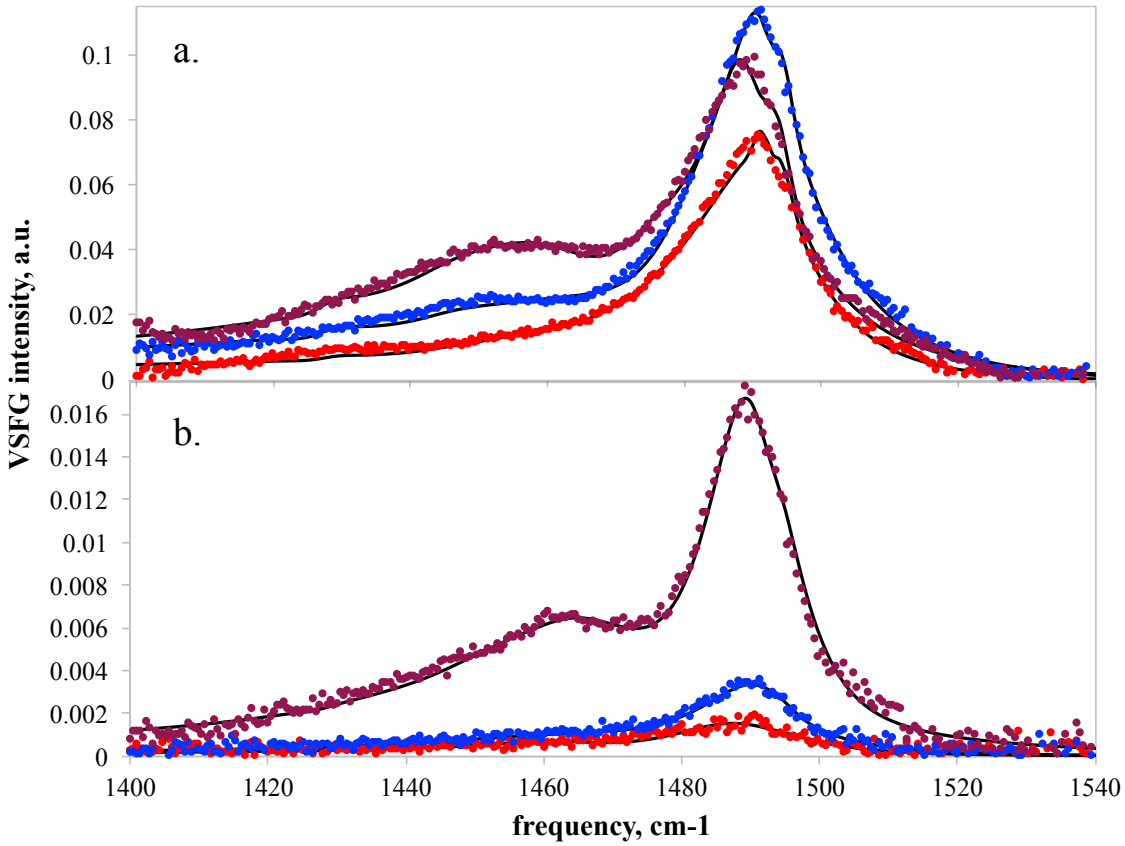

Figure 6. Experimental VSFG spectra of 6T on glass with a thickness of 19 nm (red), 47.5 nm (blue) and 105 nm (purple) overlaid with the multilayer interference fits (black line) for the (a) ssp polarization combination and (b) sps polarization combination.

grows as the thickness increases, however as it was shown in the previous chapter, the raw VSFG data cannot paint a complete picture of what is happening at the interfaces. A correct fitting routine needs to be used, parameters calculated, and then conclusions can be drawn.

The VSFG data were fitted with the global multilayer interference modelling routine described previously in Chapter 1.[118-120, 173] In all of these samples, the inner (6T/glass) interfaces were assumed to have the same molecular structure and chemical composition due to the interaction of the 6T and glass molecules, which was assumed to be the same between all samples, regardless of the sample thickness. Thus in the fits the frequency of

the symmetric and asymmetric peaks for this interface were fixed to be the same between samples. The outer (air/6T) interfaces were allowed to be different between the different samples. We attempted to use the same outer interface parameters for the frequency between the different samples but we could not get a reasonable fit with a small error. We hypothesized that this was because each sample thickness was at a different stage in the crystal growth mechanism. This was confirmed by the AFM images shown in Figure 8.

Tables 1, 2, and 3 show the best fit parameters that produced the solid lines overlaid on the data in Figure 6. The amplitude of the symmetric peak in the sps data for the inner interface has an overall smaller value compared to the rest of the parameters. The outer interface amplitude in the sps polarization and most of the inner and outer amplitude in the ssp polarization parameters. This gives us insight into the orientation of the molecule at the 6T/glass interface. In the ssp polarization combination the IR beam is P-polarized which means any vibrational mode that is polarized along the z-axis will be detected in this polarization. Similarly, in the sps polarization combination the IR is S-polarized and any vibrations with elements polarized along the interface plane, the x-y plane in Figure 7, will be observed. So the presence of the symmetric vibration in the ssp polarization combination and the absence of the same stretch in sps, suggests that the average molecular orientations at the 6T/glass interface are arranged in such a way that the symmetric vibration, polarized along the M axis, is parallel to the z-axis. This means that the molecules have an overall edge-on orientation.

It has previously been shown[174] that when 6T molecules are deposited at a submonolayer thickness on silicon dioxide, the molecular orientation is edge-on. However molecular

orientation for a thicker film of a couple monolayers changes to an end-on orientation; the long molecular axis (L) is perpendicular to the surface.[175-176]

Table 1. Best fit parameters to SFG data in ssp polarization combination (Figure 6a)

		Symmetric Mode			Asymmetric Mode		
Sample	**interface**	**amplitude**	**frequency cm^{-1}**	**HWHM cm^{-1}**	**amplitude**	**frequency cm^{-1}**	**HWHM cm^{-1}**
19nm	outer	-1.4265×10^{-5} ($+0.00013/-0.0001$)	1460 (+20/-50)	4.00671 (+10/-25)	0.0013689 (+0.002/ -0.002)	1491.15 (+20/-20)	11.8785 (+8/-8)
	inner	-3.441×10^{-9}	1472.04 (+10/-15)	4.9994 (+6/-16)	6.0716×10^{-5} (+0.0017/ -0.00012)	1491.5 (+20/-20)	1.7571 (+1/-2)
47.5nm	outer	0.00047877 (+0.0016/ -0.0008)	1482.95 (+25/-25)	9.01187 (+6/-9)	0.002006 (+0.004/ -0.004)	1491.4 (+20/-20)	10.9522 (+6/-9)
	inner	0.00132107 (+0.004/ -0.002)	1472.04 (+10/-15)	21.5077 (+10/-15)	0.00015596 (+0.0005/ -0.0002)	1491.5 (+20/-20)	2.45365 (+2.5/-2)
105nm	outer	0.0099184 (+0.018/ -0.018)	1468.62 (+10/-35)	17.3334 (+10/-10)	0.0037942 (+0.002/ -0.002)	1490.43 (+20/-20)	6.45515 (+4/-2)
	inner	0.003604 (+0.003/ -0.003)	1472.04 (+10/-15)	14.6235 (+10/-10)	0.001551 (+0.004/ -0.002)	1491.5 (+20/-20)	7.2516 (+9/-6)

Table 2. Best fit parameters to SFG data in sps polarization combination (Figure 6b)

		Symmetric Mode			Asymmetric Mode		
Sample	**interface**	**amplitude**	**frequency cm^{-1}**	**HWHM cm^{-1}**	**amplitude**	**frequency cm^{-1}**	**HWHM cm^{-1}**
19nm	outer	5.934×10^{-5} ($+1.5\times10^{-4}/-2.5\times10^{-4}$)	1464.31 (+15/-10)	11.0987 (+5/-20)	0.00018437 (+0.0003/- 0.0002)	1487.1 (+10/-20)	11.1957 (+20/-5)
	inner	-1.553×10^{-9} ($+2.6\times10^{-8}/-1.4\times10^{-7}$)	1461 (+50/-15)	9.00002 (+56/- 20)	-3.992×10^{-5} (+0.00028/ -0.00016)	1494.22 (+20/-10)	9.7999 (+115/ -25)
47.5nm	outer	0.00014519 (+0.0007/ -0.0009)	1466.98 (+25/-10)	18.6034 (+20/- 25)	0.0002492 (+0.0008/ -0.0012)	1489.78 (+15/-20)	10.4766 (+40/ -15)
	inner	4.346×10^{-6} ($+8\times10^{-6}/-1.6\times10^{-5}$)	1461 (+50/-15)	7.4 (+18/- 69)	2.908×10^{-5} (+0.0003/ -0.00036)	1494.22 (+20/-10)	4.7836 (+20/ -20)

105nm	outer	0.0008124 (+0.004/ -0.0016)	1466.61 (+10/-15)	19.5303 (+15/-15)	0.00087942 (+0.0016/ -0.0032)	1489.72 (+10/-10)	8.9855 (+8/-8)
	inner	2.2904×10^{-5} (+0.00006/ -0.0004)	1461 (+50/-15)	8.7 (+52/-28)	0.00053604 (+0.001/ -0.001)	1494.22 (+20/-10)	15.2452 (+80/ -20)

Table 3. Best fit parameters to non-resonant background of SFG data in ssp and sps polarization combination (Figure 6)

Sample	**Polarization**	**A_{NR}**	**ϕ_{NR}**
19nm	ssp	0.04013 (+0.08/-0.04)	4.33379 (+1.4/-1)
	sps	0.00765 (+0.015/-0.03)	11.7296 (+8/-16)
47.5nm	ssp	0.05022 (+0.02/-0.02)	10.2227 (+0.8/-0.8)
	sps	0.00569 (+0.015/-0.01)	10.7818 (+2/-6)
105nm	ssp	0.05048 (+0.03/-0.03)	18.1321 (+1.4/-0.6)
	sps	0.00766 (+0.02/-0.02)	10.7695 (+3/-2)

Tables 1 and 2 also show that the amplitude of the symmetric mode on the outer interface increases with thickness for both polarization combinations. This does not provide any specific information about molecular orientation except that with increase in thickness the orientation changes in a way that the projection of the symmetric mode has elements with bigger magnitude in both the z-axis and the x-y plane (Figure 7). In other words, with increase in thickness the molecule orients in a way that it not purely edge-on or end-on anymore but rather has an orientation with some contribution from both of these forms.

The bigger amplitude of the symmetric mode on the outer interface compared to the inner interface, shows that the orientation on the outer interface is not similar to that of the inner interface. The amplitude of the asymmetric mode also increases with thickness for both polarization combinations but the change is not considerable within the errors. The frequencies of the asymmetric modes for both polarizations are close to 1490 cm^{-1}, which

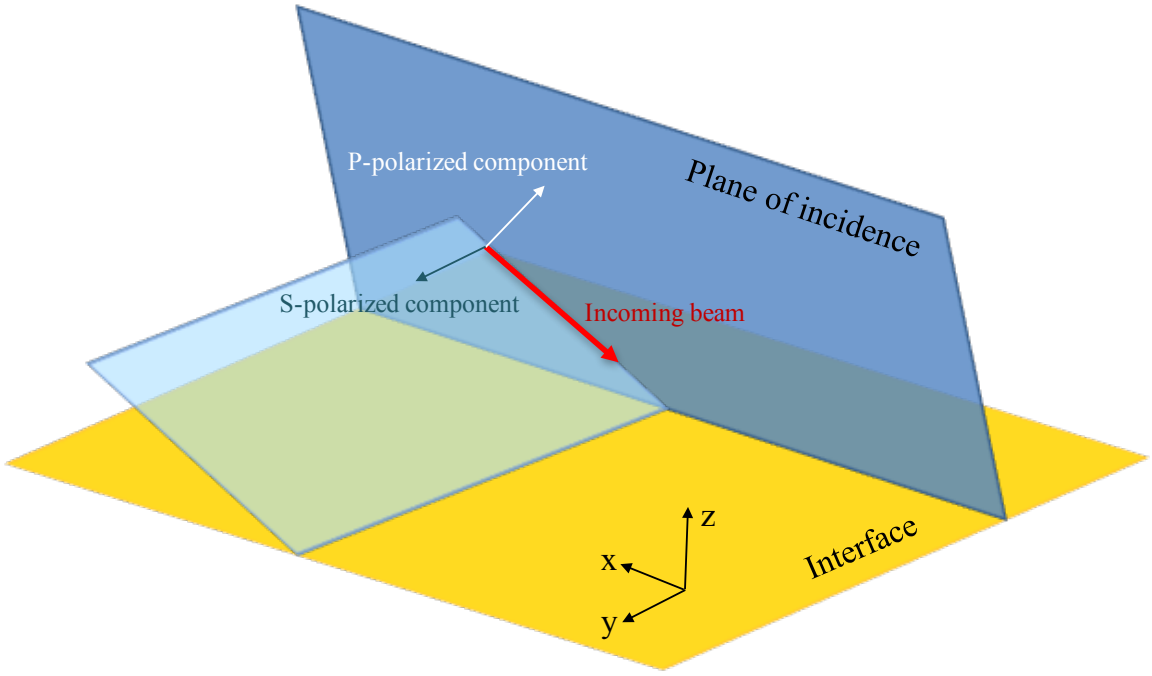

Figure 7. P-polarized and S-polarized components of an incoming beam and their relative orientation to the x, y and z coordinates (lab-frame coordinates)

is also the value obtained from the linear vibrational spectroscopy. However, for the ssp polarization we have frequency values for the symmetric mode that are far from the values observed in the linear spectra. During the fitting routine, we tried confining those frequencies to be closer to the value observed in linear vibrations (1460 cm^{-1}) but the fit resulted a higher error value and thus those results were not acceptable. This higher frequency for the symmetric mode might be described by the fact that possibly a resonance was not elucidated in the linear spectroscopies. Our Raman spectrum was not very well resolved and there might be a second peak at 1475 cm^{-1} that cannot be distinguished by the Raman instrument. This is due to the fact that the light source highly excites the molecules, to an extent where additional resonant contribution from the distorted molecules at the grain boundaries cause widening of the peaks.[169] It is worth noting that some studies have reported a Raman peak at 1473 cm^{-1} other than the peak at 1460 cm^{-1}.[169]

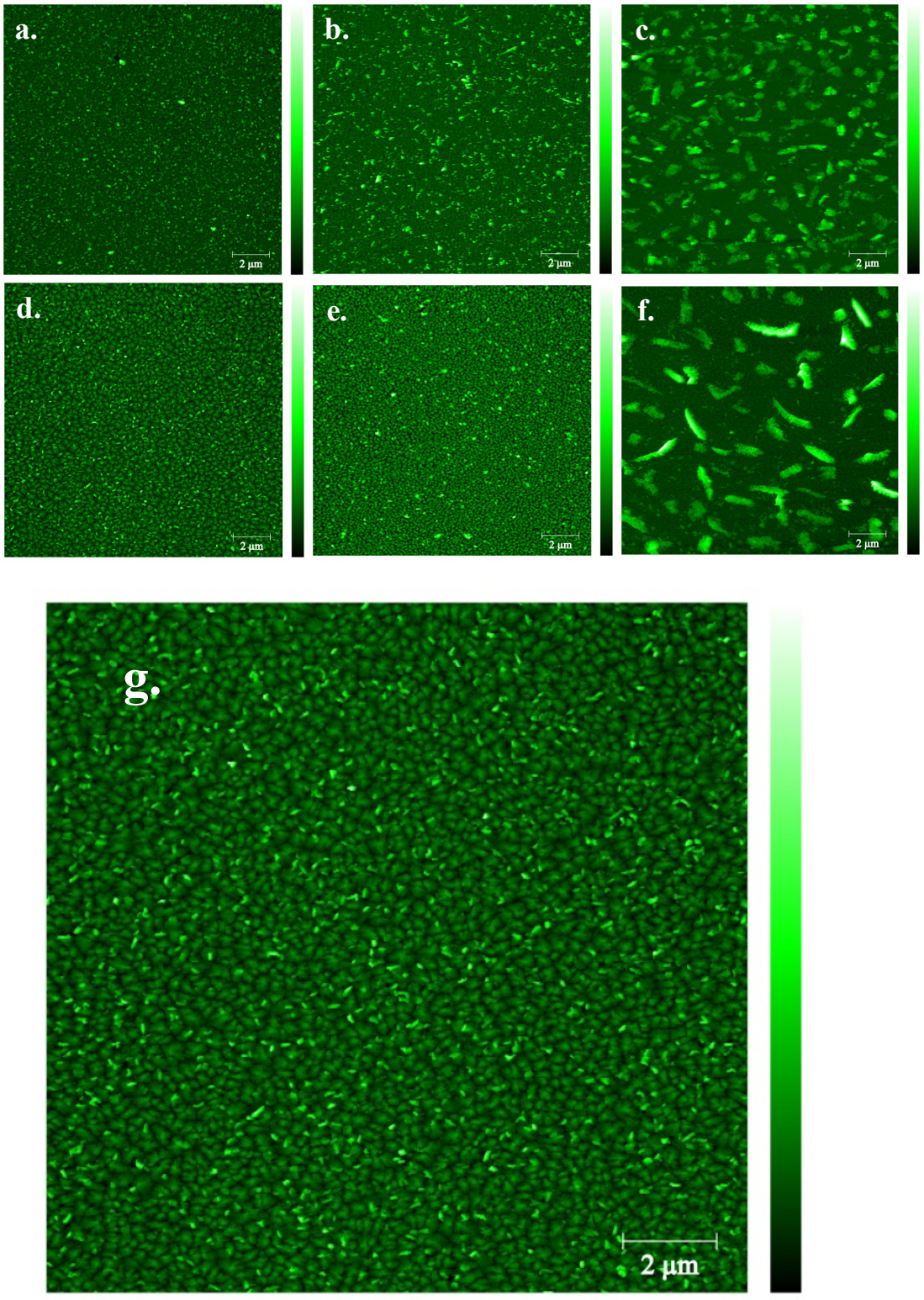

Figure 8. AFM images of 6T thin films on glass with thickness of (a) 19 nm, (b) 28 nm, (c) 38 nm, (d) 47.5 nm, (e) 76 nm and (f) 105 nm. (g) Zoomed AFM image of frame d.

Figure 8 shows AFM images of six samples with differing thicknesses. For three of these samples, 19, 47.5 and 105 nm thick samples, the VSFG data were shown above. The images show that the topographies of the samples change with thickness, from grains in dimensions of 100's of nanometer to micrometers. The images suggest the growth is reminiscent of a Stranski-Krastanov (SK) growth transition[177] where the first 2-3 layers have a layer-by-layer growth and later the growth mode changes to simultaneous multilayer growth (formation of 3D grains). This has been previously shown to be the case for oligothiophene films growth at room temperature.[178-180]

The second part of the SK growth, multilayer growth and grain formation, can clearly be seen in the different frames of Figure 8. Each frame has grains within a different height layer and size. This can be seen more clearly in frame d where there are three different heights visible to the eye, the dark green/black layer, the green layer that has tightly-formed packed grains and the brighter green particles that are more sparse and smaller in size (Figure 8g). So in this frame one can see that at least three heights with different grain sizes are all present together on one sample. This is true for all the other frames as well. To be able to see the first step of the SK transition, layer-by-layer formation, however one needs to investigate with samples of submonolayer to monolayer thicknesses.

3.3. VSFG and AFM data of a 6T Thin Film Gradient Sample

To observe the earlier steps of growth in the SK transition, a thickness gradient sample of 6T on glass was made with thickness range of 0 to 28 nm. Making a single gradient sample was preferred over using samples with different thicknesses in order to eliminate any bias associated with differences in deposition conditions and substrate characteristics.

VSFG data were then collected over the gradient on 15 spots, each a millimeter apart. VSFG was also collected on three spots beyond the gradient, where no 6T should have been present, which as expected resulted in no signal (spots 16, 17 and 18).

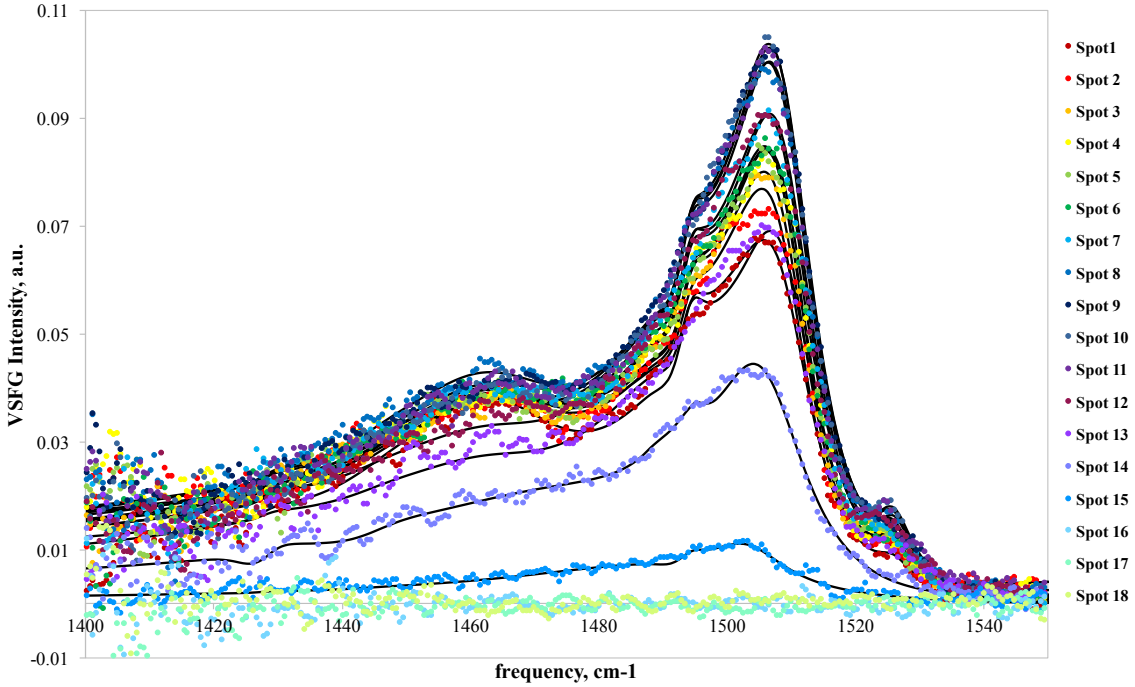

Figure 9. Experimental VSFG spectra of a gradient sample of 6T on glass with the multilayer interference fits (black lines).

The VSFG data at locations across the gradient and the resulting fits are depicted in Figure 9. Table 4 shows the thickness of each spot and its distance from the substrate edge (Figure 1) on the 6T gradient sample. The thicknesses of these spots were found by using the gradient length, thickness of the gradient at its maximum (as read by the QCM during deposition), the QCM calibration curve, and the fact that the spots were a millimeter apart. The resulting fit parameters of the experimental data in Figure 9 are presented in Tables 5 and 6. These data were also fitted using the global multilayer interference model. [118-120, 173] Since all the points were collected on the same sample, the same frequency and half-width at half-maximum (HWHM) values for all spots and both interfaces were chosen and thus

Table 4. Corresponding thickness for each spot on the 6T gradient sample (Figure 9)

Spot on Gradient	Thickness (nm)	Distance of spot from substrate edge (mm)
1	28.40	4
2	26.37	5
3	24.34	6
4	22.31	7
5	20.28	8
6	18.25	9
7	16.22	10
8	14.19	11
9	12.16	12
10	10.13	13
11	8.1	14
12	6.07	15
13	4.04	16
14	2.01	17
15	0.01	18

Table 5. Best fit parameters to SFG data in ppp polarization combination for the gradient sample (Figure 9)

Spot	interface	Symmetric Mode			Asymmetric Mode		
		amplitude	frequency cm^{-1}	HWHM cm^{-1}	amplitude	frequency cm^{-1}	HWHM cm^{-1}
1	outer	0.0002179 (+0.00013/ -0.0001)	1465.54 (+10/-10)	17.1602 (+10/ -10)	0.00020287 (+0.00021/ -0.00013)	1495.6 (+8/-6)	15.7344 (+10/ -10)
	inner	-2.2304×10^{-5} (+0.00011/ -0.00346)	1525.71 (+10/-10)	3.4913 (+10/ -10)	0.000339 (+0.00019/ -0.0003)	1508.6 (+10/-10)	8.0138 (+10/ -10)
2	outer	0.0001268 (+0.00022/ -0.00007)	1465.54 (+10/-10)	17.1602 (+10/ -10)	9.1218×10^{-5} (+0.0004/ -0.0001)	1495.6 (+8/-6)	15.7344 (+10/ -10)
	inner	2.850×10^{-5} (+0.00015/ -0.0002)	1525.71 (+10/-10)	3.4913 (+10/ -10)	0.000369 (+0.001/ -0.001)	1508.6 (+10/-10)	8.0138 (+10/ -10)
3	outer	0.0001543 (+0.0003/ -0.0002)	1465.54 (+10/-10)	17.1602 (+10/ -10)	0.0001457 (+0.0004/ -0.0002)	1495.6 (+8/-6)	15.7344 (+10/ -10)
	inner	4.1031×10^{-5} (+0.00015/ -0.00025)	1525.71 (+10/-10)	3.4913 (+10/ -10)	-0.000392 (+0.001/ -0.001)	1508.6 (+10/-10)	8.0138 (+10/ -10)
4	outer	0.0001235 (+0.0003/ -0.0002)	1465.54 (+10/-10)	17.1602 (+10/ -10)	9.6662×10^{-5} (+0.0006/ -0.0002)	1495.6 (+8/-6)	15.7344 (+10/ -10)

	Inner	-2.3483×10^{-5} (+0.0001/ -0.00006)	1525.71 (+10/-10)	3.4913 (+10/ -10)	-0.000391 (+0.001/ -0.001)	1508.6 (+10/-10)	8.0138 (+10/ -10)
5	outer	0.0001548 (+0.0004/ -0.0004)	1465.54 (+10/-10)	17.1602 (+10/ -10)	0.0001413 (+0.0004/ -0.0002)	1495.6 (+8/-6)	15.7344 (+10/ -10)
	inner	3.4409×10^{-5} (+0.00012/ -0.00021)	1525.71 (+10/-10)	3.4913 (+10/ -10)	-0.000404 (+0.001/ -0.001)	1508.6 (+10/-10)	8.0138 (+10/ -10)
6	outer	0.0001612 (+0.0004/ -0.0004)	1465.54 (+10/-10)	17.1602 (+10/ -10)	0.0001924 (+0.0004/ -0.0004)	1495.6 (+8/-6)	15.7344 (+10/ -10)
	inner	-2.0194×10^{-5} (+0.00014/ -0.0001)	1525.71 (+10/-10)	3.4913 (+10/ -10)	-0.0003747 (+0.001/ -0.001)	1508.6 (+10/-10)	8.0138 (+10/ -10)
7	outer	0.0001545 (+0.0004/ -0.0004)	1465.54 (+10/-10)	17.1602 (+10/ -10)	0.0001779 (+0.0003/ -0.0003)	1495.6 (+8/-6)	15.7344 (+10/ -10)
	inner	3.3318×10^{-5} (+0.00008/ -0.00015)	1525.71 (+10/-10)	3.4913 (+10/ -10)	-0.0004212 (+0.0006/ -0.0006)	1508.6 (+10/-10)	8.0138 (+10/ -10)
8	outer	0.0001455 (+0.0003/ -0.0002)	1465.54 (+10/-10)	17.1602 (+10/ -10)	0.0001694 (+0.0004/ -0.0003)	1495.6 (+8/-6)	15.7344 (+10/ -10)
	inner	3.2543×10^{-5} (+0.0001/ -0.00016)	1525.71 (+10/-10)	3.4913 (+10/ -10)	-0.0004367 (+0.0004/ -0.0006)	1508.6 (+10/-10)	8.0138 (+10/ -10)
9	outer	0.0001205 (+0.0002/ -0.0002)	1465.54 (+10/-10)	17.1602 (+10/ -10)	0.0001552 (+0.0003/ -0.0002)	1495.6 (+8/-6)	15.7344 (+10/ -10)
	inner	-2.644×10^{-5} (+0.0001/ -0.00008)	1525.71 (+10/-10)	3.4913 (+10/ -10)	-0.0004462 (+0.0008/ -0.0008)	1508.6 (+10/-10)	8.0138 (+10/ -10)
10	outer	0.000122 (+0.0002/ -0.0002)	1465.54 (+10/-10)	17.1602 (+10/ -10)	0.0001826 (+0.0003/ -0.0003)	1495.6 (+8/-6)	15.7344 (+10/ -10)
	inner	4.0908×10^{-5} (+0.0001/ -0.00018)	1525.71 (+10/-10)	3.4913 (+10/ -10)	-0.0004628 (+0.0004/ -0.0004)	1508.6 (+10/-10)	8.0138 (+10/ -10)
11	outer	0.0001118 (+0.0002/ -0.0002)	1465.54 (+10/-10)	17.1602 (+10/ -10)	0.000175 (+0.0003/ -0.0003)	1495.6 (+8/-6)	15.7344 (+10/ -10)
	inner	-3.783×10^{-5} (+0.00018/ -0.0001)	1525.71 (+10/-10)	3.4913 (+10/ -10)	-0.0004462 (+0.0006/ -0.0006)	1508.6 (+10/-10)	8.0138 (+10/ -10)

12	outer	8.477×10^{-5} (+0.00016/ -0.00016)	1465.54 (+10/-10)	17.1602 (+10/ -10)	0.000203 (+0.0004/ -0.0004)	1495.6 (+8/-6)	15.7344 (+10/ -10)
	inner	-4.174×10^{-5} (+0.00024/ -0.00008)	1525.71 (+10/-10)	3.4913 (+10/ -10)	-0.0004307 (+0.0008/ -0.0008)	1508.6 (+10/-10)	8.0138 (+10/ -10)
13	outer	7.838×10^{-5} (+0.00024/ -0.00016)	1465.54 (+10/-10)	17.1602 (+10/ -10)	0.0002165 (+0.0004/ -0.0004)	1495.6 (+8/-6)	15.7344 (+10/ -10)
	inner	2.762×10^{-5} (+0.0001/ -0.00016)	1525.71 (+10/-10)	3.4913 (+10/ -10)	-0.0003527 (+0.0006/ -0.0006)	1508.6 (+10/-10)	8.0138 (+10/ -10)
14	outer	0.0002561 (+0.0008/ -0.0014)	1477.76 (+45/-200)	32.0669 (+70/ -215)	1.724×10^{-5} (+0.0002/ -0.00002)	1492.81 (+15/-10)	2.929 (+25/ -55)
	inner	-0.02202 (+0.1/-?)	1876.76 (+410/ -370)	125.8 (+?/ -?)	-0.0003498 (+0.0016/-?)	1505.91 (+10/-10)	9.6542 (+10/ -15)
15	outer	--	--	--	-4.959×10^{-5} (+0.0005/ -0.00045)	1503.16 (+20/-25)	7.497 (+435/ -135)
	inner	--	--	--	-0.000421 (+0.0032/ -0.0048)	1491.49 (+705/-?)	25.373 (+170/ -120)

Table 6. Best fit parameters to non-resonant background of ppp SFG data for the gradient sample (Figure 9)

Point on Gradient	$\mathbf{A_{NR}}$	$\boldsymbol{\phi_{NR}}$
1	-0.05827 (+0.1/-0.1)	19.927 (+1.2/-1.2)
2	0.10105 (+0.2/-0.2)	9.9902 (+2/-0.6)
3	0.08104 (+0.1/-0.1)	10.2715 (+1.5/-0.9)
4	0.1012 (+0.16/-0.16)	10.0471 (+1.8/-0.6)
5	0.08506 (+0.1/-0.1)	10.3301 (+1.4/-0.6)
6	0.07644 (+0.1/-0.1)	10.3539 (+1/-0.6)
7	0.08124 (+0.06/-0.06)	10.5042 (+1/-0.8)
8	0.09003 (+0.06/-0.06)	10.4235 (+1.2/-0.6)

9	-0.09486 (+0.1/-0.1)	7.24454 (+1.2/-0.6)
10	0.08488 (+0.06/-0.06)	10.5965 (+1/-0.6)
11	0.09186 (+0.06/-0.06)	10.5718 (+1/-0.6)
12	0.08287 (+0.06/-0.06)	10.7436 (+1/-0.6)
13	0.07363 (+0.06/-0.04)	10.7553 (+1/-0.8)
14	0.17252 (+0.5/-0.4)	8.3702 (+1.2/-5.4)
15	0.01994 (+0.06/-?)	10.9629

these values were fixed among all spots except for the last two. The last two spots have a very thin, submonolayer coverage of 6T molecules.

Since the mechanism of crystal growth on these two spots is still the first step of the SK growth and is therefore different from the other spots, the frequencies and HWHMs of VSFG peaks from these two spots were not assumed to be the same as the others. Also, due to the small intensity of the symmetric mode for these two spots no correct value could be assigned to the amplitude and HWHM of this mode during fitting so it was not feasible to use the same frequency and HWHM for the last two spots on the gradient. Tables 5 and 6 contain a lot of information that makes it hard to construe any meaningful trends without plotting the values. Figure 10 shows how the amplitude of the different frequency modes, interfaces, and spots change with thickness. The peak amplitudes from the VSFG spectra at spots 1 through 13 are plotted in Figure 10 since they are comparable; their frequencies and HWHMs were forced to be the same and therefore are not compared. Figure 10 shows that the absolute value of the amplitude of the symmetric mode on the

6T/glass interface is fairly insensitive to thickness changes compared to the others series. It might seem that the amplitude of the outer interface (for both modes) however seems to systematically change for the last three spots, 11 through 13. However, if the errors are taken into account this conclusion is inaccurate. Thus the amplitudes for the outer and inner interfaces for both modes don't seem to change once the errors are accounted for.

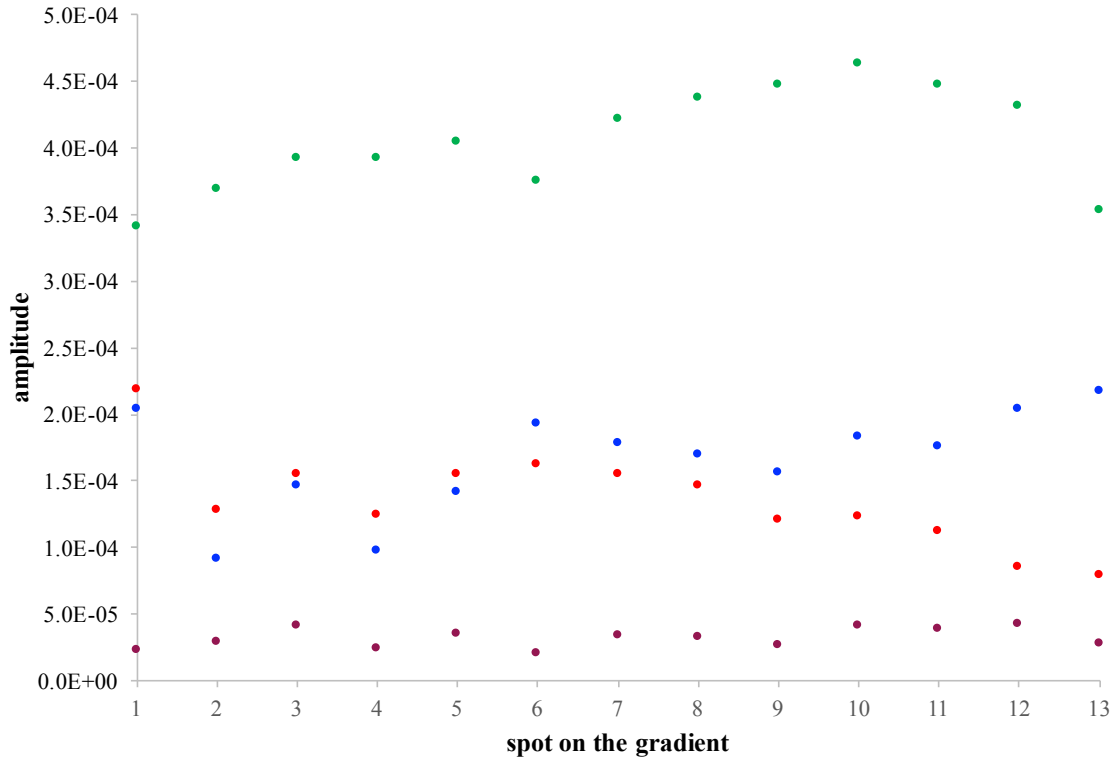

Figure 10. The absolute value of the amplitudes for spots 1 through 13 for the symmetric mode on the 6T/air interface (red), the asymmetric mode on the 6T/air interface (blue), the symmetric mode on the 6T/glass interface (purple) and the asymmetric mode on the 6T/glass interface (green).

This is not similar to what has been previously reported using x-ray studies[174], where the first monolayer has an edge-on orientation and as thickness increases this orientation becomes more end-on. The difference in the results of the VSFG and x-ray studies can be explained when one takes into account the fact that VSFG is an interface-specific technique that can provide information about the average orientation at the outer and inner interfaces.

X-ray on the other hand is not interface-specific and thus one can argue that the data collected from this method may contain information of molecular orientational from the bulk.

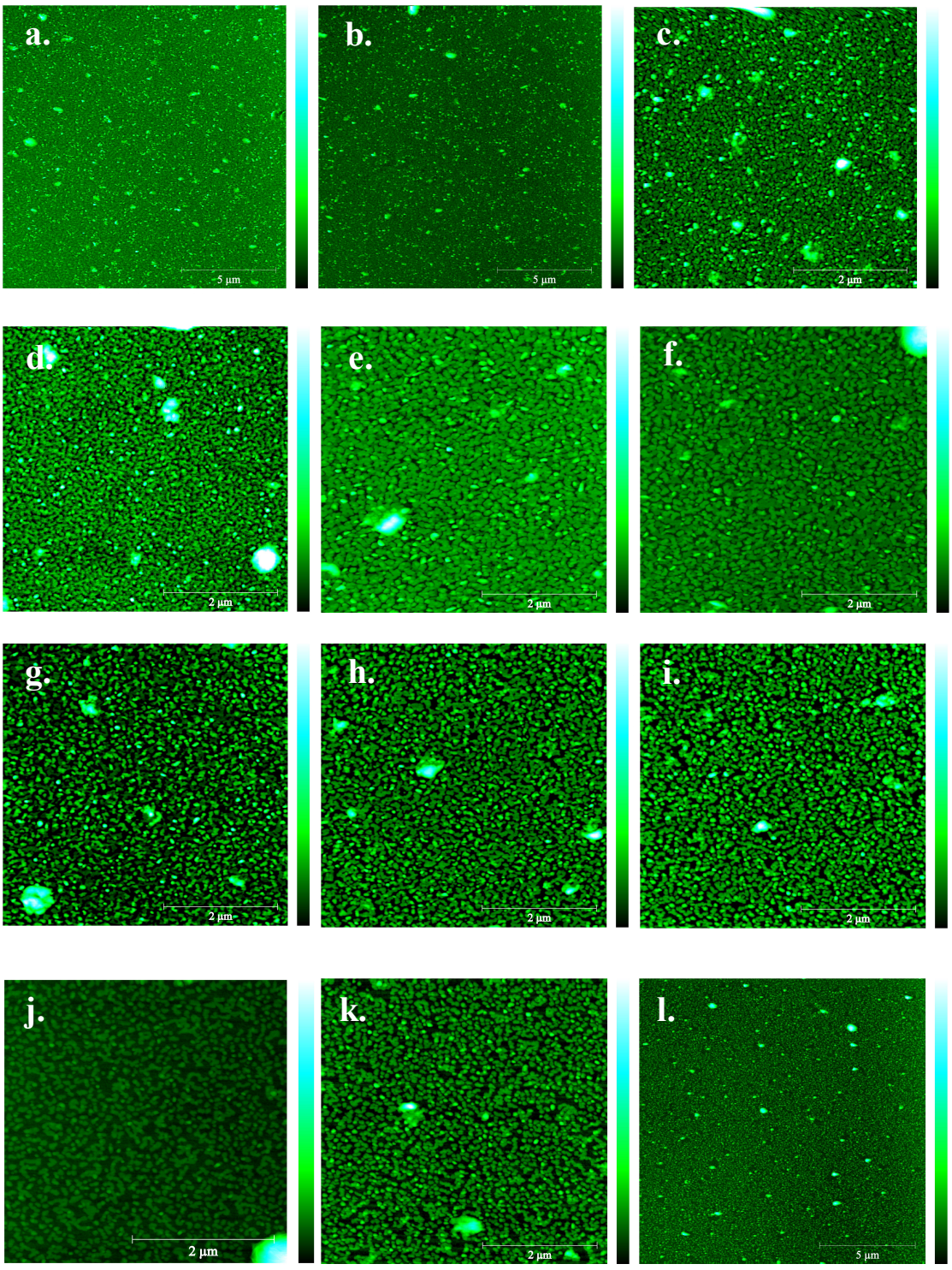

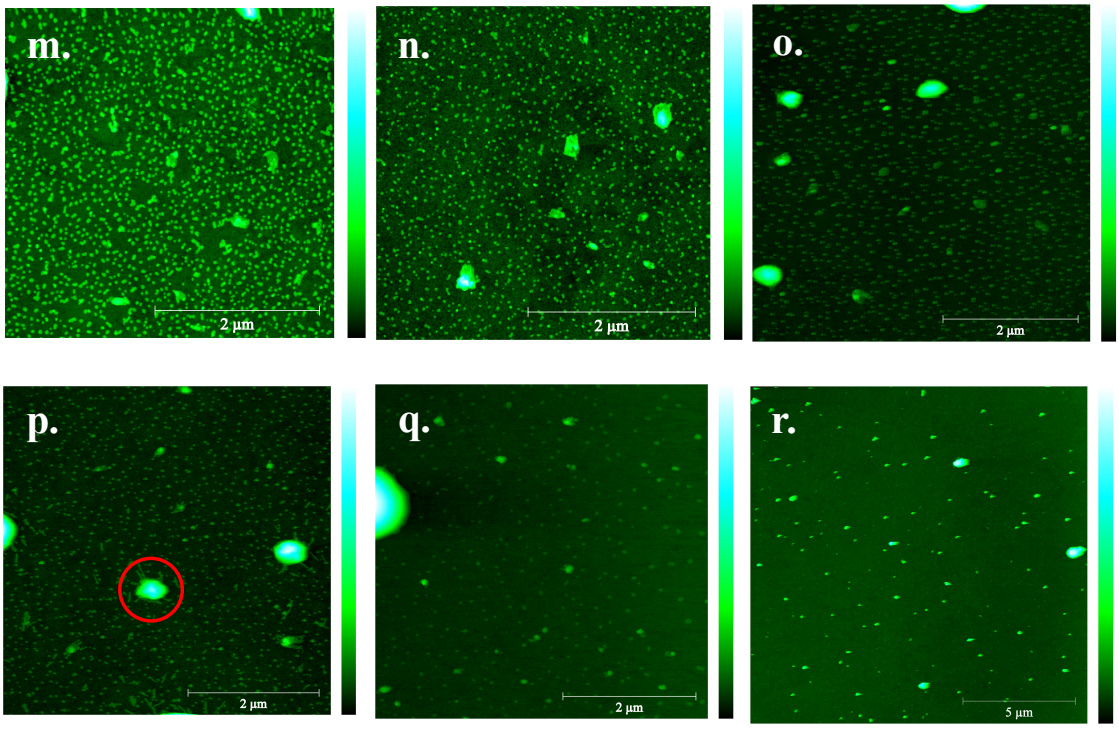

Figure 11. AFM images of the 6T gradient sample at distance of (a) 10 mm, (b) 12.5 mm, (c) 15 mm, (d) 15.5 mm, (e) 16mm, (f) 16.25 mm, (g) 16.75 mm, (h) 17 mm, (i) 17.25 mm, (j) 17.5 mm, (k) 17.75 mm, (l) 18 mm, (m) 18.15 mm, (n) 18.25 mm, (o) 18.5 mm, (p) 18.75 mm, (q) 19 mm and (r) 30 mm from the substrate edge (refer to Table 4 for thickness and spot number).

It is important to note, that the $\chi^{(2)}$ in the ppp polarization has elements from other polarization combinations and usually cannot be used individually and independently to deduce the molecular orientation. However, the ssp and sps polarization VSFG data from the single-thickness samples (Figure 6) had already clarified the orientation of this molecule. This prior knowledge of the relation between the molecular orientation and VSFG polarization is the reason we could use the results from the ppp polarization data to comment on molecular orientation

AFM images were collected on some of the spots near the end of the gradient, where there are only submonolayer or one to two monolayers of molecules. In addition, images were also collected on spots beyond the gradient and on the thicker part of the gradient for

comparison. The results are tabulated in Figure 11, ordered by thickness decrease. Frames n through p, in Figure 11 show that the 6T molecules start as sparse and far apart (the bright green dots on the dark green/black background), then the spaces between the molecules start filling in and a layer starts forming (frames m and l) and later the next layer starts building on top of the first layer (k through c). This is in accord with the Stranski-Krastanov (SK) growth transition. We believe the bigger blobs that show up in some of the frames (similar to the one circled in red in frame p) are either non-chemically bound 6T particles or other particles that could have landed on the sample during measurements.

For each frame in Figure 11 the height distribution was found using the built-in function in the Gwyddion 2.41® software. To find this distribution, areas of each image were chosen that had no anomalous blobs present. The height distributions were then fitted to a sum of Gaussian functions. Figures 12a and 12b show two representative spots at different heights on the gradient. Figure 12a, which belongs to a spot located at 17.25 mm from the edge of the substrate and on a thicker part of the gradient, shows two distinct peaks. Each peak, or height bin, is believed to illustrate a layer on the substrate. Figure 12b, located on a thinner part of the gradient, however shows only one distinct peak or molecular layer. It is important to mention that the heights (x-axis) in Figures 12a and 12b are not comparable. The heights in an AFM image are calculated relative to the maximum and minimum height features in each image making it complicated and inaccurate for height comparison. In the next step the area under each Gaussian function was calculated, which represents the number of molecules in a certain layer of the film. Then the ratio of the area for each Gaussian function to the total area of all the Gaussian functions was calculated in order to show the ratio of molecules that belong to a specific height bin or layer.

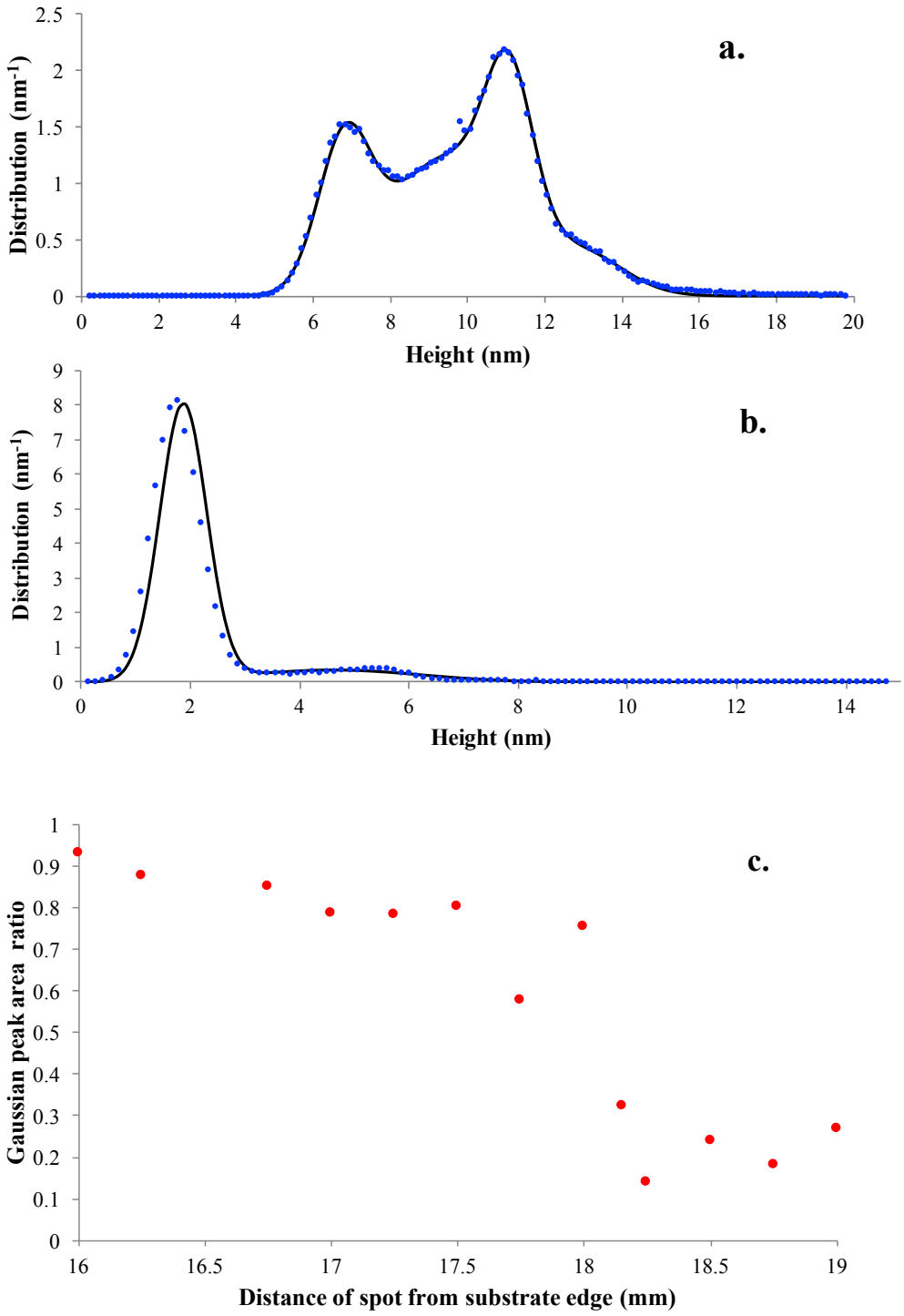

Figure 12. (a) Height distribution and Gaussian fit (black line) for spot at 17.25 mm from substrate edge, (b) Height distribution and Gaussian fit (black line) for spot at 18.25 mm from substrate edge, (c) Gaussian peak area ratio calculated from AFM images (Figure 6) for different spots on the 6T gradient sample.

Figure 12c shows the results of the Gaussian peak ratios for different thicknesses. A step at 18 mm (the thinnest spot on the gradient) can be seen on the red series, which is the point where the first particles of 6T start depositing and the AFM images confirm this as well. Also the last point on the graph reaches a ratio of nearly 1 which again confirms that the first layer nearly covers the whole surface before the next layer starts.

4. Conclusion

Through VSFG data it was shown that the average orientation of the 6T molecule on glass for the inner interface (6T/glass) is different depending on the thickness of the film. This is a result of the growth mechanism of 6T on glass, the Stranski-Krastanov (SK) growth transition, which was confirmed by AFM imaging. It was also shown, through using different polarization combinations, that the average orientation of 6T on the inner and outer interfaces are also different from one another.

Electrical Measurements on Bilayer Heterojunction Organic Solar Cells

1. Introduction

The science of efficiently harvesting the energy of the sun for electricity generation started with the discovery of a p-n junction silicon photovoltaic device in 1954.[46] Since then, solar cells have improved and become much more efficient. Today, the world's best research solar cell has an efficiency of 46%.[72, 181] This solar cell however is made of inorganic materials such as gallium, indium, and arsenic that are rare elements.

The most common type of solar cell used nowadays are made of silicon. The cost of fabricating silicon solar cells is energy-demanding and cannot be reduced any further.[47] Organic materials, such as polymers and small molecule thin films, on the other hand have the potential to be fabricated inexpensively through less energy-intensive procedures such as roll-to-roll processes.[182] In 1986, Tang and coworkers for the first time sandwiched an organic molecule, chlorophyll-a, between two metals and successfully generated a photovoltaic device.[183] Later that year, they reported a different photovoltaic device using two organic materials, one acting as an electron donor and the other as the acceptor. This bilayer junction cell was more efficient than the single-layer device.[58] Since then more efficient bilayer devices have been fabricated [184-186] but their efficiencies are not yet comparable to the silicon solar cells or other types of organic solar cells.

As discussed previously in Chapter 1, upon illumination of organic photovoltaics excitons are formed. To generate electricity, the exciton needs to be separated into its components, a hole and an electron. The separation process happens at the interface of the

donor and acceptor material, where a built-in field is present and provides the force needed to dissociate the exciton.[58] The conditions that can make this process and built-in field more effective have not been fully discerned.

We saw this as an interesting problem to tackle using a combination of electrical measurements, to obtain current-voltage (I-V) curves, and vibrational sum frequency generation spectroscopy (VSFG). This was particularly interesting because VSFG is an interface-specific technique that can potentially be used to monitor molecules at the interface between the donor and acceptor layer where the electricity generation begins.

To study the effect of this built-in field we decided to modify it. To change the built-in field a third material was deposited between the donor and acceptor, the modifier. The effect of different materials and thicknesses for the modifier, were studied.

2. Experimental

2.1. Materials

The samples were prepared on indium tin oxide (ITO)-coated glass slides (Delta Technologies, Ltd.; 120-160 nm thick ITO, sheet resistance = 8-12 Ω/sq). Poly(3,4-ethylenedioxy-thiophene)/poly(styrene-sulfonate) (PEDOT:PSS, 1.3% by weight dispersion in water), fullerene (C_{60}, 99.5%), α-sexithiophene (6T), 2,2′:5′,2′′:5′′,2′′′-quaterthiophene (4T), copper (II) phthalocyanine (CuPc, 99% dye content), aluminum phthalocyanine chloride (AlPcCl, 85% dye content), [6,6]-Phenyl C_{61} butyric acid methyl ester (PCBM, 99.5%), and HPLC grade water were used as received from Sigma-Aldrich. Regioregular Poly(3-hexylthiophene-2,5-diyl) (P3HT, electronic grade, average MW of 50000-70000 g/mol) was used as received from Reike Specialty Polymers. Some samples used P3HT that was synthesized by the Hillmyer group (samples marked by an asterisk in

Table 1). This P3HT was more than 95% regioregular with a number-average molecular weight (M_n) of 37 kg/mol.

2.2. Device Preparation

For all bilayer samples, a 1×1-inch square of ITO-coated glass was cut and the ITO was etched from three sides using the etching procedure described below. This was done to avoid short circuiting the aluminum and ITO electrodes in the assembled device. The fourth un-etched edge which was used for the connection of the measurement clips to the ITO electrode. All of the samples had a thin layer of PEDOT:PSS applied to the ITO. This facilitates the transportation of the hole to the electron donor material. This film was prepared by first sonicating the PEDOT:PSS aqueous solution for 10 minutes to ensure a homogeneous solution and then the solution was filtered through an acrodisc syringe filter of 0.45 μm pore size. The filtered solution was then spin coated on the substrate at 3000 rpm (acceleration of 1500 rpm/s) for 2.5 minutes. After spin coating, the PEDOT:PSS-covered substrate was annealed under N_2 at 110-130 °C for 30 minutes.

The samples reported here had one of two types of electron donating materials: P3HT or 6T. The 6T molecule was vapor deposited; P3HT was spin-cast. A solution of 20-25 mg of P3HT in 1.5 mL chloroform was made in a glass vial. The solution was then stirred (with a magnetic stir bar) and heated at 60 °C until all P3HT particles were visibly dissolved and the solution turned a deep orange color. The solution was filtered through an acrodisc syringe filter of 0.2 μm pore size to filter out any undissolved P3HT particles. It was then spin coated onto the substrate at 2000 rpm (acceleration of 1500 rpm/s) for 1.5 minutes.

After this, the sample was annealed for 10-15 minutes at 110-120 °C under an N_2 atmosphere.

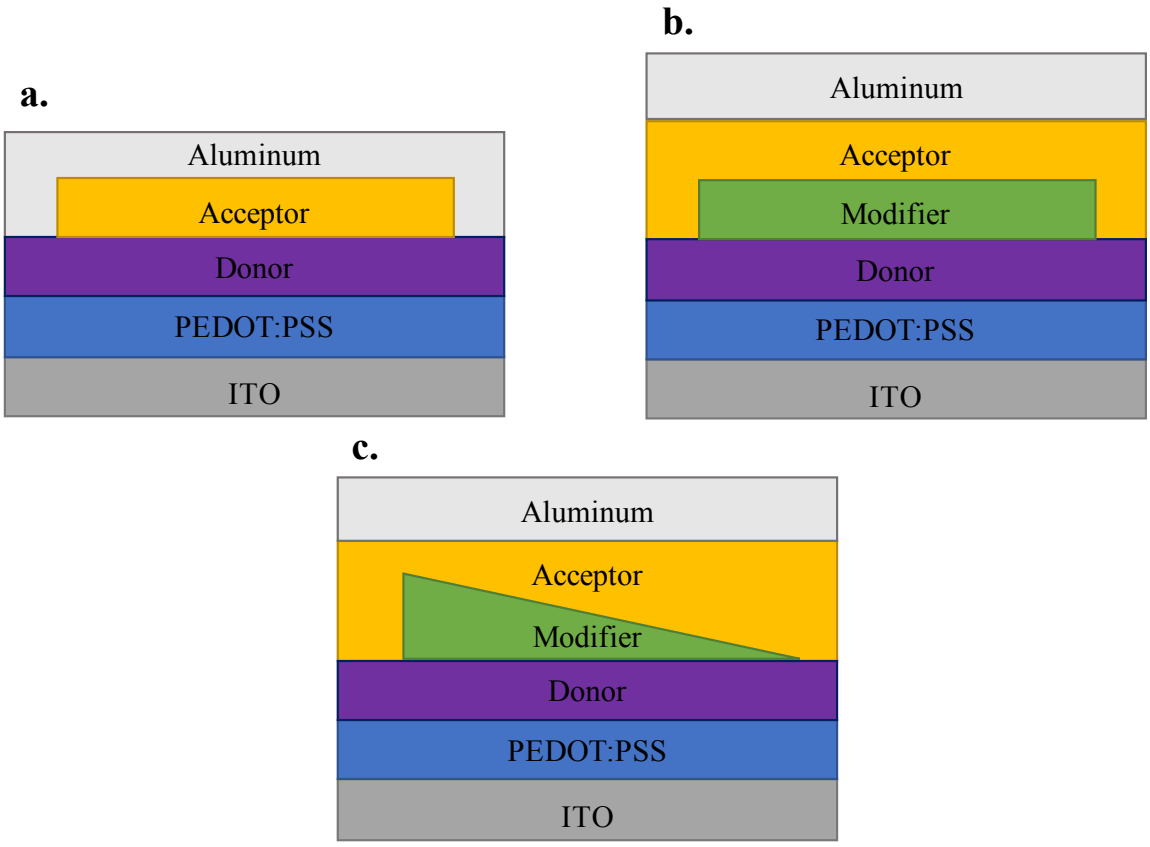

Figure 1. Samples can have (a) no modifier layer, (b) same-thickness modifier layer or (c) a gradient modifier layer.

Most samples in this study had C_{60} as the electron acceptor material, which was vapor deposited either as a layer with a constant thickness or as a thickness gradient. The gradient was deposited using an automated shutter that slowly exposed the sample while deposition was taking place.[165] All vapor depositions were done at an average chamber pressure of 5×10^{-6} Torr and deposition rate of 0.06-0.08 Å/s. Some samples had a modifier layer between the donor and acceptor layer. The modifier was either vapor-deposited as a layer with the same thickness or as a gradient (Figure 1).

In all samples we wanted to observe the role of a modifier, donor or acceptor in the cell efficiency improvement or lack thereof. For this purpose, the modifier was not deposited on the entire donor layer but as a block in the middle so that the two sides of the block did not have a modifier layer (Figure 1). Measurements on the sides and the block should show a difference in electrical behavior due to a difference in the structure of the cell.

A bulk heterojunction (BHJ) device was also prepared for comparison to the bilayer cells. This sample was made by first dissolving 7.1mg of P3HT (donor) and 7.1mg of PCBM (acceptor) in 1.5 mL of chloroform. The solution was stirred and heated at 60 °C and then 0.2 μm filtered, similar to the P3HT solution described above. The filtered solution was then spin cast onto the ITO-covered substrate at 2000 rpm (acceleration of 1500 rpm/s) for 1.5 minutes, followed by annealed for 10-15 minutes at 110-120 °C under N_2.

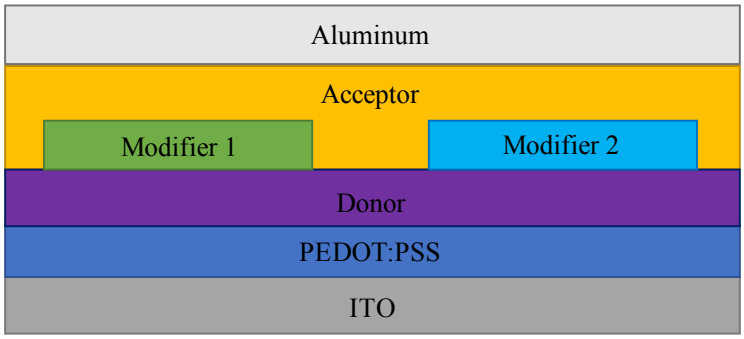

Figure 2. DM(Cu&6T)A sample, with two different modifiers on the same sample

One sample was designed so that there were two different modifier materials on the same sample (Figure 2). This enabled comparison of the two modifiers independent of errors associated with differences in devices due to various deposition environments. All the sample types are listed in Table 1.

Table 1. Summary of all samples (the samples marked with an asterisk used P3HT synthesized by the Hillmyer group)

Sample	Donor			Modifier			Acceptor			
	Material	Concentration (mg in 1.5mL chloroform)	Thickness (nm)	Material	Gradient?	Thickness (nm)	Material	Gradient?	Thickness (nm)	Concentration (mg in 1.5mL chloroform)
DA1& DA2*	P3HT	24.1	--	--	--	--	C_{60}	No	62.1	--
DA3 & DA4*	P3HT	26.0	--	--	--	--	C_{60}	No	61.0	--
DA7	P3HT	23.2	--	--	--	--	C_{60}	No	36.1	--
DA(g)1	P3HT	21.2	--	--	--	--	C_{60}	Yes	58.3	--
D(6T)A1	6T	--	70	--	--	--	C_{60}	No	36.1	--
D(6T)A9&10	6T	--	65.1	--	--	--	C_{60}	No	58.0	--
DM(4T)A2*	P3HT	22.4	--	4T	Yes	18.1	C_{60}	No	61.0	--
DM(4T)A4*	P3HT	23.8	--	4T	Yes	18.1	C_{60}	No	61.0	--
DM(6T)A1*	P3HT	23.5	--	6T	No	33.1	C_{60}	No	59.9	--
DM(6T)A4*	P3HT	22.1	--	6T	No	33.1	C_{60}	No	60.0	--
DM(6T)A10	P3HT	23.2	--	6T	No	32.6	C_{60}	No	36.2	--
DM(6T,g)A1&2*	P3HT	22.9	--	6T	Yes	17.9	C_{60}	No	60.1	--
DM(6T,g)A6*	P3HT	23.7	--	6T	Yes	17.7	C_{60}	No	59.2	--
DM(Cu)A10	P3HT	20.6	--	CuPc	No	32.5	C_{60}	No	36.2	--
DM(Cu,g)A1*	P3HT	24.1	--	CuPc	Yes	50.0	C_{60}	No	58.6	--
DM(Cu,g)A3*	P3HT	26.0	--	CuPc	Yes	50.7	C_{60}	No	61.6	--
DM(Cu,g)A4*	P3HT	23.2	--	CuPc	Yes	50.7	C_{60}	No	61.6	--
DM(Cu,half,g)A1*	P3HT	24.5	--	CuPc	Yes	9.9	C_{60}	No	58.1	--
DM(Cu,half,g)A4*	P3HT	22.2	--	CuPc	Yes	10.0	C_{60}	No	58.3	--
DM(Cu4020)A1*	P3HT	22.2	--	CuPc	Yes	40.1 & 20.0	C_{60}	No	58.5	--
DM(Al)A1&2*	P3HT	21.0	--	AlPcCl	Yes	30.0	C_{60}	No	58.7	--
DM(Al)A3*	P3HT	21.6	--	AlPcCl	Yes	31.3	C_{60}	No	64.0	--
DM(Al)A4	P3HT	21.2	--	AlPcCl	Yes	31.3	C_{60}	No	64.0	--
DM(Cu&6T)A	P3HT	20.5	--	CuPc & 6T	No	34.3 & 32.0	C_{60}	No	36.2	--
BHJ1	P3HT	7.1	--	--	--	--	PCBM	No	--	7.1

2.3. ITO Etching Procedure

To etch the ITO off of the coated glass, an etching solution was prepared by heating 10 mL of DI water to 80 °C while stirring. Then 5 mL of HCl and 1 mL of HNO_3 were added to the heated water and the solution was diluted to 25 mL with DI water. Approximately 3-5 mm of each of three edges of an ITO-coated substrate were dipped into the solution for about 10 minutes, followed by quenching by immersing the sample in DI water. A digital multimeter was used to test that the resistance between the etched part and the rest of the ITO-covered glass was off-scale. If the resistance was not high enough the etching procedure was repeated. Once the etching was successful, the substrates were cleaned by 10 minute ultrasonication in successive baths of acetone, methanol and isopropanol.[187] Finally the substrate was dried on a hot plate at 100-120 °C.

2.4. Measurement and Instrumentation

The electrical measurements on the photovoltaic cells were performed on a home-built instrument shown in Figure 3. The measurement setup was built in a covered box to decrease the amount of stray light reaching the sample while measuring. The setup was purged with dry air during measurements in order to decrease the effect of humidity. The sample was located on a mechanical stage that has the capability to systematically move the sample to different spots for measurements. This was specifically useful for comparing the electrical characteristics between the spots on a sample with and without the modifier layer or between the different spots on a sample that had a gradient modifier or gradient donor layer. In Figure 3, the stage moves in and out of the plane of the paper and the gradients were deposited in this dimension as well.

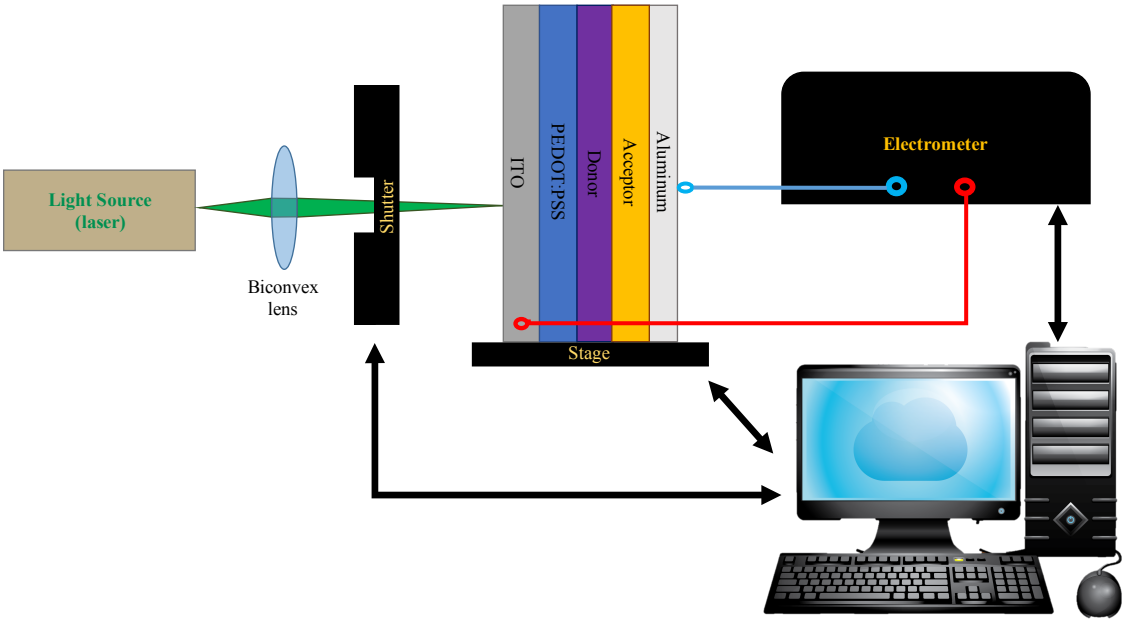

Figure 3. Electrical measurement setup for the photovoltaics

Measurements were carried out with and without the sample illumination. The differences between these two states show the photovoltaic characteristics of the samples. During each state, different voltages were applied and the respective current was measured, which in turn enabled one to construct an I-V curve. A shutter was used to block the light from reaching the sample during the dark state. During each state, a full I-V curve was generated, where the current for each voltage was measured 3 times and then averaged to account for random fluctuations. The I-V curve measurement for each state was repeated 4 times and averaged. Finally, the resulting averaged curves for the light and dark states were subtracted and a single I-V curve resulted that represented each spot on the sample. The light source that was used in this setup was a green laser from Laserglow Technologies

(532 nm CW, average output power of 153.4 mW, stability of 0.1391% RMS over 4 hours). The light was then focused onto the sample using a convex lens.

2.5. Making Smaller Voltage Steps by Using a Resistive Divider

The electrometer that was used for these measurements was a Keithley 617. This electrometer can apply voltages to the sample in steps as small as 0.1 V. However, this voltage step was not small enough to produce an accurate I-V curve so we constructed a resistive voltage divider to get to voltage steps about 1/10 of the built-in steps. The resistive divider schematic is shown in Figure 4. The divided voltage (V_{out}) from the initial voltage (V_{in}) was given by:

$$V_{out} = \frac{R_2}{R_1 + R_2} V_{in}$$

where R_1 is equal to 100 KΩ and R_2 is 10 KΩ. For our resistors, this resulted in the V_{out} being 9% of the V_{in}.

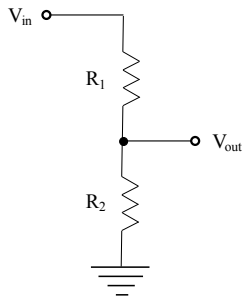

Figure 4. Resistive voltage divider, R_1=100 KΩ and R_2=10 KΩ

3. Results and Discussion

In this section, the I-V curves measured for all samples listed in Table 1 will be presented. These curves were measured over multiple spots on each sample; horizontal spots were 1 mm apart. An I-V curve was measured for each spot and a 3D plot of the curves for each

spot is presented such that a slice taken at a point on the "spot number" axis shows the I-V curve for that spot.

3.1. Samples without a Modifier Layer

The curves of the DA1 sample are presented in Figures 5 and 6. There are two curves for this sample because each sample has 3-5 separate aluminum stripes (one of the two electrodes) and each stripe can be treated as a separate cell. For the DA1 sample spots 5 through 16 had the acceptor layer and the rest of the spots only had the donor (Scheme 1a). In the DA2 sample spots 6 through 17 had the acceptor layer. Spots 5 through 17 had the acceptor layer in samples DA3 and DA4. Finally, spots 5 through 17 had the acceptor in sample DA7.

The figures show that the current on the spots with only the donor present mainly have positive values regardless of the voltage. However, the current does change into more negative values faster with voltage change for the spots with an acceptor layer. This faster change in the current directionality does have a big influence on the fill factor and improvement in the cell efficiency only for some samples, one of the aluminum stripes on DA1, DA3 and DA4. In other words, for some samples we have been able to make the cells more efficient by depositing an acceptor layer.

The charge generation mechanisms are different between single layer and bilayer heterojunction cells. It has been shown,[182] that for a single layer device (an organic material sandwiched between two electrodes) a Schottky junction is formed between the p-type organic and the electrode with a lower work function (between P3HT and PEDOT:PSS/ITO).[188] Close to the contact, the Schottky contact causes band bending near

the depletion region in the depletion region. So the photovoltaic activity of single layer devices is a direct result of the interaction between the organic material and the electrode.

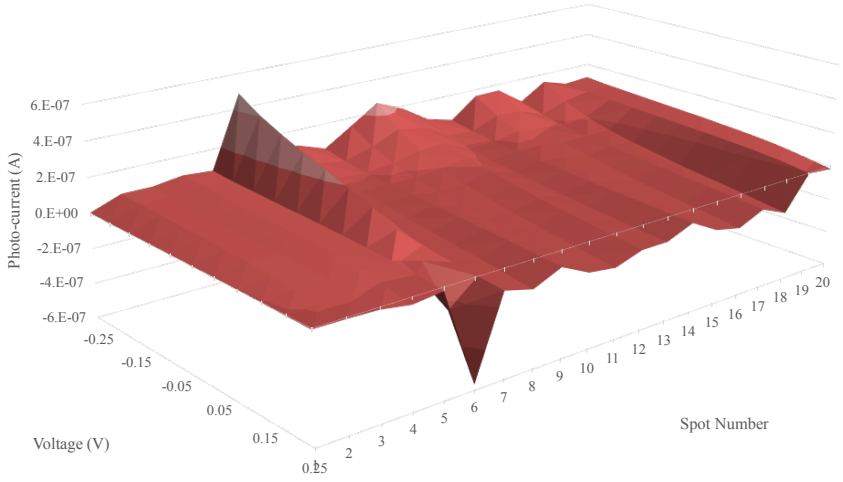

Figure 5. I-V curves for the DA1 sample on aluminum stripe 1.

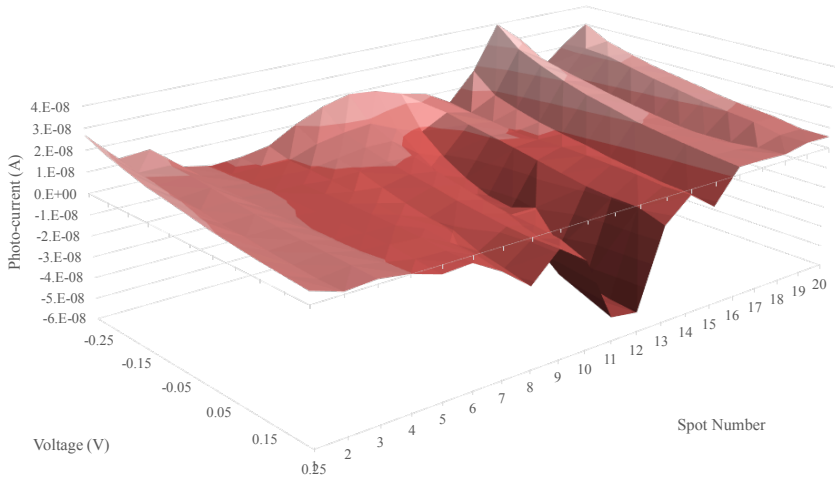

Figure 6. I-V curves for the DA1 sample on aluminum stripe 2.

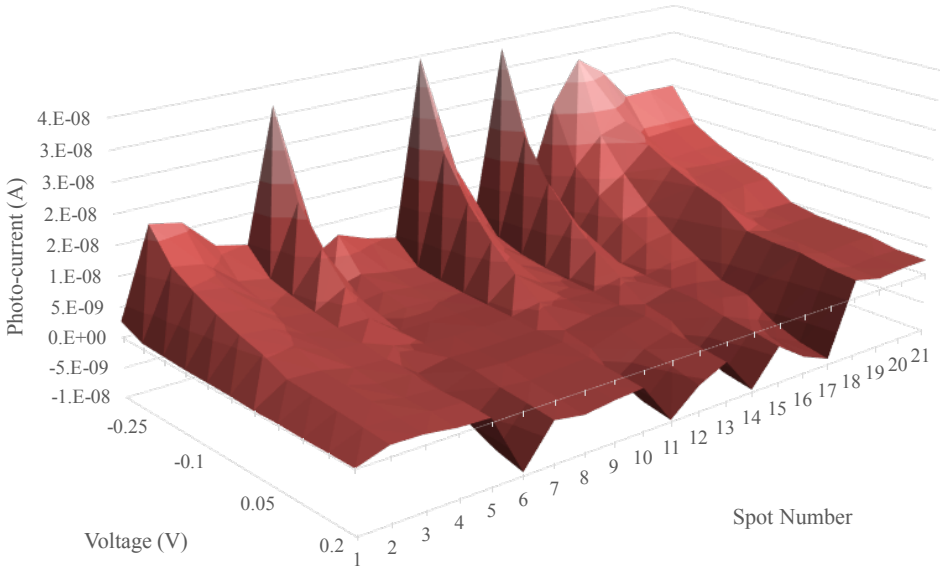

Figure 7. I-V curves for the DA2 sample.

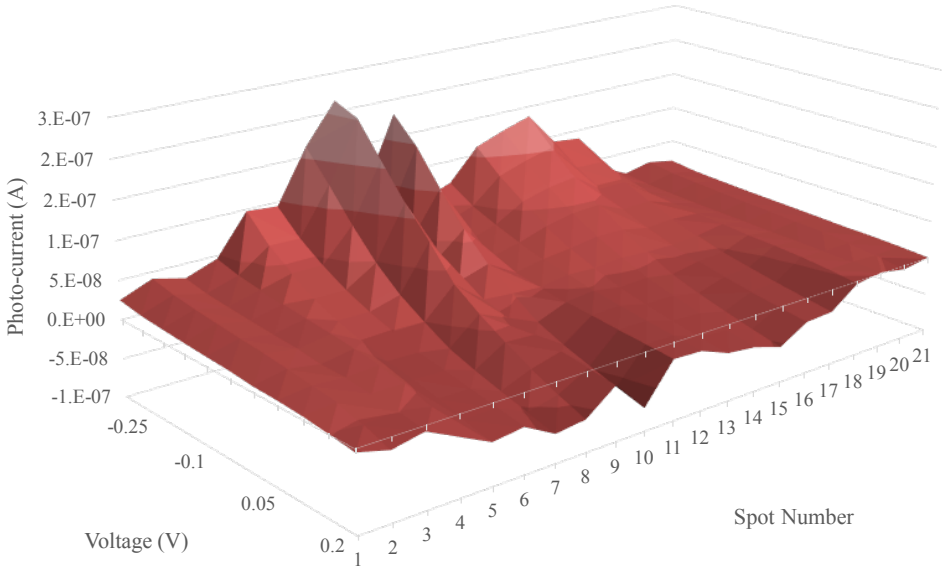

Figure 8. I-V curves for the DA3 sample on aluminum stripe 1.

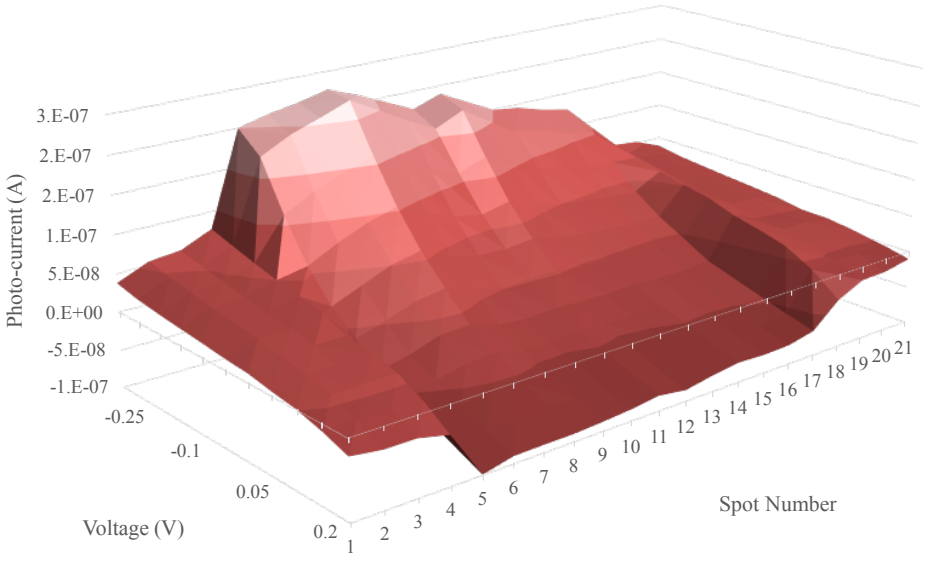

Figure 9. I-V curves for the DA3 sample on aluminum stripe 2.

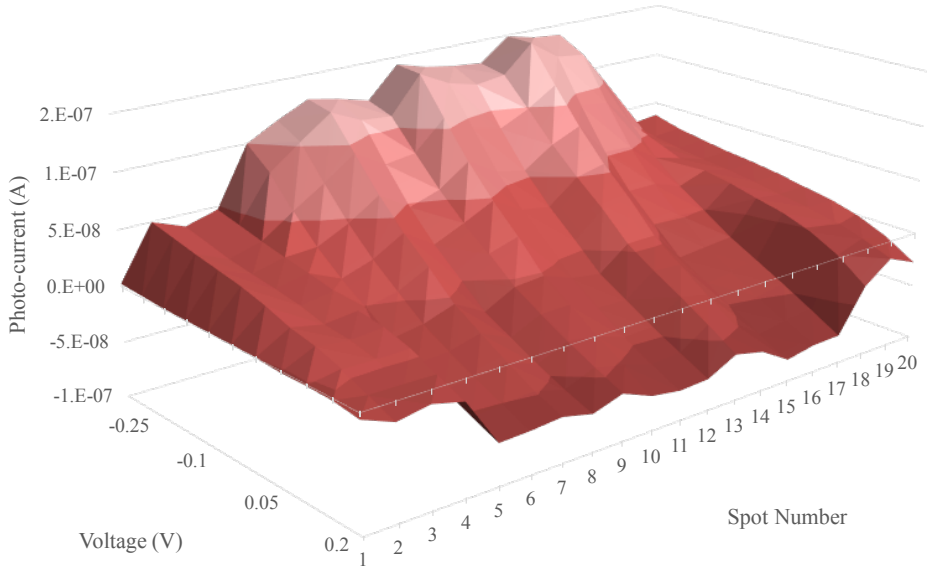

Figure 10. I-V curves for the DA4 sample.

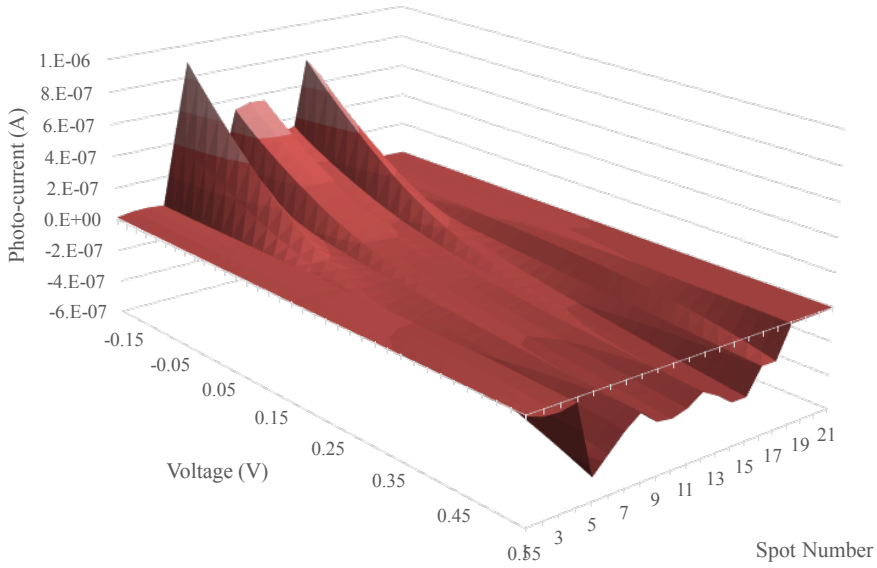

Figure 11. I-V curves for the DA7 sample.

In a bilayer heterojunction however the exciton dissociation is due to the differences in ionization potential and electron affinity of the donor and acceptor materials.[182] It has been shown, both experimentally[189-191] and theoretically,[192] that at the interface of the donor and acceptor materials an interfacial dipole forms. This dipole can help favorably in exciton dissociation if it is oriented properly. It can also help in stabilizing the charge-separated state by a repulsive force between the interface and the free charges that keeps the charges from recombining. The advantage of the bilayer over the single layer device is that in the former the chances of recombination are lower since the electrons travel in the acceptor and the holes in the donor.

As mentioned due to lower chance of recombination it is expected for the bilayer heterojunction cell to have a better performance, however our measurements do not show this. The first reason for explaining this discrepancy is accounting for the trap densities.

The bilayer devices might have enough carrier trap sites that will cause trap-assisted recombination. This keeps the device from becoming more efficient from its single layer counterpart. Typically, photovoltaic devices are manufactured and sometimes measured under vacuum. Our samples however, were not made nor measured under vacuum thus making them more prune to oxidation and trap site build-up.

Another reason for the samples with an acceptor layer to not be as efficient might be due to the quality of the organic/Al interface. We observed in some cases that the aluminum would get flaky during sample mounting and measurement, which could degrade the performance of the bilayer heterojunctions.

Samples in Figures 12 through 14 are very similar to samples in Figures 5 through 11 except that the donor material in these samples was vapor-deposited 6T. In samples D(6T)A1, D(6T)A9, and D(6T)A10, spots 6 through 17 had the acceptor layer. The overall I-V curves of Figures 12 through 14 are similar to Figures 5 through 11 where the current changes more with the voltage where the acceptor material is present. As the figures show, the I-V curves for 6T are more reproducible than the P3HT samples.

It is worth noting that sample D(6T)A1 had the biggest short-circuit current compared to all other samples (Figure 12). However samples D(6T)A9 and D(6T)A10 (Figures 13 and 14) did not have as high of a short-circuit current. This might be due to the fact that the acceptor layer is about half the thickness on D(6T)A1 compared to the two other samples. Less thickness means less acceptor material for the electron to transport through and less chance of encountering a trap site and recombination. We tried to reproduce the results of this sample but unfortunately the other samples all had short circuits and did not function.

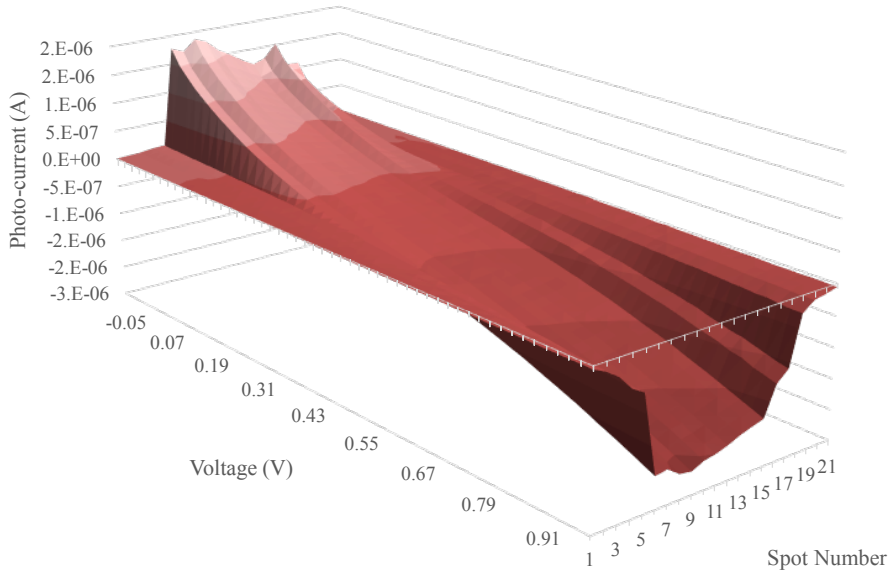

Figure 12. I-V curves for the D(6T)A1 sample.

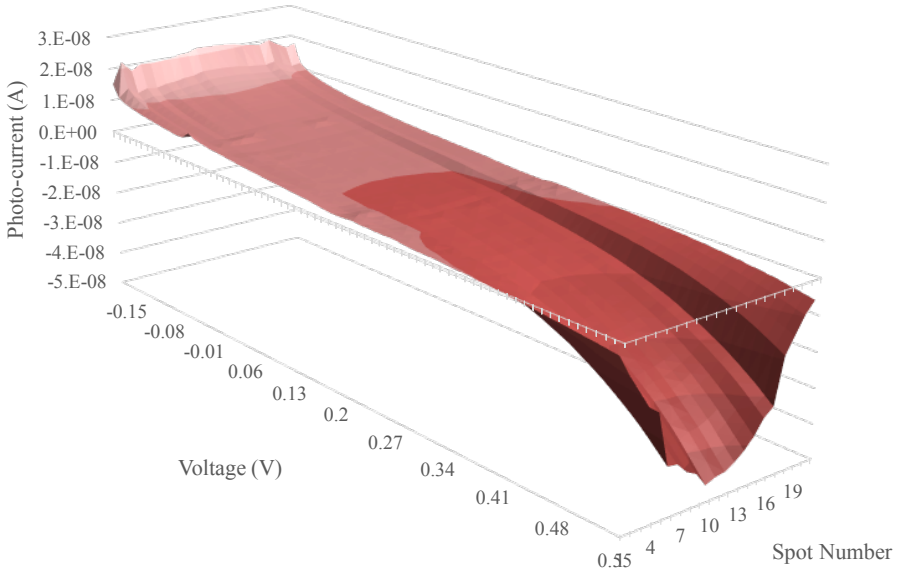

Figure 13. I-V curves for the D(6T)A9 sample.

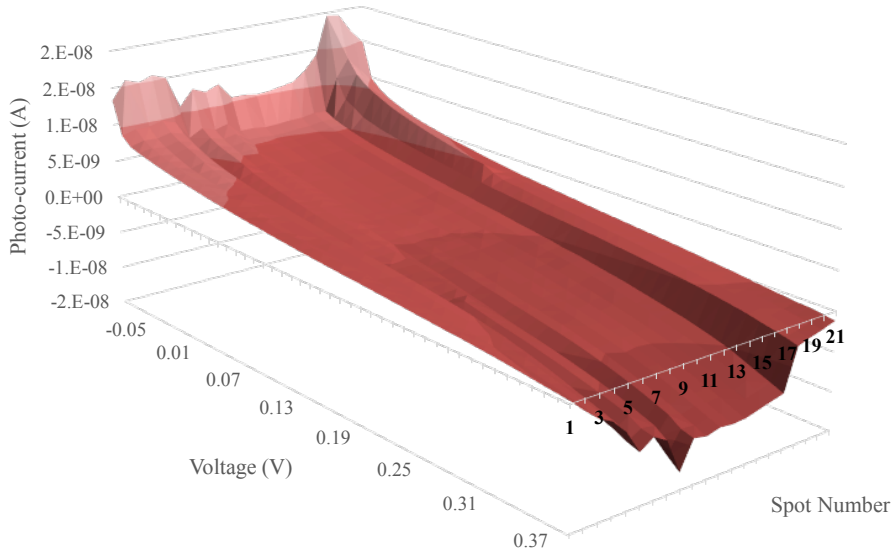

Figure 14. I-V curves for the D(6T)A10 sample.

Figure 15 shows the I-V curve for the DA(g)1 sample. On this sample, the acceptor was deposited as a gradient with maximum nominal thickness of 58 nm to see if the different thicknesses had an effect on the I-V response. Spots 6 through 17 had the acceptor layer, and spot 6 is located on the thicker end of the gradient.

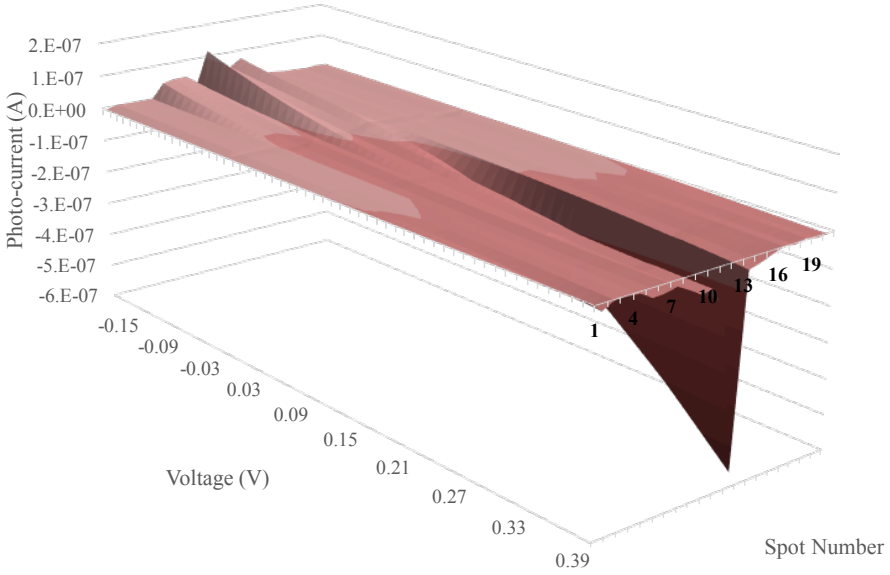

Figure 15. I-V curve for the DA(g)1 sample.

On all samples with a gradient acceptor of modifier layer we expected to see an increase or decrease or a local maximum with the change in thickness on the gradient. Figure 16 shows how the short circuit current (I_{SC}) changes over the sample and the gradient. On parts of the gradient the short-circuit current seems to change polarity and on spot 13 it switches back again. Since the gradient is the thinnest at this end, it appears that when the acceptor thickness reaches some minimum value, the bilayer begins to function like a single donor layer. This is probably due to incomplete coverage of the acceptor material. Assuming a linear thickness gradient from 58 nm at spot 6 to effectively zero nm at spot 17, this means that somewhere around 15 – 20 nm of C_{60} the monolayer begins to be complete when deposited on 6T. This seems to show a change in the type of carrier that is generating electricity in the donor or acceptor layer.

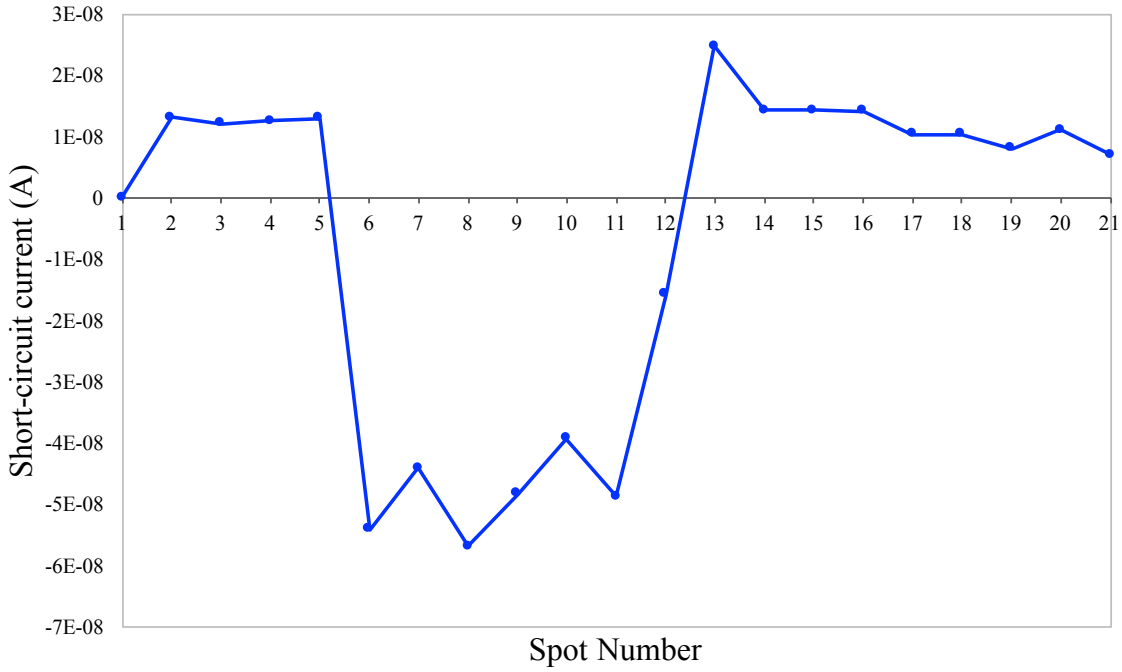

Figure 16. Short-circuit current versus spot number for the DA(g)1 sample.

The short-circuit current is the current when there is no applied voltage to the solar cell. One of the factors that affects the I_{SC} is the absorption spectrum of the active layers and how light propagates through the acceptor and donor layers. This is important because it affects the generation and diffusion of photogenerated species and the electric field distribution inside the device plays a crucial role especially in a device with a reflective metal electrode.[193] Figure 12 shows that the absolute value of the I_{SC} for spots 6 through 11 are the highest, meaning the light propagates favorably at those gradient thicknesses. These thicknesses are between 58 to 29 nm.

3.2. Samples with a Modifier Layer

3.2.1. Samples with 4T as Modifier

Figures 17 and 18 depict the I-V curves for the DM(4T)A2 and DM(4T)A4 samples. Both of these sample have 2,2′:5′,2′′:5′′,2′′′-quaterthiophene (4T) as the modifier layer between the donor (P3HT) and acceptor (C_{60}) materials. The modifier was deposited as a gradient with maximum nominal thickness of 18 nm. Spots 1 through 15 had the modifier layer.

The I-V curves do not seem to show any change at the regions with and without the modifier for sample DM(4T)A2. However for sample DM(4T)A4, Figure 19 shows a gradual increase in the absolute value of the current (up to spot 7) and then a decrease with change in gradient thickness, again pointing to the optimal thickness of light propagation that works in the favor of more I_{SC} generation. This corresponds to a nominal 4T thickness of about 9 nm.

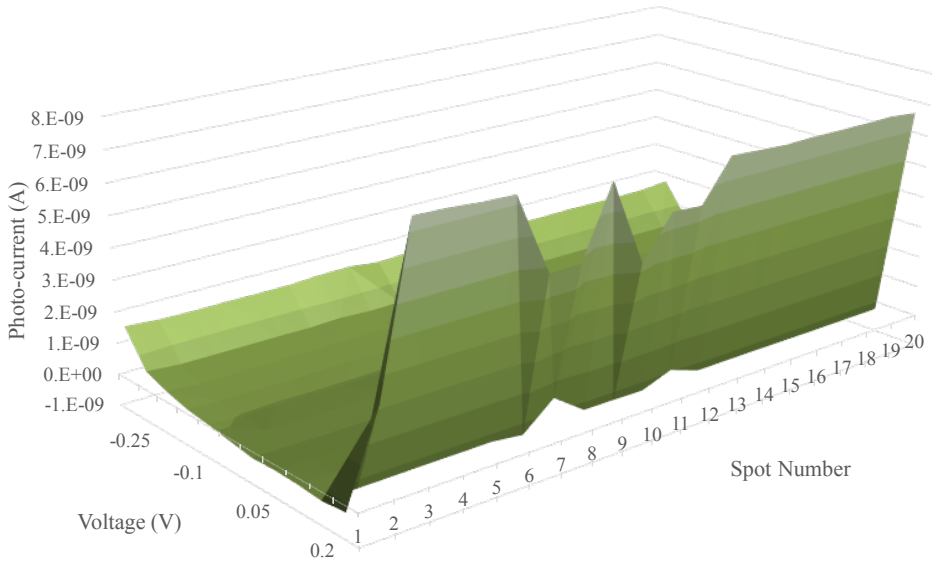

Figure 17. I-V curves for the DM(4T)A2 sample.

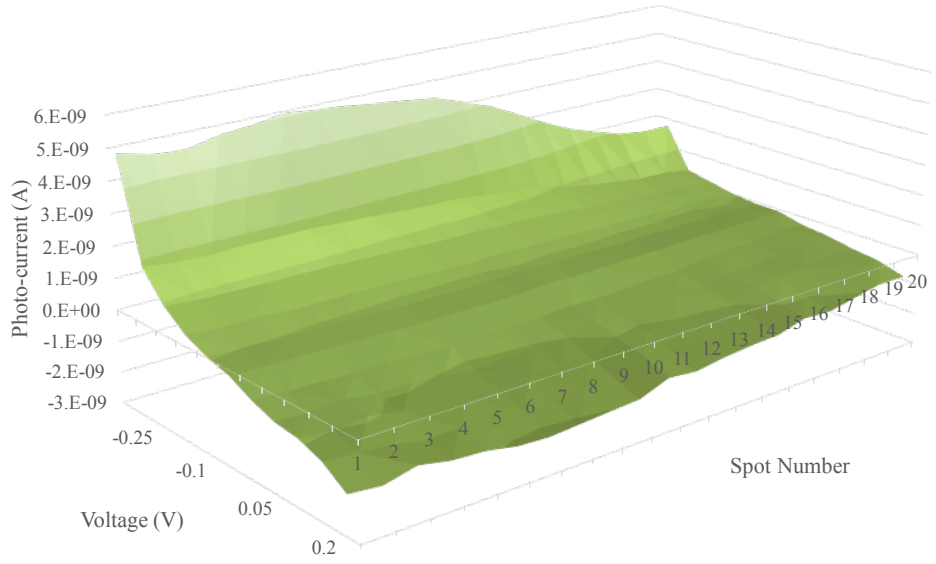

Figure 18. I-V curves for the DM(4T)A4 sample.

It is important to note that although the light propagates through the donor and that is normally the material where the exciton is generated in, one has to take into account the back-reflectance from the metal electrode surface as well.

It is also worth noting that the currents for these samples were an order of magnitude lower than the smallest currents on the previous group of samples. The short-circuit current is directly related to the number of photons that can be absorbed by the material.[182] Thus, the drop in current might be due to the drop in the absorbance spectra of 4T around 532 nm, which is the wavelength of our light source.[194] But probably a more important reason is that the energy levels of 4T don't align very well with the donor and acceptor energy levels in such a way that makes it an inefficient modifier. The HOMO and LUMO of 4T is not aligned between that of the donor and acceptor,[195-197] making it hard for the separated electrons to migrate to the acceptor spontaneously.

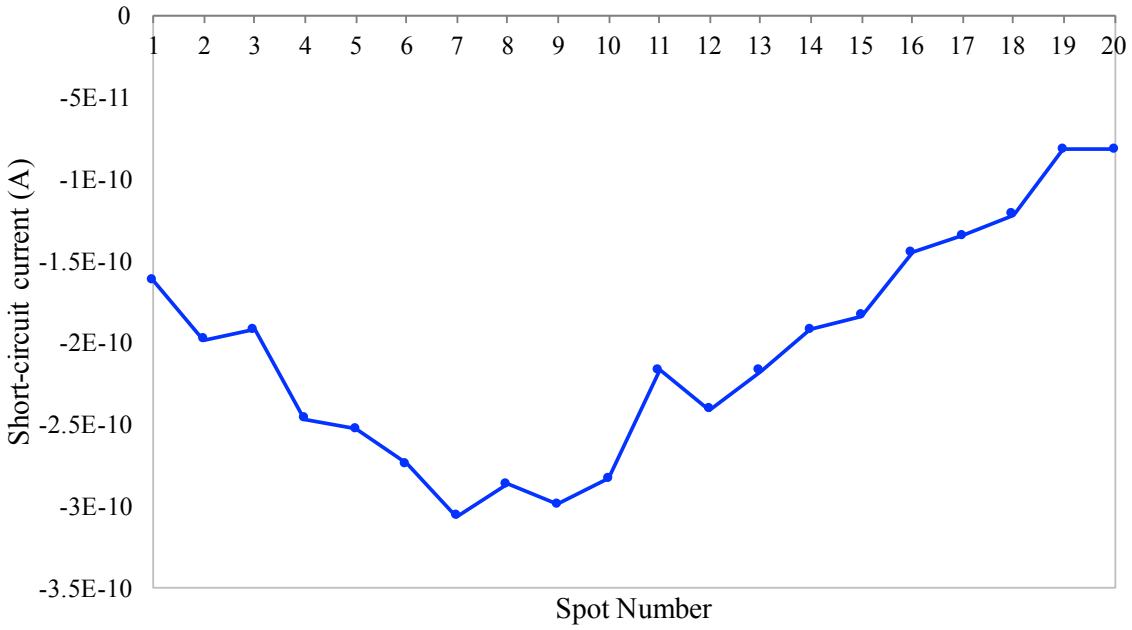

Figure 19. Short-circuit current versus spot number for the DM(4T)A4 sample.

3.2.2. Samples with 6T as Modifier

The next set of figures, 20 through 26, show the I-V curves for three samples with 6T as the modifier layer. In all these samples 6T was deposited as a block, with the same

thickness. For sample DM(6T)A1 on the first aluminum stripe (Figure 20) spots 6 through 17 and on the second aluminum stripe (Figure 21) spots 5 through 16 have the modifier layer. On sample DM(6T)A4 spots 6 through 16 have the 6T modifying layer. Lastly, spots 4 through 16 have 6T in sample DM(6T)A10. The last sample, DM(6T)A10, has half the thickness of the acceptor material, C_{60}, than the first two samples.

It is interesting to point out that on the first two samples, the spots with the 6T modifying layer seem to change less with change in voltage. Figure 27, shows the short-circuit current for these samples. It is hard to find a trend amongst these samples; for sample DM(6T)A1 it seems like the current on the spots with the modifier changes polarity however this can hardly be said for samples DM(6T)A4 and DM(6T)A10, where this change in polarity seems to be random and not following any trends.

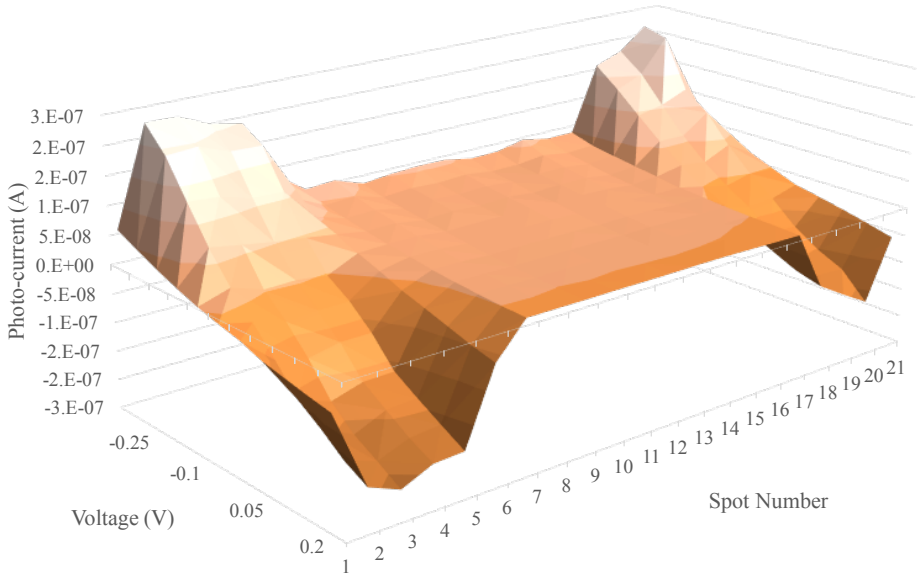

Figure 20. I-V curves of the DM(6T)A1 sample for aluminum stripe 1.

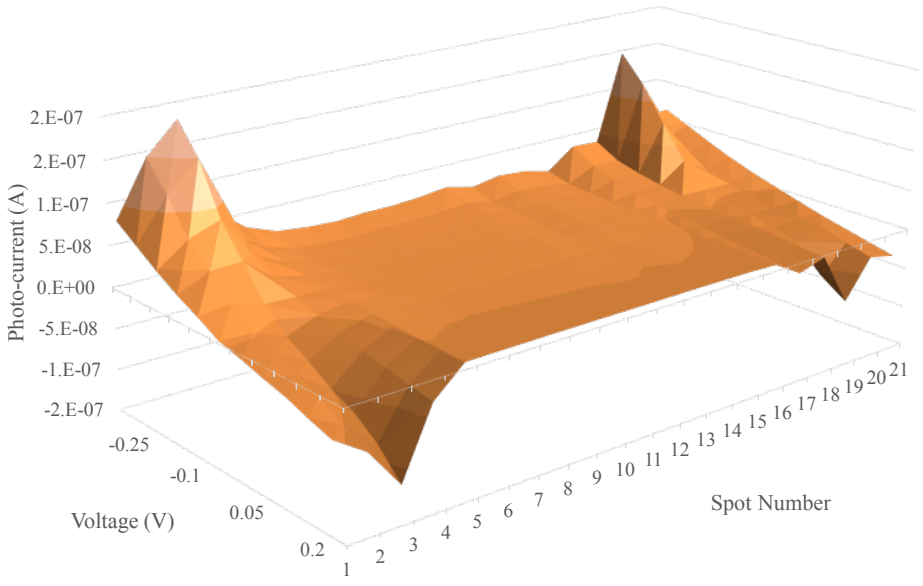

Figure 21. I-V curves of the DM(6T)A1 sample for aluminum stripe 2.

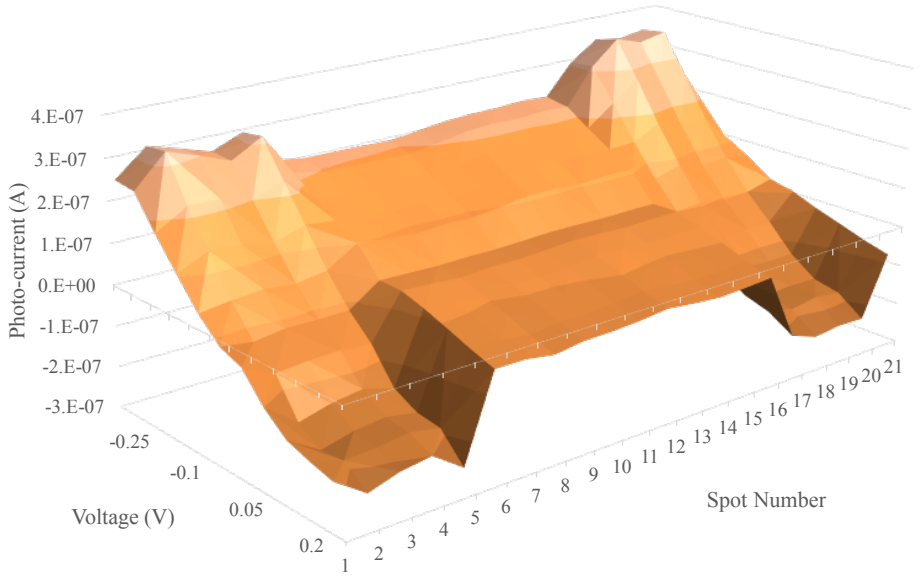

Figure 22. I-V curves of the DM(6T)A4 sample on aluminum stripe 1.

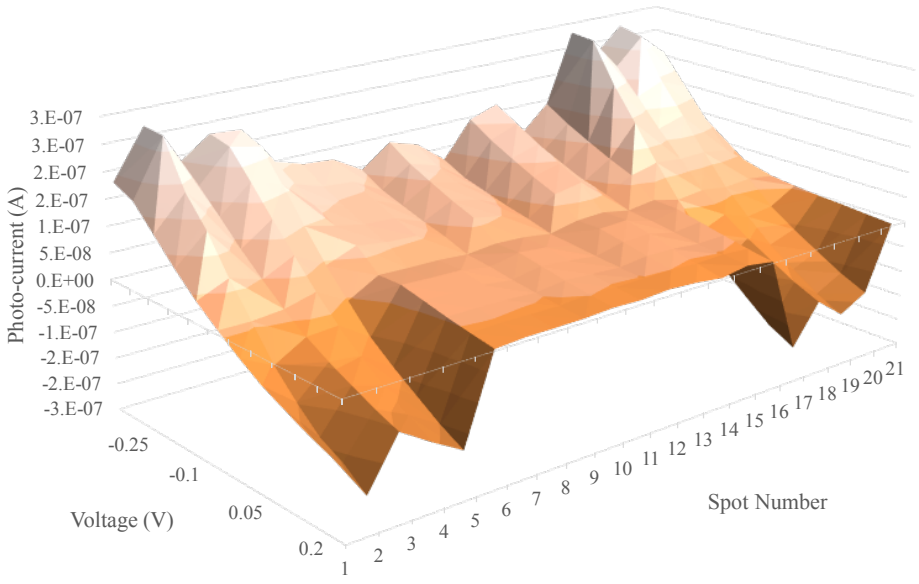

Figure 23. I-V curves of the DM(6T)A4 sample on aluminum stripe 2.

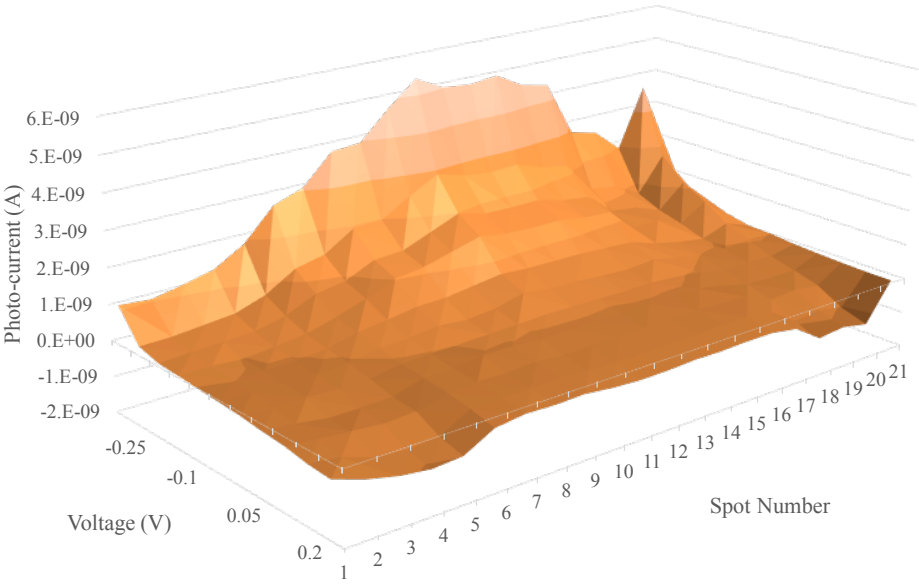

Figure 24. I-V curves of the DM(6T)A4 sample on aluminum stripe 3.

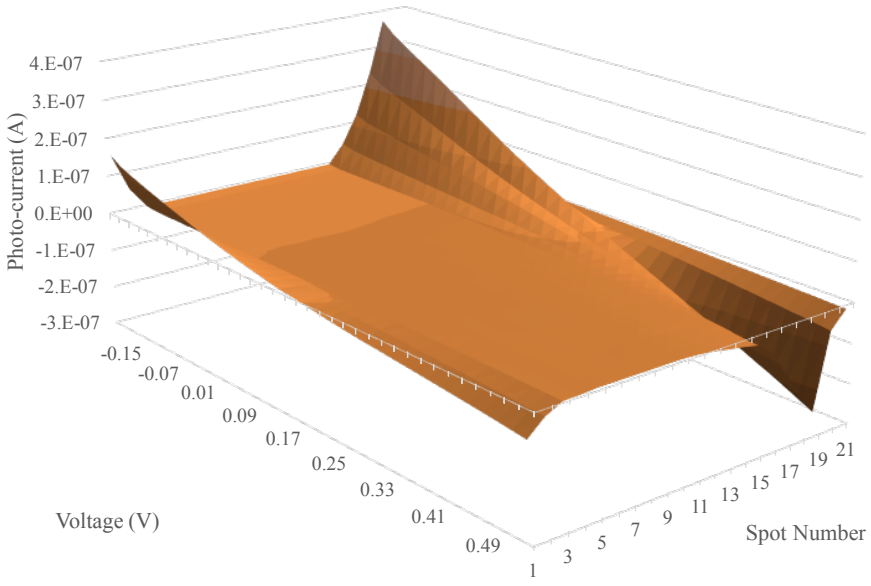

Figure 25. I-V curves of the DM(6T)A10 sample on aluminum stripe 1.

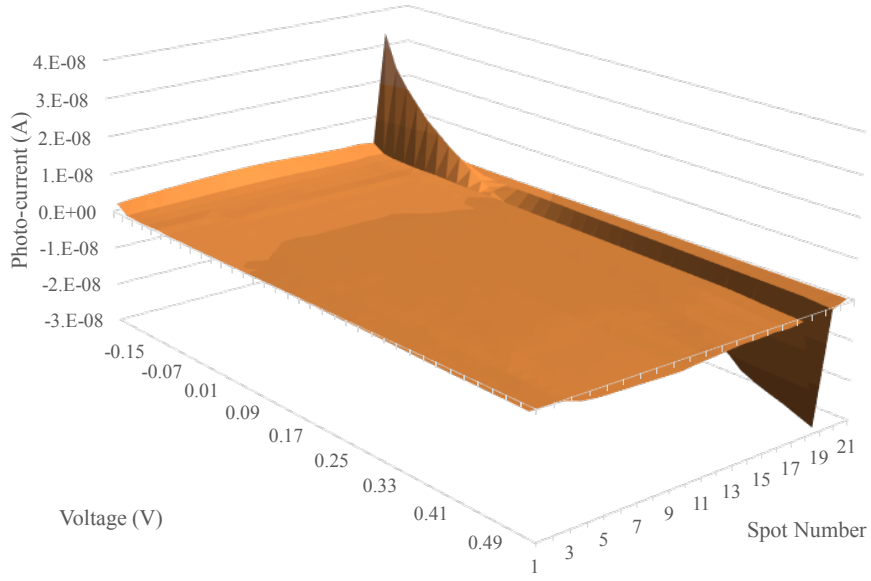

Figure 26. I-V curves of the DM(6T)A10 sample on aluminum stripe 2.

It is also hard to see any trend in the absolute value of the current between samples on spots with and without the modifying layer. For some samples, the absolute value increases

on the modifier, for some it does not change much and for others it decreases. Unfortunately, results from this set of samples were inconclusive and were very hard to reproduce.

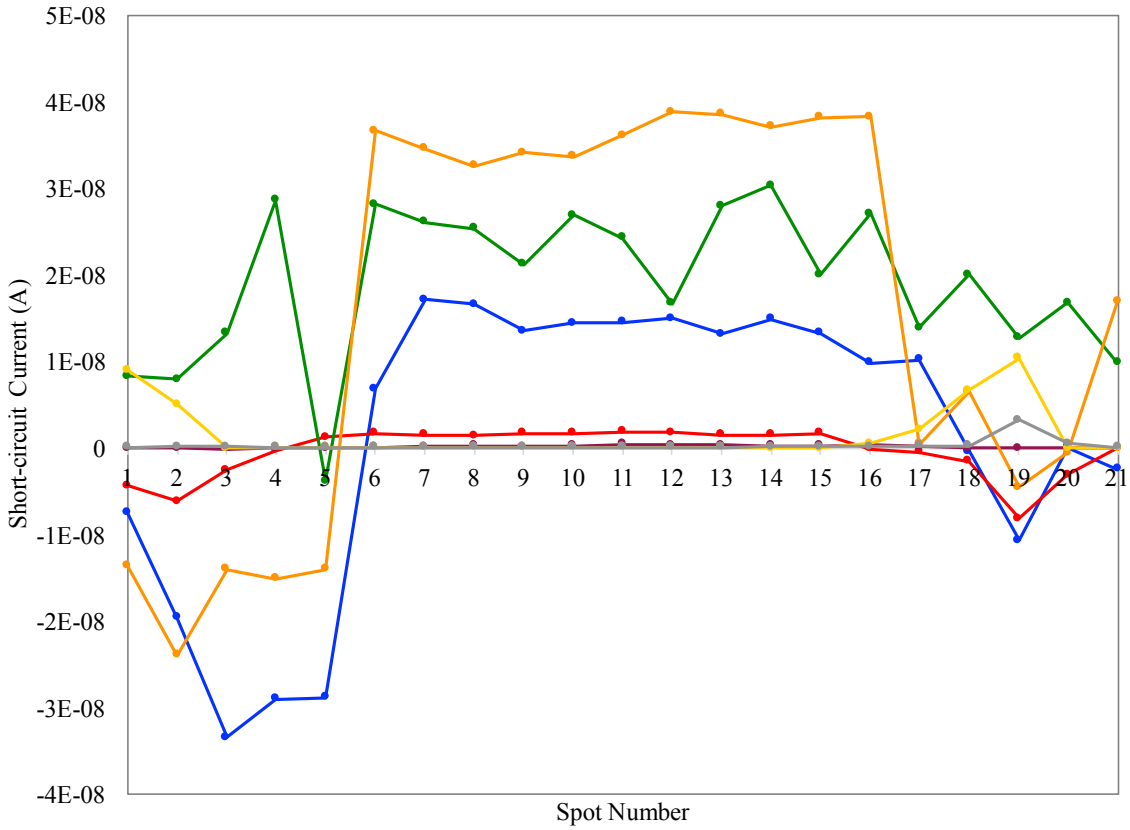

Figure 27. Short-circuit current versus spot number for (blue and red) sample DM(6T)A1 aluminum stripes (corresponds with Figures 20 and 21), (purple, green and orange) sample DM(6T)A4 aluminum stripes (corresponds with Figures 22, 23 and 24) and (yellow and gray) sample DM(6T)A10 stripes (corresponds with Figures 25 and 26).

The next set of samples (Figures 28 through 32) also had 6T as the modifying molecule, however they are deposited as a gradient this time. All samples had 6T from spots 1 through 15, where spot 1 had the maximum thickness of the gradient. The nominal thickness of 6T at the maximum on the gradient was 18 nm. It is again hard to spot any trend from looking

at merely the I-V curves in Figures 28 through 30. It seems like each sample behaves differently and this specific type of sample was not reproducible.

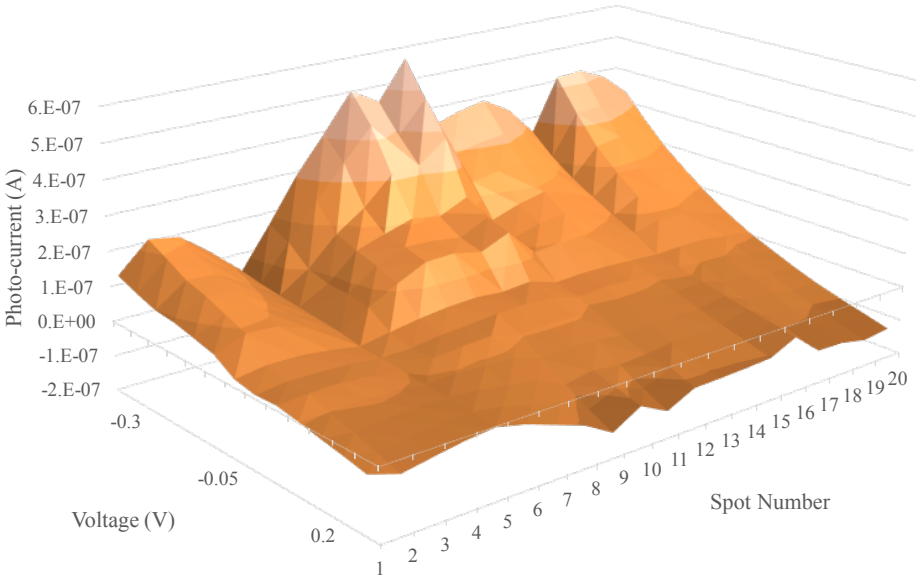

Figure 28. I-V curves of the DM(6T,g)A1 sample.

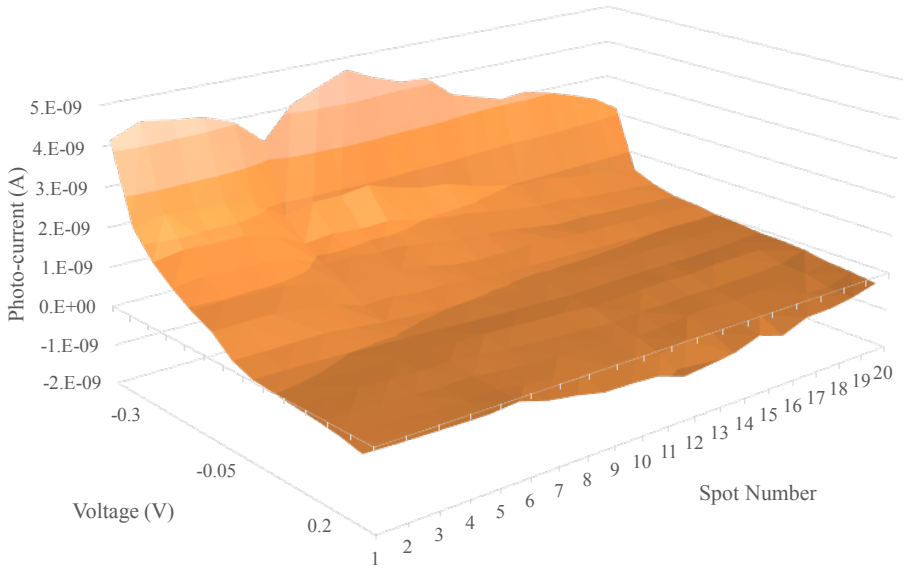

Figure 29. I-V curves of the DM(6T,g)A2 sample.

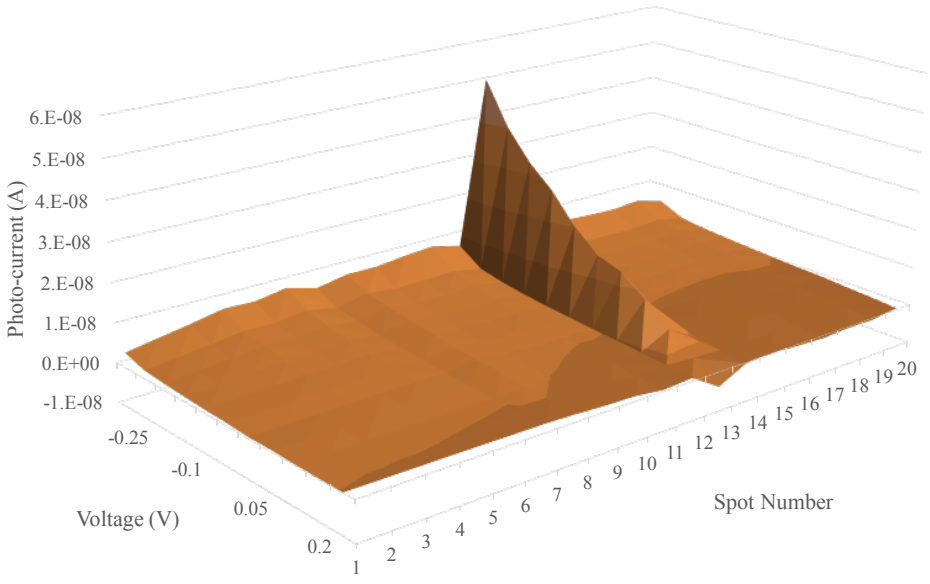

Figure 30. I-V curves of the DM(6T,g)A6 sample

Figure 31 shows the I_{SC} for the different spot numbers on the three samples. It seems like the I_{SC} on samples DM(6T,g)A1 and DM(6T,g)A6 do not change polarity. They also do not seem to follow a trend and look randomly distributed.

However the I_{SC} for sample DM(6T,g)A2 seems decrease with the decrease in the gradient (the inlet graph in Figure 31). This trend is very similar to what was seen for sample DM(4T)A4 (Figure 18) where the I_{SC} first increased in absolute value and then started decreasing. The spot at which this change occurs for DM(4T)A4 is spot 7, whereas this spot for DM(6T,g)A2 is spot 9. These spots are comparable since the maximum thickness of the gradient, the gradient width and where the gradient starts (on the edge) are the same for both samples. It is interesting that both molecule behave the same and respond to the change in absolute value of I_{SC} at a thickness very close to one another.

The little difference in the thickness between the 4T and 6T sample where the absolute value of the I_{SC} starts changing can be associated with the fact that these are two different

molecules with different optical properties, even though they are chemically very much alike. The other reason for this small difference is because the donor material in both cases, P3HT, was spin cast on the substrate and this results a different thickness every time due to slight differences in the concentration of the initial P3HT solution.

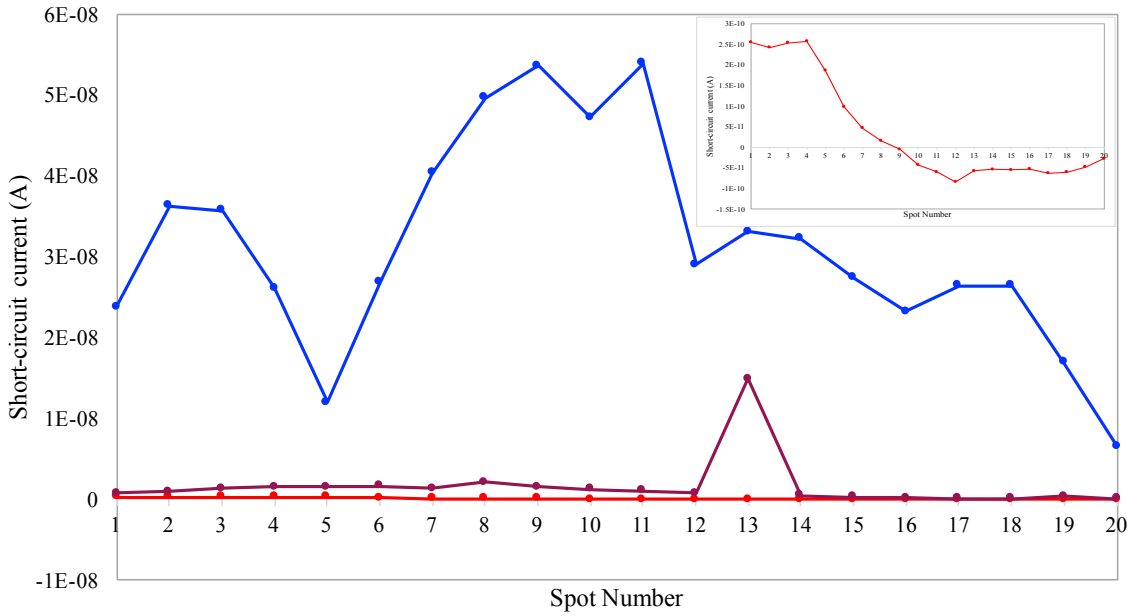

Figure 31. Short-circuit current versus spot number for samples (blue) DM(6T,g)A1, (red) DM(6T,g)A2 and (purple) DM(6T)A6. The inset graph shows only the red curve.

3.2.3. Samples with CuPc as Modifier

Figure 32 shows the I-V curves for sample DM(Cu)A10. In this sample, the modifier is copper (II) phthalocyanine (CuPc), which is deposited as a block with the same thickness from spots 5 through 17.

Again, the spots that have the CuPc layer behave differently than the spots without it; the current on these spots change less with the differing voltage. It is also worth noting that the I-V curves for the spots with the CuPc block look very similar and reproducible, unlike the samples that had 6T as the modifying molecule.

Figures 33 through 39 show the I-V curves for samples DM(Cu,g)A1, DM(Cu,g)A3 and DM(Cu,g)A4, which have CuPc as the modifier deposited as a gradient. The maximum thickness of CuPc on the gradient for these samples was nominally 50 nm. Spots 6 through 16 for sample DM(Cu,g)A1, 6 through 17 for sample DM(Cu,g)A3, 5 through 16 for sample DM(Cu,g)A4 have the CuPc modifying layer. In all these samples, the spot with a lower number (6 or 5) has the maximum thickness of the gradient.

Figures 40 through 42, show the data for samples DM(Cu,half,g)A1 and DM(Cu,half,g)A4 which also have a gradient of CuPc modifier. The difference between these samples and the previous set is that the gradient on these are not deposited in the middle of the sample, it starts a couple spots in and continues all the way to the end of the sample edge. Also the gradient is much thinner on these samples with CuPc nominal thickness of 10 nm at the maximum. Spots 5 through the end have the modifier layer, where spot 5 is located on the maximum thickness of the gradient.

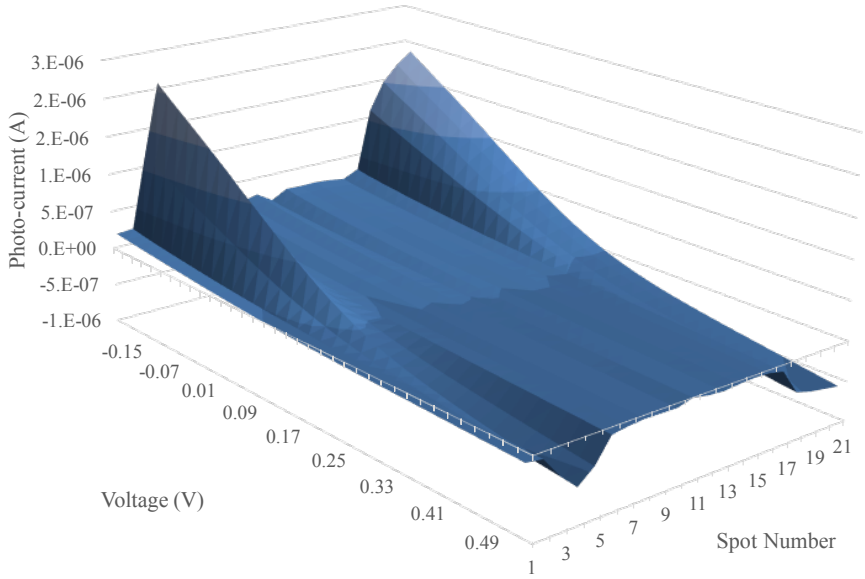

Figure 32. I-V curves of the DM(Cu)A10 sample.

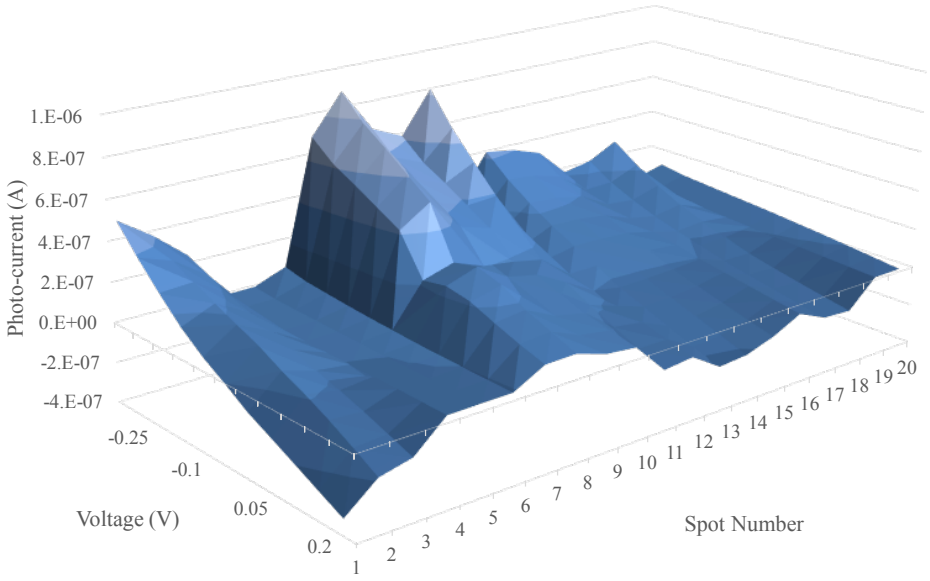

Figure 33. I-V curves of the DM(Cu,g)A1sample on aluminum stripe 1.

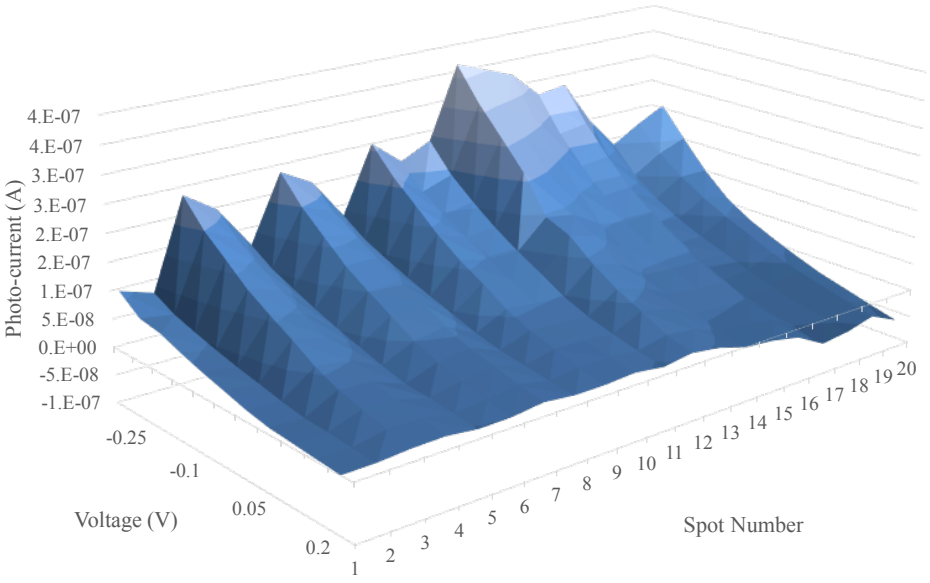

Figure 34. I-V curves of the DM(Cu,g)A1sample on aluminum stripe 2.

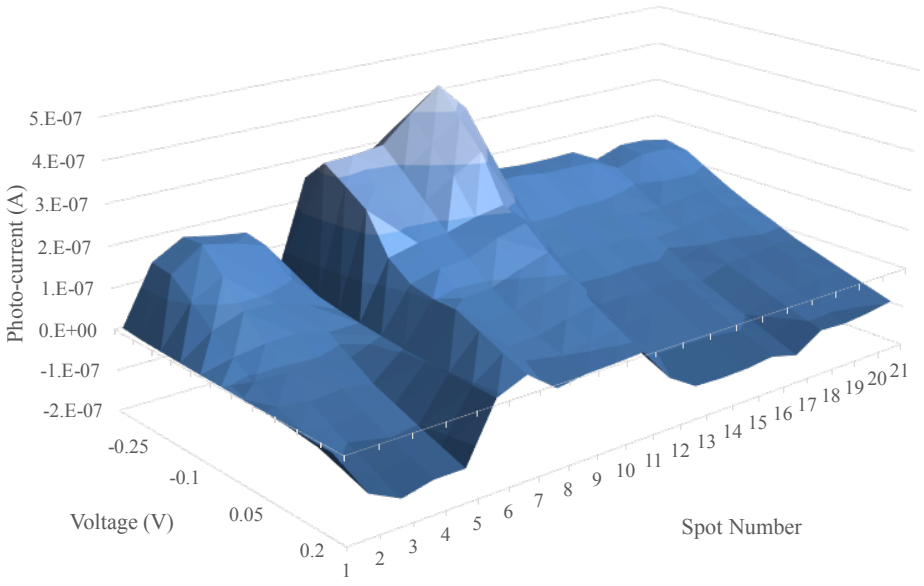

Figure 35. I-V curves of the DM(Cu,g)A3 sample on aluminum stripe 1.

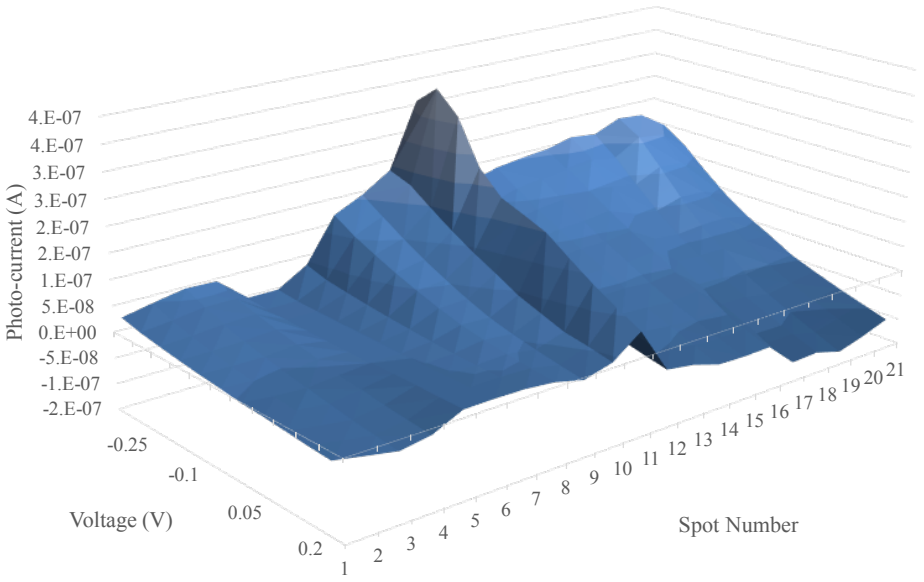

Figure 36. I-V curves of the DM(Cu,g)A3sample on aluminum stripe 2.

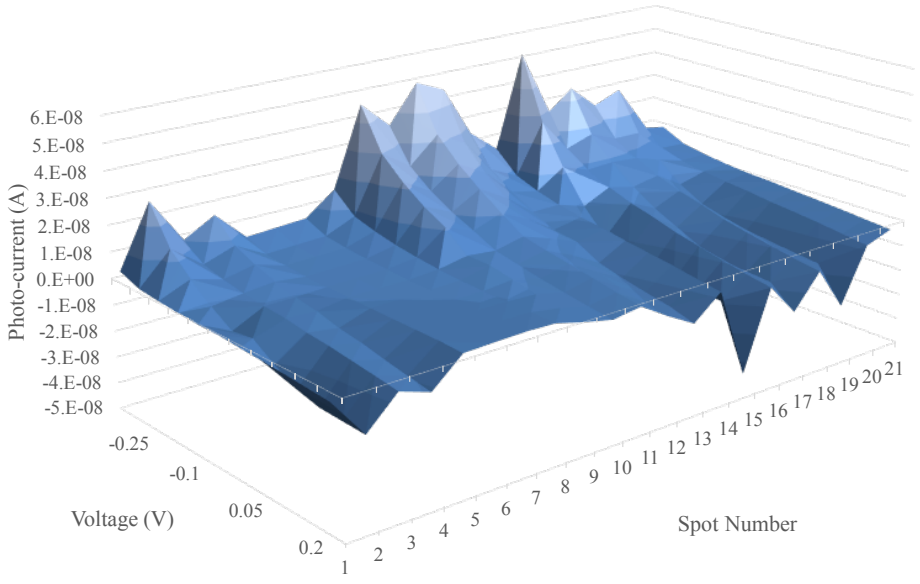

Figure 37. I-V curves of the DM(Cu,g)A4 sample on aluminum stripe 1.

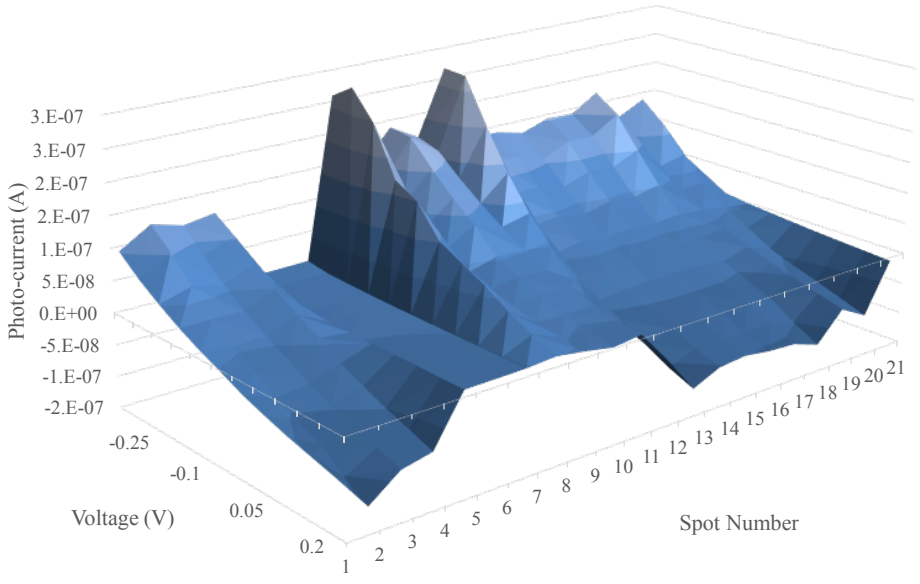

Figure 38. I-V curves of the DM(Cu,g)A4 sample on aluminum stripe 2.

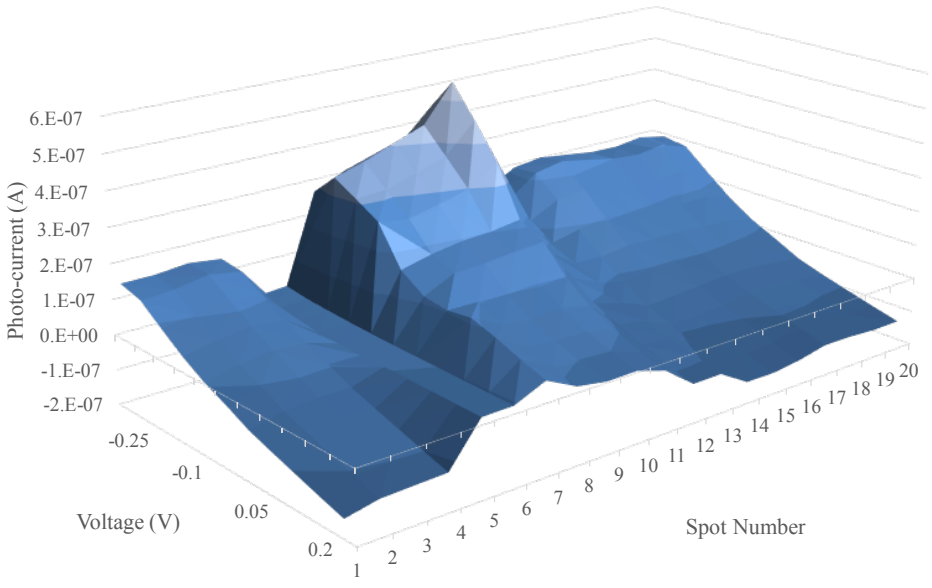

Figure 39. I-V curves of the DM(Cu,g)A4 sample on aluminum stripe 3.

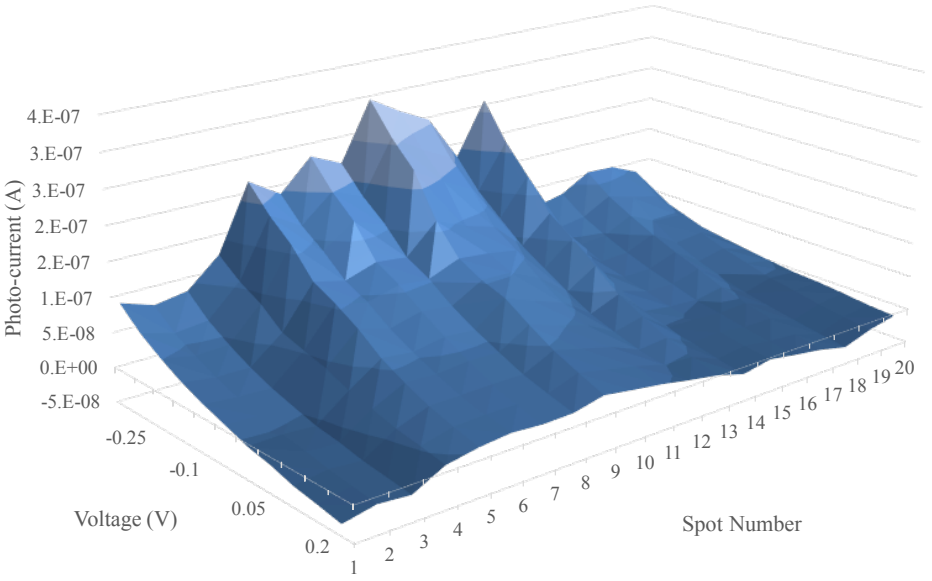

Figure 40. I-V curves of the DM(Cu,half,g)A1 sample on aluminum stripe 1.

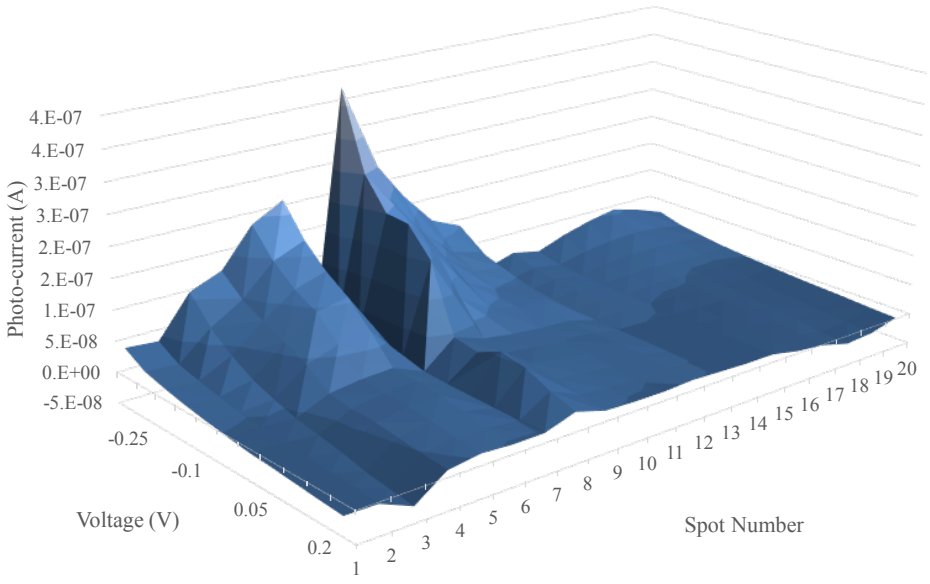

Figure 41. I-V curves of the DM(Cu,half,g)A1 sample on aluminum stripe 2.

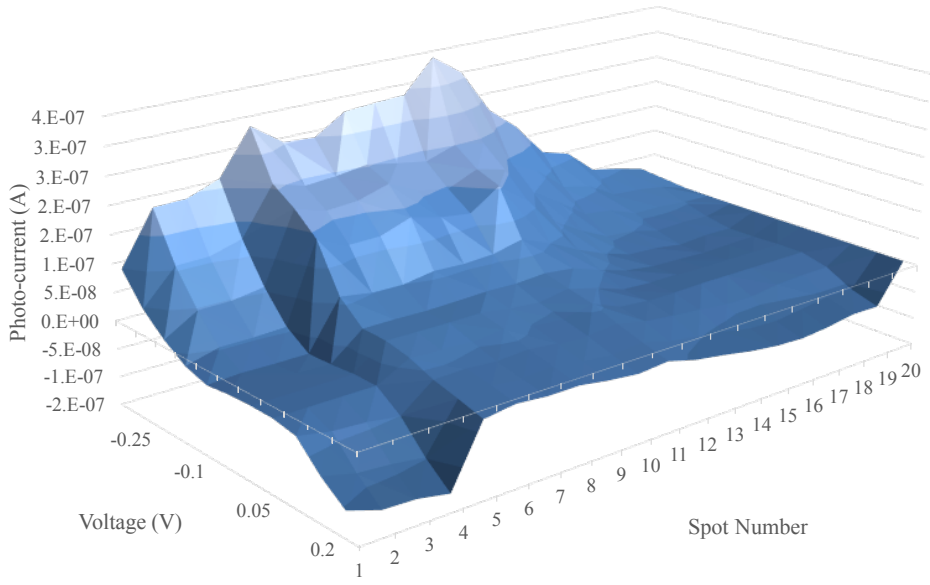

Figure 42. I-V curves of the DM(Cu,half,g)A4 sample.

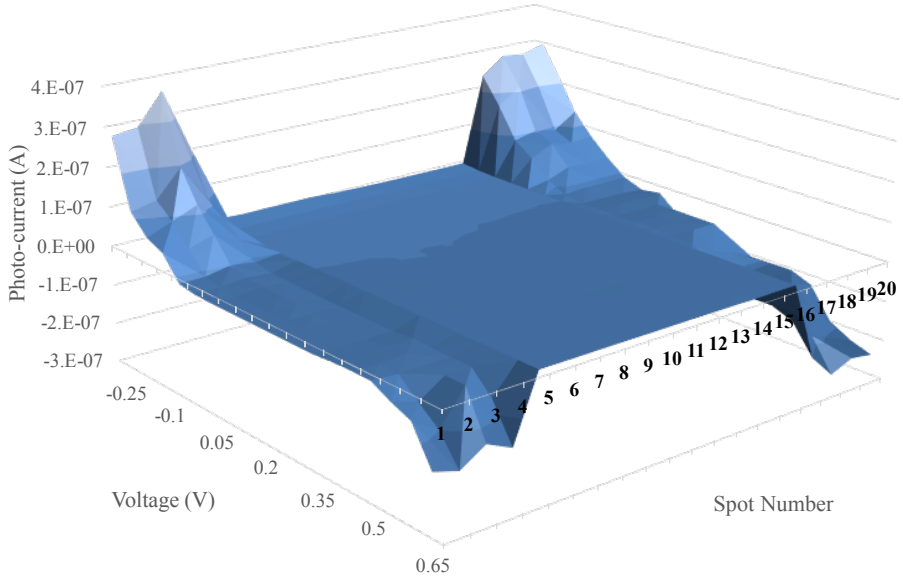

Figure 43. I-V curves of the DM(Cu4020)A1 sample on aluminum stripe 1.

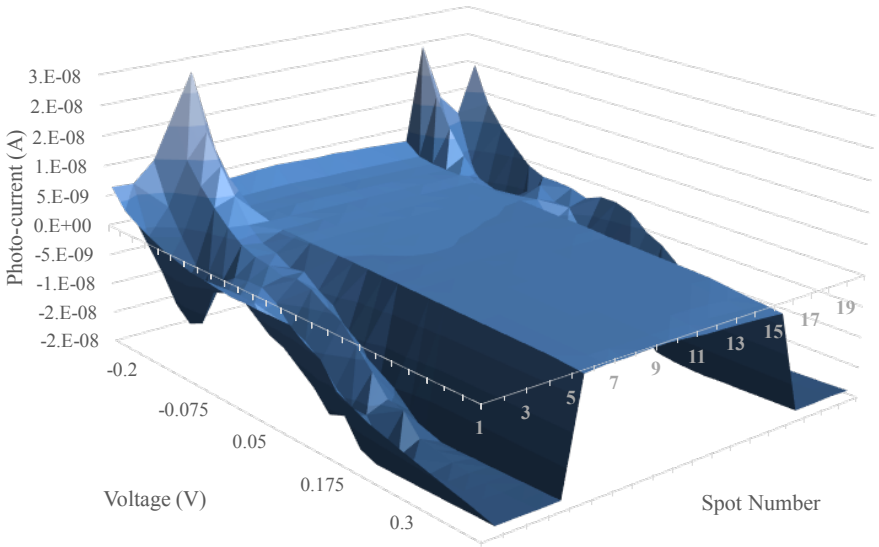

Figure 44. I-V curves of the DM(Cu4020)A1 sample on aluminum stripe 2.

Sample DM(Cu4020)A1 (Figures 43 and 44) also has a CuPc modifier layer in the form of a gradient, however this gradient does not go all the way to zero thickness. It has a maximum nominal CuPc thickness of 40 nm and a minimum of 20 nm, it is shaped like a right-angled trapezoid instead of the typical right-angled triangle. Spots 5 through 16 have the CuPc layer, where spot 5 is on the minimum thickness side of the gradient. For all these samples the I-V curves again show a change in behavior for spots with and without CuPc.

Figures 45-48 shows how the short-circuit current changed for each of these samples on different spots.

Figure 45 shows the I_{SC} for sample DM(Cu)A10. It is interesting to note that the I_{SC} seems to be more or less stable and at the same value over the spots with the modifier layer. The spots without the CuPc molecule have sharp changes in the I_{SC} and seem to change randomly.

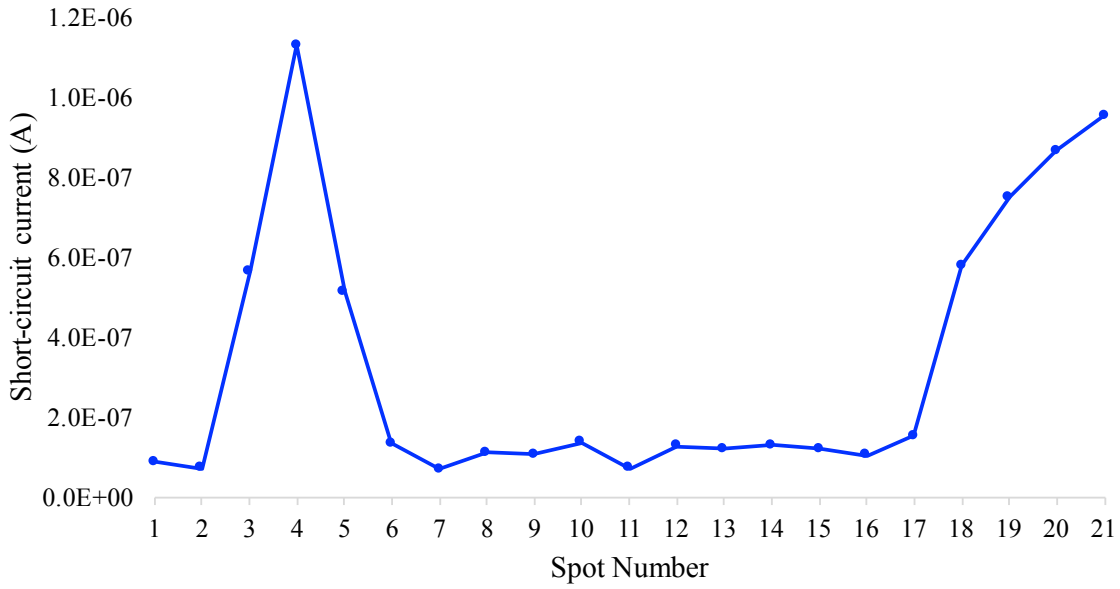

Figure 45. Short-circuit current versus spot number for sample DM(Cu)A.

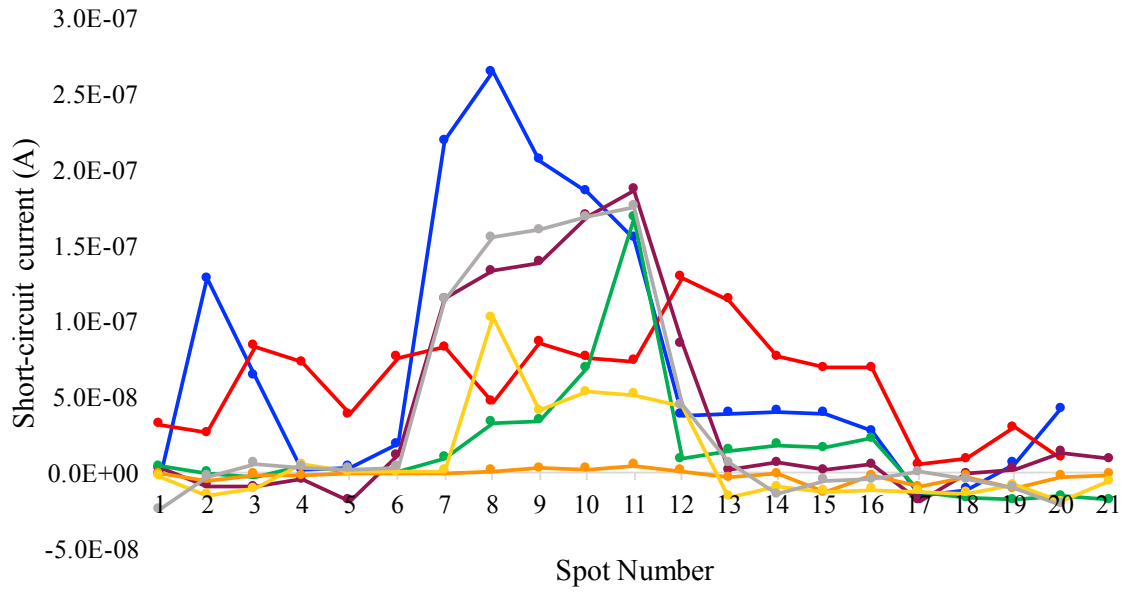

Figure 46. Short-circuit current versus spot number for samples DM(Cu,g)A1 (blue and red) for two aluminum stripes, DM(Cu,g)A3 (purple and green) for two aluminum stripes and DM(Cu,g)A4 (orange, yellow and gray) for three aluminum stripes.

Figure 47. Short-circuit current versus spot number for samples DM(Cu,half,g)A1 (blue and red) for two aluminum stripes and DM(Cu,half,g)A4 (purple).

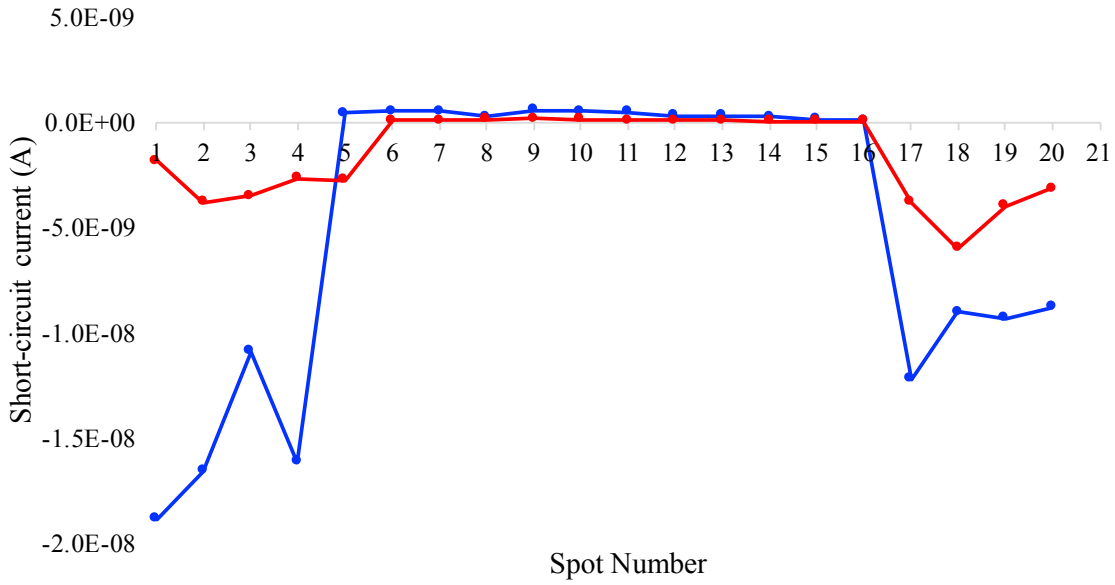

Figure 48. Short-circuit current versus spot number for samples DM(Cu4020)A1 (blue and red) for two aluminum stripes.

Figure 46 shows the set of samples that were all the same, CuPc modifier as a gradient in the middle of the substrate. The graph for sample DM(Cu,g)A1 shows that for one stripe specifically (blue graph) the I_{SC} first increases sharply and then decreases from spot 8 onward with thickness decrease. But for the other two samples, the current increases with thickness up to spot 11 and then it starts decreasing. The reason for these different electrical behaviors are not clear, however the small difference in layer thicknesses between samples might result different light absorbance and reflection for each sample which in turn causes different photon absorbance behavior and different I_{SC}.

Figure 47 shows the I_{SC} trend for the samples that had the CuPc gradient starting at spot 5 and continuing all the way to the edge of the sample. For all these samples the current increases drastically at the start of the gradient and gradually fades away. This trend is similar to some of the samples in Figure 46.

In Figure 48 the polarity of the I_{SC} changes upon the CuPc gradient and gradually decreases with increase in modifier thickness. Figures 47 and 48 combined show an interesting trend. At some thickness between 10 to 20 nm of CuPc the I_{sc} is at its maximum and at thicknesses smaller or bigger than that it starts to decrease.

3.2.4. Samples with AlPcCl as Modifier

The next set of samples has aluminum phthalocyanine chloride (AlPcCl) as the modifying molecule. All samples with this molecule had a gradient modifier layer with maximum AlPcCl nominal thickness of 30 nm. Sample DM(Al)A1 has the modifier layer from spot 5 through 16. For the other three samples, spots 6 through 17 have the AlPcCl layer. In all the samples the spot with the lowest number (5 or 6) has the maximum thickness of AlPcCl. Again, similar to the previous samples the spots with the modifier behave differently than the other spots.

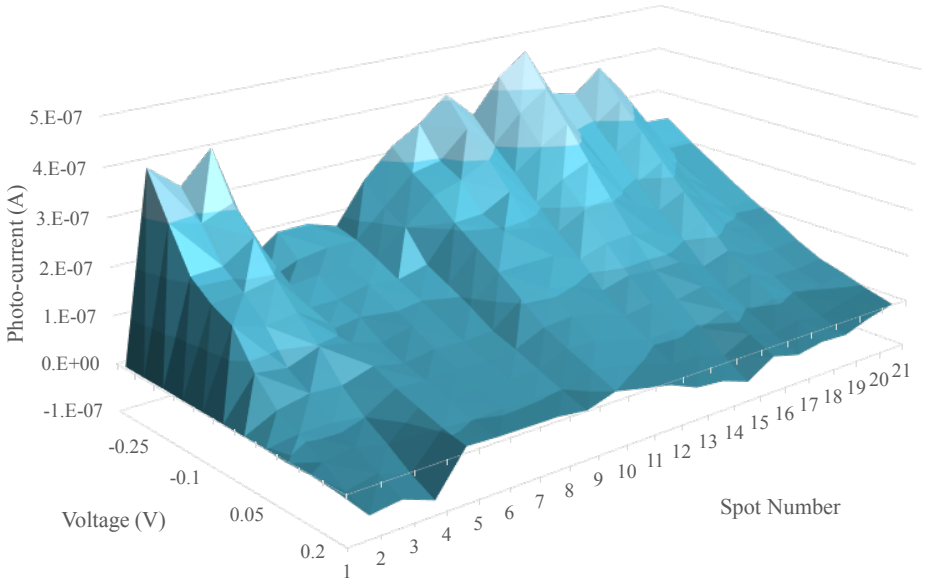

Figure 49. I-V curves of sample DM(Al)A1 for aluminum stripe 1.

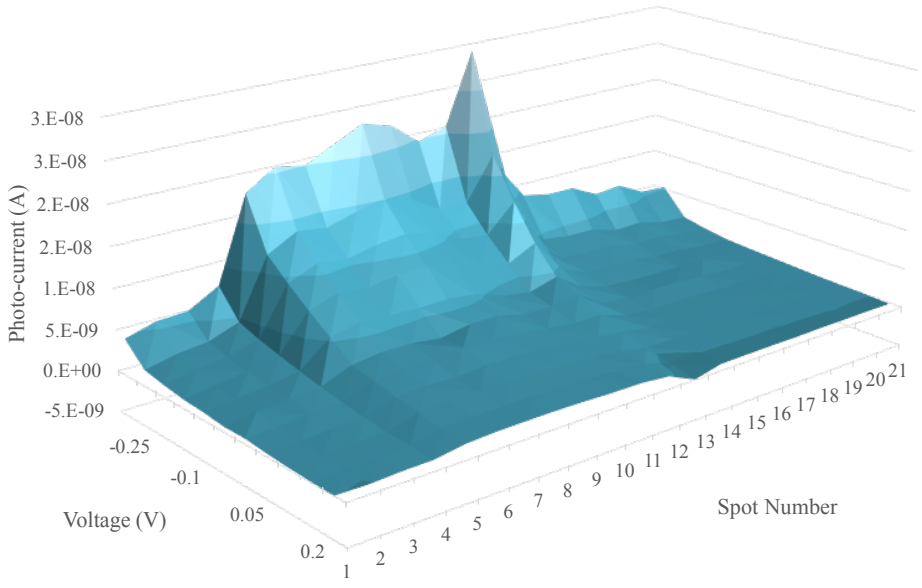

Figure 50. I-V curves of sample DM(Al)A1 for aluminum stripe 2.

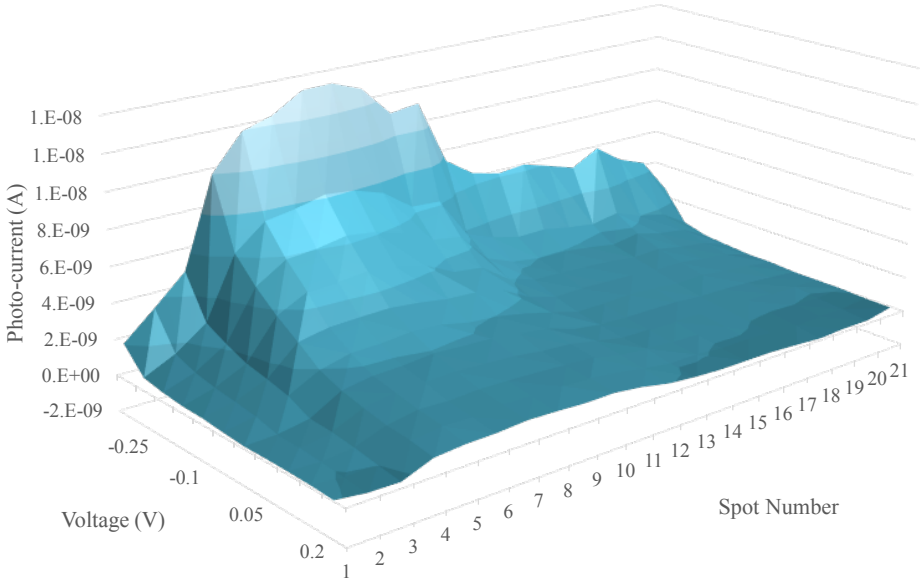

Figure 51. I-V curves of sample DM(Al)A1 for aluminum stripe 3.

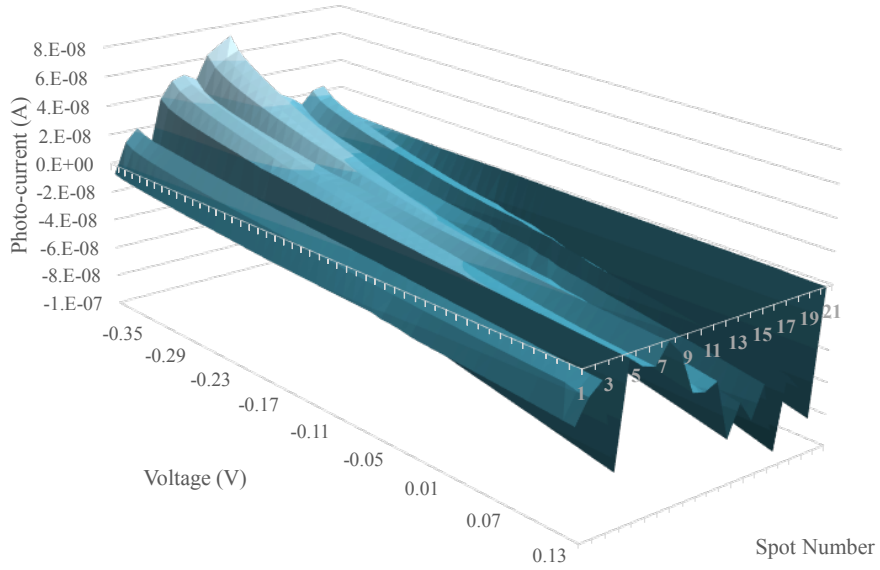

Figure 52. I-V curves of sample DM(Al)A2.

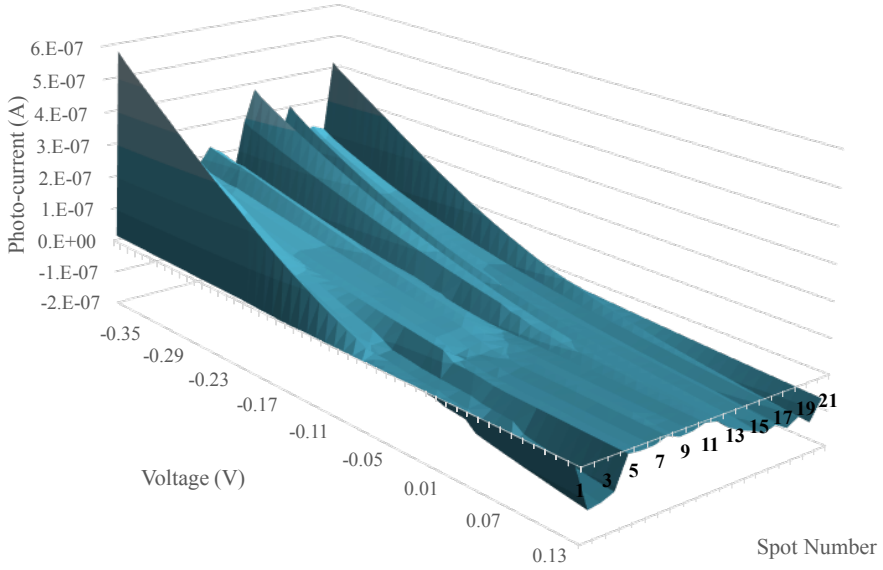

Figure 53. I-V curves of sample DM(Al)A3 for aluminum stripe 1.

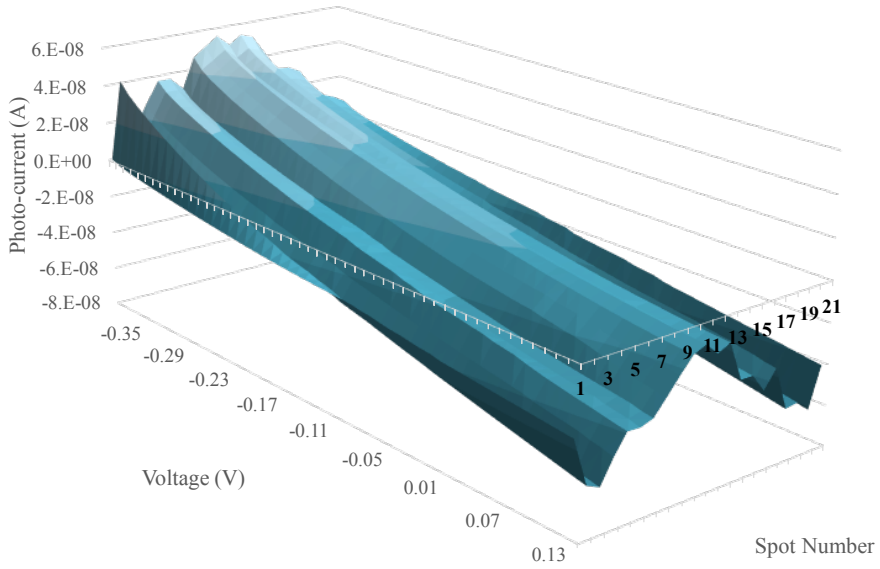

Figure 54. I-V curves of sample DM(Al)A3 for aluminum stripe 2.

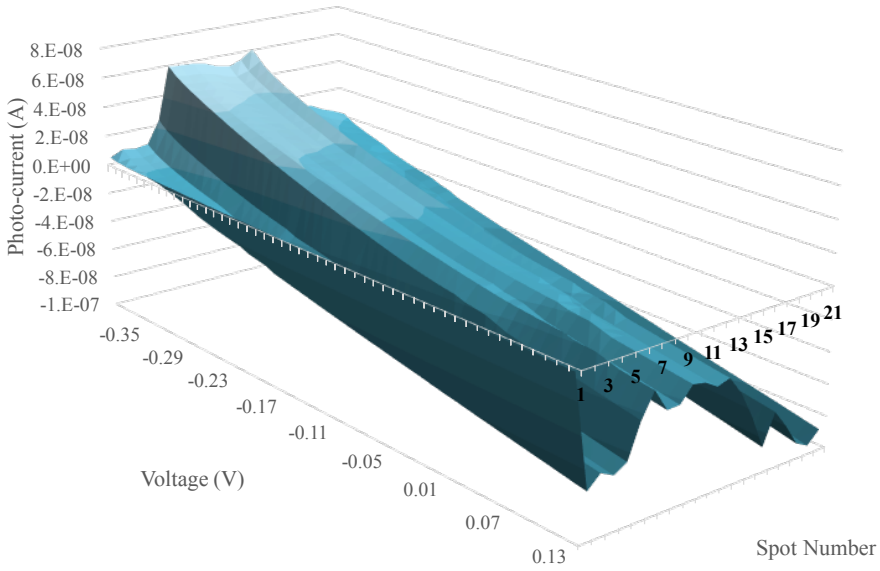

Figure 55. I-V curves of sample DM(Al)A4 for aluminum stripe 1.

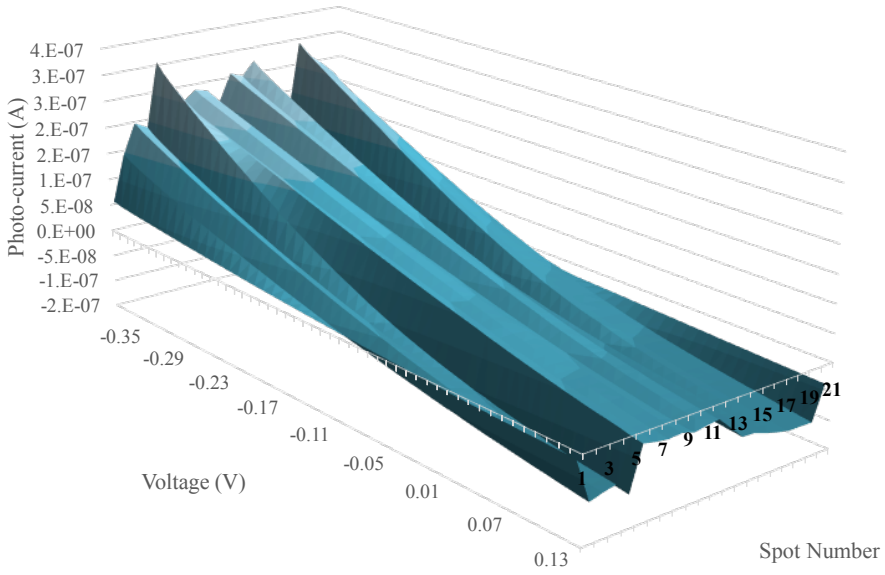

Figure 56. I-V curves of sample DM(Al)A4 for aluminum stripe 2.

Figure 57 shows how the short-circuit current changes with the spots for the different samples. For all of the samples, except DM(Al)A1, the smallest absolute value for the current can be seen at the start of the gradient and then it starts increase. For sample DM(Al)A1, one of the stripes (purple curve in Figure 58) the current has its maximum value at the maximum thickness of the gradient. For the other two stripes of this sample, Figure 58 (red curve) and Figure 57 (blue curve), it is hard to see any trend between the spots with and without the modifier layer.

On this set of samples, it is hard to get a reproducible I-V curve and find a trend between the short-circuit current and thickness of the modifier layer. The results for this modifier molecule were inconclusive since we saw different behaviors for different samples.

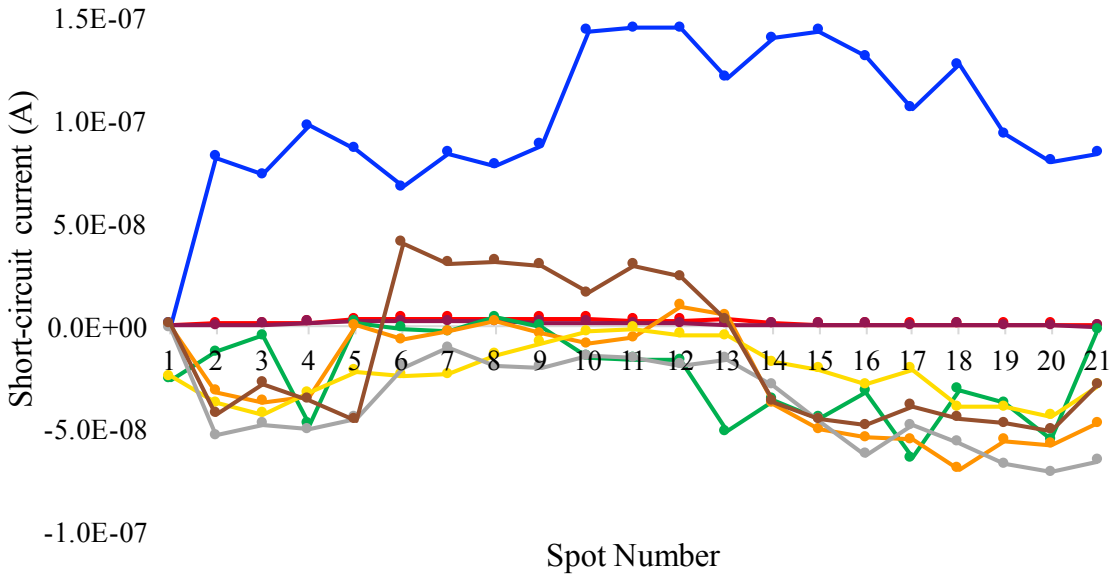

Figure 57. Short-circuit current versus spot number for samples (blue, red and purple) DM(Al)A1 for three strips, (green) DM(Al)A2, (orange and yellow) DM(Al)A3 for two stripes and (gray and brown) DM(Al)A4 for two stripes.

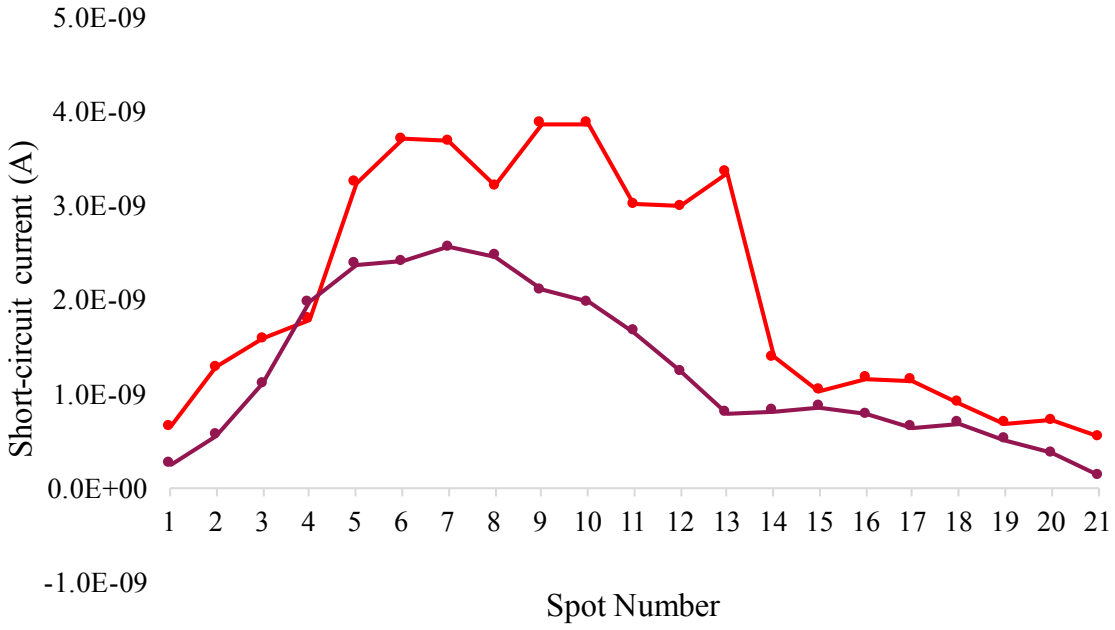

Figure 58. Zoomed in view of the red and purple curves in Figure 57.

3.2.5. Sample with 6T and CuPc as Modifier

Figure 59 shows the I-V curve of sample DM(Cu&6T)A, where there are two modifiers present on the same sample at the same time. Both modifiers were deposited as layers with the same thickness of nearly 30 nm nominal thickness of modifier. Spots 6 through 12 had the CuPc modifier and spots 14 through 20 had the 6T modifier.

Similar to what has been observed previously the spots with the modifier have a different I-V curve compared to the spots without a modifier. Figure 60 takes a closer look at the short-circuit current for different spots on this sample. The spots with the modifier layer have a smaller I_{SC} than the other spots. The spots with the CuPc modifier in general have bigger currents than the spots with the 6T molecule.

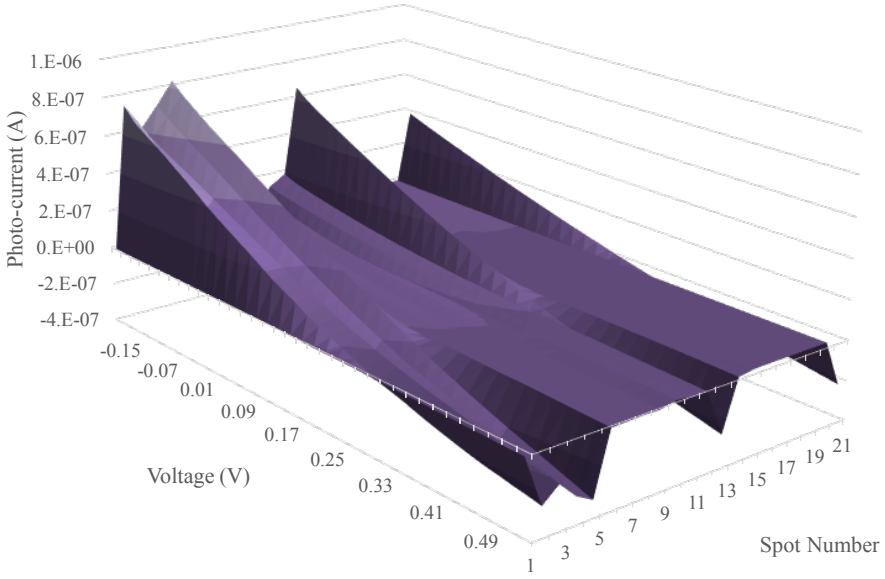

Figure 59. I-V curves for sample DM(Cu&6T)A

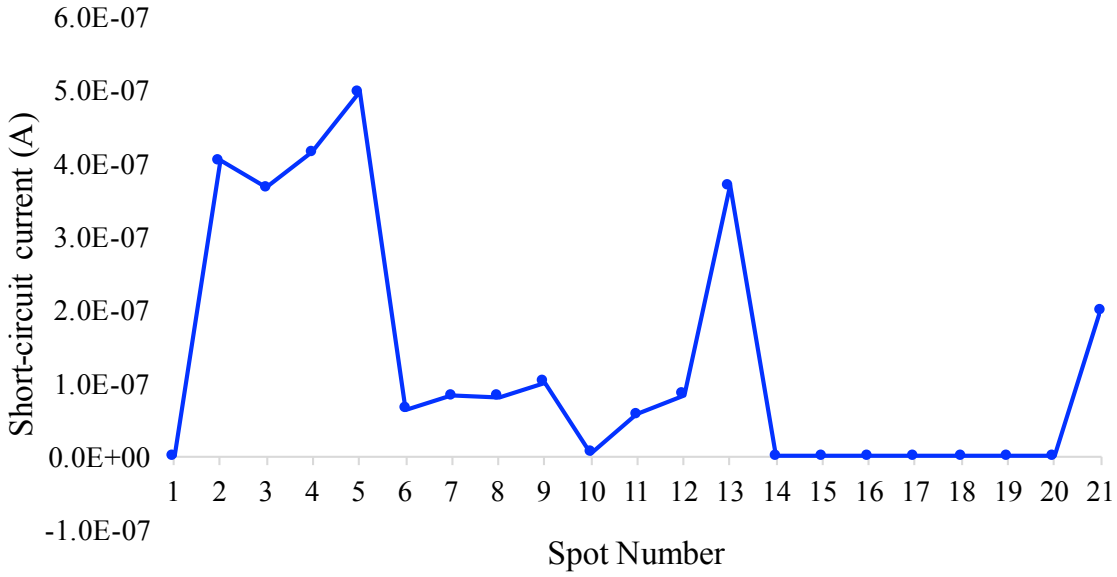

Figure 60. Short-circuit current versus spot number for sample DM(Cu&6T)A

This figure shows that with the thicknesses that were used here, the spots without the modifier layer have a bigger current and between the two modifiers CuPc seems to generate higher I_{SC}.

3.3. Bulk Heterojunction Sample

The last sample that we studied was a bulk heterojunction (BHJ) sample in which a mixture of the donor and acceptor were spin-cast onto the substrate. The donor/acceptor interface thus was intertwined through the sample and there was not one area that could be defined as the interface between the acceptor and donor phase. P3HT was used as the donor and [6,6]-Phenyl C_{61} butyric acid methyl ester (PCBM) was used as the acceptor. This sample was made as a reference; we wanted to see how the I-V curves would look on the different spots of a sample that should be the same over different spots. Also it is clear from the literature that BHJ cells are more efficient than their bilayer counterparts.[63, 198-200]

We were interested to put that into test with our fabrication procedures. Figure 61 shows the I-V curves and short-circuit current for this sample on different spots.

The first thing to note is that the I_{SC} is not as stable as was expected. The percentage of change in I_{SC} on the different spots is more or less similar to the other samples. So with

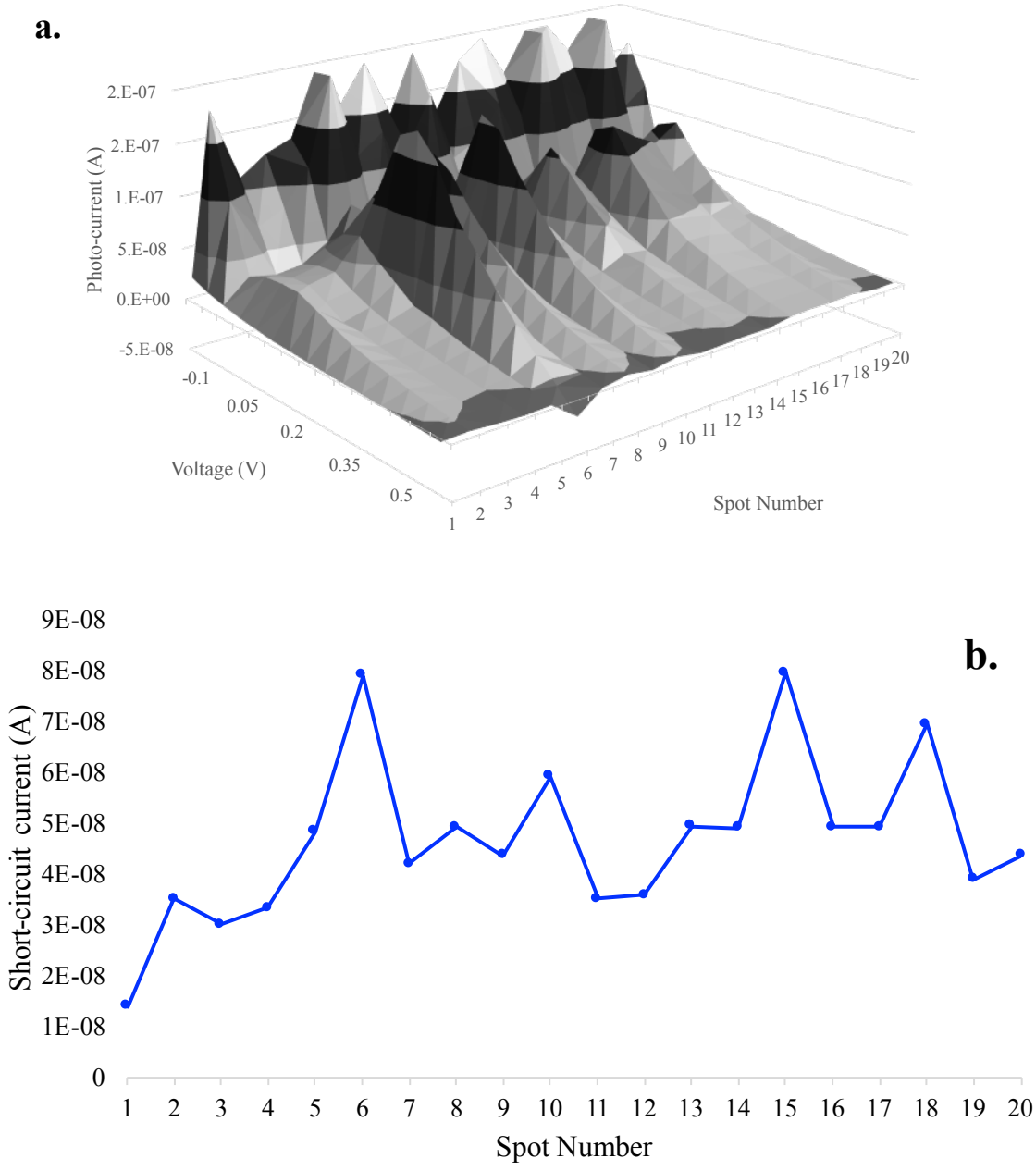

Figure 61. (a) I-V curves and (b) short-circuit current versus spot number for sample BHJ1

our fabrication scheme and measurement setup it does not seem that the spots on the BHJ sample are necessarily similar and reproducible.

Also it is worth noting that the general current of the BHJ sample is not only bigger than the other samples but it is also smaller in some cases. Again, confirming that the fabrication procedure and measurement techniques used might not be as reproducible and reliable as needed.

4. Conclusion and Future Directions

In this chapter spatially resolved electrical measurements of some organic photovoltaics were presented. Different donor, modifier, and acceptor materials were used. In some cases, the effect of the thickness of these materials was also studied. We learned that materials that can be vapor deposited generated better bilayer cells that could be reproduced more often and failed less frequently. We also observed that the presence of the modifier causes the currents to drop and make the cell less efficient. This is opposite to what one would expect, since the energy levels of some of these modifying molecules are positioned between the donor and acceptor energy levels and should have helped in the charge transition to the electrodes. We hypothesize that this could be due to the fabrication or measurement procedure, although looking through the literature it seems like our fabrication methods were similar to what is used commonly.[201-203]

The measurement setup however could have been improved. Our measurement setup made use of a green laser light source for illumination instead of the typical AM 1.5 illumination light sources. This difference in light source could cause differences in the electrical behavior, especially I_{SC}, of the samples from what is generally expected. A more

serious problem was the type of alligator clips that were used for the measurements. A thick copper wiring was used to connect the ITO and aluminum electrodes to the leads on the electrometer. Due to the movement of the stage during measurements we had to tighten the copper to the electrodes robustly. Sometimes the copper wiring would scratch into the aluminum layer, which in many occasions would cause the device to short circuit. Sanding the copper wire down and making a softer edge so it would not scratch into the aluminum helped but did not eliminate the problem completely. In the future, it is suggested to use other types of connections to the electrodes to avoid this problem. One suggestion is to solder a permanent wire to the electrodes that is more flexible than the thick copper wire and can move easier with the stage during measurements.

The ultimate goal for this project was to simultaneously do electrical measurements and VSFG spectroscopy. This type of measurement would provide valuable structure-property information that can be used to better understand the electricity generation procedure in these types of samples, and how that manifests itself in the VSFG data. Ultimately that information can be used in building more efficient organic solar cells.

References

1. Tian, C. S.; Shen, Y. R., Recent progress on sum-frequency spectroscopy. *Surface Science Reports* **2014,** *69* (2–3), 105-131.
2. Zhu, X. D.; Suhr, H.; Shen, Y. R., Surface vibrational spectroscopy by infrared-visible sum frequency generation. *Physical Review B* **1987,** *35* (6), 3047-3050.
3. Franken, P. A.; Hill, A. E.; Peters, C. W.; Weinreich, G., Generation of Optical Harmonics. *Physical Review Letters* **1961,** *7* (4), 118-119.
4. Armstrong, J. A.; Bloembergen, N.; Ducuing, J.; Pershan, P. S., Interactions between Light Waves in a Nonlinear Dielectric. *Physical Review* **1962,** *127* (6), 1918-1939.
5. Bloembergen, N.; Pershan, P. S., Light Waves at the Boundary of Nonlinear Media. *Physical Review* **1962,** *128* (2), 606-622.
6. Bloembergen, N.; Chang, R. K.; Jha, S. S.; Lee, C. H., Optical Second-Harmonic Generation in Reflection from Media with Inversion Symmetry. *Physical Review* **1968,** *174* (3), 813-822.
7. Shen, Y., Surface nonlinear optics: a historical perspective. *IEEE Journal of Selected Topics in Quantum Electronics* **2000,** *6* (6), 1375-1379.
8. Chen, J. M.; Bower, J. R.; Wang, C. S.; Lee, C. H., Optical second-harmonic generation from submonolayer Na-covered Ge surfaces. *Optics Communications* **1973,** *9* (2), 132-134.
9. Fleischmann, M.; Hendra, P. J.; McQuillan, A. J., Raman spectra of pyridine adsorbed at a silver electrode. *Chemical Physics Letters* **1974,** *26* (2), 163-166.
10. Chen, C. K.; de Castro, A. R. B.; Shen, Y. R., Surface-Enhanced Second-Harmonic Generation. *Physical Review Letters* **1981,** *46* (2), 145-148.
11. Chen, C. K.; Heinz, T. F.; Ricard, D.; Shen, Y. R., Detection of Molecular Monolayers by Optical Second-Harmonic Generation. *Physical Review Letters* **1981,** *46* (15), 1010-1012.
12. Boyd, G. T.; Hänsch, T. W.; Shen, Y. R., Continuous-wave second-harmonic generation as a surface microprobe. *Optical Letters* **1986,** *11* (2), 97-99.
13. Heinz, T. F.; Chen, C. K.; Ricard, D.; Shen, Y. R., Spectroscopy of Molecular Monolayers by Resonant Second-Harmonic Generation. *Physical Review Letters* **1982,** *48* (7), 478-481.
14. Heinz, T. F.; Loy, M. M. T.; Thompson, W. A., Study of Si(111) Surfaces by Optical Second-Harmonic Generation: Reconstruction and Surface Phase Transformation. *Physical Review Letters* **1985,** *54* (1), 63-66.
15. Tom, H. W. K.; Mate, C. M.; Zhu, X. D.; Crowell, J. E.; Heinz, T. F.; Somorjai, G. A.; Shen, Y. R., Surface Studies by Optical Second-Harmonic Generation: The Adsorption of O_2, CO, and Sodium on the Rh(111) Surface. *Physical Review Letters* **1984,** *52* (5), 348-351.
16. Tom, H. W. K.; Zhu, X. D.; Shen, Y. R.; Somorjai, G. A., Investigation of the Si(111)-(7 × 7) surface by second-harmonic generation: Oxidation and the effects of surface phosphorus. *Surface Science* **1986,** *167* (1), 167-176.

17. Zhu, X. D.; Shen, Y. R.; Carr, R., Correlation between thermal desorption spectroscopy and optical second harmonic generation for monitoring surface coverages. *Surface Science* **1985,** *163* (1), 114-120.
18. Richter, L. J.; Petralli-Mallow, T. P.; Stephenson, J. C., Vibrationally resolved sum-frequency generation with broad-bandwidth infrared pulses. *Optical Letters* **1998,** *23* (20), 1594-1596.
19. Star, D.; Kikteva, T.; Leach, G. W., Surface vibrational coherence at the CaF2/air interface: Vibrational wave packet dynamics as a probe of interface inhomogeneity. *The Journal of Chemical Physics* **1999,** *111* (1), 14-17.
20. Bain, C. D., Sum-frequency vibrational spectroscopy of the solid/liquid interface. *Journal of the Chemical Society, Faraday Transactions* **1995,** *91* (9), 1281-1296.
21. Lambert, A. G.; Davies, P. B.; Neivandt, D. J., Implementing the theory of sum frequency generation vibrational spectroscopy: A tutorial review. *Applied Spectroscopy Reviews* **2005,** *40* (2), 103-145.
22. Wang, C. C., Second-Harmonic Generation of Light at the Boundary of an Isotropic Medium. *Physical Review* **1969,** *178* (3), 1457-1460.
23. Shen, Y. R., Surfaces probed by nonlinear optics. *Surface Science* **1994,** *299*, 551-562.
24. O'Brien, D. B.; Anglin, T. C.; Massari, A. M., Surface Chemistry and Annealing-Driven Interfacial Changes in Organic Semiconducting Thin Films on Silica Surfaces. *Langmuir* **2011,** *27* (22), 13940-13949.
25. Li, G.; Dhinojwala, A.; Yeganeh, M. S., Interfacial Structure and Melting Temperature of Alcohol and Alkane Molecules in Contact with Polystyrene Films. *The Journal of Physical Chemistry B* **2009,** *113* (9), 2739-2747.
26. Harp, G. P.; Gautam, K. S.; Dhinojwala, A., Probing Polymer/Polymer Interfaces. *Journal of the American Chemical Society* **2002,** *124* (27), 7908-7909.
27. Gautam, K. S.; Schwab, A. D.; Dhinojwala, A.; Zhang, D.; Dougal, S. M.; Yeganeh, M. S., Molecular Structure of Polystyrene at Air/Polymer and Solid/Polymer Interfaces. *Physical Review Letters* **2000,** *85* (18), 3854-3857.
28. Lambert, A. G.; Neivandt, D. J.; Briggs, A. M.; Usadi, E. W.; Davies, P. B., Interference Effects in Sum Frequency Spectra from Monolayers on Composite Dielectric/Metal Substrates. *The Journal of Physical Chemistry B* **2002,** *106* (21), 5461-5469.
29. Feller, M. B.; Chen, W.; Shen, Y. R., Investigation of surface-induced alignment of liquid-crystal molecules by optical second-harmonic generation. *Physical Review A* **1991,** *43* (12), 6778-6792.
30. Hirose, C.; Ishida, H.; Iwatsu, K.; Watanabe, N.; Kubota, J.; Wada, A.; Domen, K., In situ SFG spectroscopy of film growth. I. General formulation and the analysis of the signal observed during the deposition of formic acid on Pt(110)-(1×2) surface. *The Journal of Chemical Physics* **1998,** *108* (14), 5948-5956.
31. Tong, Y.; Zhao, Y.; Li, N.; Osawa, M.; Davies, P. B.; Ye, S., Interference effects in the sum frequency generation spectra of thin organic films. I. Theoretical modeling and simulation. *The Journal of Chemical Physics* **2010,** *133* (3), 034704.
32. Lu, X.; Clarke, M. L.; Li, D.; Wang, X.; Xue, G.; Chen, Z., A Sum Frequency Generation Vibrational Study of the Interference Effect in Poly(n-butyl methacrylate)

Thin Films Sandwiched between Silica and Water. *The Journal of Physical Chemistry C* **2011,** *115* (28), 13759-13767.
33. Backus, E. H. G.; Garcia-Araez, N.; Bonn, M.; Bakker, H. J., On the Role of Fresnel Factors in Sum-Frequency Generation Spectroscopy of Metal–Water and Metal-Oxide–Water Interfaces. *The Journal of Physical Chemistry C* **2012,** *116* (44), 23351-23361.
34. Li, G.; Dhinojwala, A.; Yeganeh, M. S., Interference Effect from Buried Interfaces Investigated by Angular-Dependent Infrared−Visible Sum Frequency Generation Technique. *The Journal of Physical Chemistry C* **2011,** *115* (15), 7554-7561.
35. Sipe, J. E., New Green-function formalism for surface optics. *Journal of Optical Society of America B* **1987,** *4* (4), 481-489.
36. Yeh, P., *Optical Waves in Layered Media*. Wiley: 1988.
37. Hashizume, N.; Ohashi, M.; Kondo, T.; Ito, R., Optical harmonic generation in multilayered structures: a comprehensive analysis. *Journal of Optical Society of America B* **1995,** *12* (10), 1894-1904.
38. Wilson, P. T.; Briggman, K. A.; Wallace, W. E.; Stephenson, J. C.; Richter, L. J., Selective study of polymer/dielectric interfaces with vibrationally resonant sum frequency generation via thin-film interference. *Applied Physics Letters* **2002,** *80* (17), 3084-3086.
39. O'Brien, D. B.; Massari, A. M., Modeling multilayer thin film interference effects in interface-specific coherent nonlinear optical spectroscopies. *Journal of Optical Society of America B* **2013,** *30* (6), 1503-1512.
40. O'Brien, D. B.; Massari, A. M., Simulated vibrational sum frequency generation from a multilayer thin film system with two active interfaces. *The Journal of Chemical Physics* **2013,** *138* (15), 154708.
41. O'Brien, D. B.; Massari, A. M., Experimental evidence for an optical interference model for vibrational sum frequency generation on multilayer organic thin film systems. I. Electric dipole approximation. *The Journal of Chemical Physics* **2015,** *142* (2), 024703.
42. O'Brien, D. B.; Massari, A. M., Experimental evidence for an optical interference model for vibrational sum frequency generation on multilayer organic thin film systems. II. Consideration for higher order terms. *The Journal of Chemical Physics* **2015,** *142* (2), 024704.
43. Becquerel, A. E., Recherches sur les effets de la radiation chimique de la lumiere solaire au moyen des courants electriques. *Comptes Rendus de l'Académie des Sciences* **1839,** *9*, 145-149.
44. Smith, W., Effect of Light on Selenium During the Passage of An Electric Current. *Nature* **1873,** *7* (173), 303.
45. W.G. Adams, R. E. D., The Action of Light on Selenium. *Proceedings of the Royal Society of London* **1876,** *25*, 113-117.
46. Chapin, D. M.; Fuller, C. S.; Pearson, G. L., A New Silicon p-n Junction Photocell for Converting Solar Radiation into Electrical Power. *Journal of Applied Physics* **1954,** *25* (5), 676-677.
47. Spanggaard, H.; Krebs, F. C., A brief history of the development of organic and polymeric photovoltaics. *Solar Energy Materials and Solar Cells* **2004,** *83* (2–3), 125-146.

48. Pochettino, A., Sul comportamento foto-elettrico dell'antracene. *Academia dei Lincei Rendiconti* **1906,** *15*, 355.
49. Volmer, M., Different Photoelectric Phenomena in Anthracene, their Relation to one another, to Fluorescence and to the Formation of Dianthracene. *Annalen der Physik* **1913,** *40*, 775-96.
50. Carswell, D.; Ferguson, J.; Lyons, L., Photo-and Semi-conductance in Molecular Single Crystals. *Nature* **1954,** *173*, 736.
51. Geacintov, N.; Pope, M.; Kallmann, H., Photogeneration of charge carriers in tetracene. *The Journal of chemical physics* **1966,** *45* (7), 2639-2649.
52. Weigl, J. W., Spectroscopic Properties of Organic Photoconductors. I. Absorption Spectra of Cationic Dye Films. *The Journal of Chemical Physics* **1956,** *24* (2), 364-370.
53. Oueriagli, A.; Kassi, H.; Hotchandani, S.; Leblanc, R., Analysis of dark current-voltage characteristics of Al/chlorophyll a/Ag sandwich cells. *Journal of Applied Physics* **1992,** *71* (11), 5523-5530.
54. Aydin, M.; Yakuphanoglu, F.; Kılıçoğlu, T., The current–voltage and capacitance–voltage characteristics of molecularly modified β-carotene/n-type Si junction structure with fluorescein sodium salt. *Synthetic Metals* **2007,** *157* (24), 1080-1084.
55. Cowie, J., Conductive polymers and plastics: JM Margolis (ed.) Chapman and Hall, London, 1989.
56. Skotheim, T. A., *Handbook of Conducting Polymers*. Taylor & Francis Group: New York, 1986; Vol. 1 & 2.
57. Weinberger, B.; Akhtar, M.; Gau, S., Polyacetylene photovoltaic devices. *Synthetic Metals* **1982,** *4* (3), 187-197.
58. Tang, C. W., 2-layer Organic Photovoltaic Cell. *Applied Physics Letters* **1986,** *48* (2), 183-185.
59. Hiramoto, M.; Fujiwara, H.; Yokoyama, M., Three-layered organic solar cell with a photoactive interlayer of codeposited pigments. *Applied Physics Letters* **1991,** *58* (10), 1062-1064.
60. Sariciftci, N.; Braun, D.; Zhang, C.; Srdanov, V.; Heeger, A.; Stucky, G.; Wudl, F., Semiconducting polymer-buckminsterfullerene heterojunctions: Diodes, photodiodes, and photovoltaic cells. *Applied Physics Letters* **1993,** *62* (6), 585-587.
61. Yu, G.; Zhang, C.; Heeger, A., Dual-function semiconducting polymer devices: Light-emitting and photodetecting diodes. *Applied Physics Letters* **1994,** *64* (12), 1540-1542.
62. Yu, G.; Heeger, A. J., Charge Separation and Photovoltaic Conversion in Polymer Composites with Internal Donor-Acceptor Heterojunctions. *Journal of Applied Physics* **1995,** *78* (7), 4510-4515.
63. Halls, J. J. M.; Walsh, C. A.; Greenham, N. C.; Marseglia, E. A.; Friend, R. H.; Moratti, S. C.; Holmes, A. B., Efficient photodiodes from interpenetrating polymer networks. *Nature* **1995,** *376* (6540), 498-500.
64. Tvingstedt, K.; Inganäs, O., Electrode Grids for ITO Free Organic Photovoltaic Devices. *Advanced Materials* **2007,** *19* (19), 2893-2897.
65. Kippelen, B., Organic Photovoltaics. *Optics and Photonics News* **2007,** *18* (10), 26-33.

66. Blom, P. W.; Mihailetchi, V. D.; Koster, L. J. A.; Markov, D. E., Device physics of polymer: fullerene bulk heterojunction solar cells. *Advanced Materials* **2007,** *19* (12), 1551-1566.
67. Faissler, W. L., *An Introduction to Modern Electronics*. John Wiley & Sons, Inc.: New York, 1991.
68. Seanor, D. A., *Electrical Properties of Polymers*. Academic Press: New York, 1982.
69. Peumans, P.; Yakimov, A.; Forrest, S. R., Small molecular weight organic thin-film photodetectors and solar cells. *Journal of Applied Physics* **2003,** *93* (7), 3693-3723.
70. Clarke, T. M.; Durrant, J. R., Charge Photogeneration in Organic Solar Cells. *Chemical Reviews* **2010,** *110* (11), 6736-6767.
71. Liu, J.; Chen, S.; Qian, D.; Gautam, B.; Yang, G.; Zhao, J.; Bergqvist, J.; Zhang, F.; Ma, W.; Ade, H.; Inganäs, O.; Gundogdu, K.; Gao, F.; Yan, H., Fast charge separation in a non-fullerene organic solar cell with a small driving force. *Nature Energy* **2016,** *1*, 16089.
72. Green, M. A.; Emery, K.; Hishikawa, Y.; Warta, W.; Dunlop, E. D., Solar cell efficiency tables (version 47). *Progress in Photovoltaics: Research and Applications* **2016,** *24* (1), 3-11.
73. Günes, S.; Neugebauer, H.; Sariciftci, N. S., Conjugated polymer-based organic solar cells. *Chemical Reviews* **2007,** *107* (4), 1324-1338.
74. Brumbach, M.; Placencia, D.; Armstrong, N. R., Titanyl phthalocyanine/C60 heterojunctions: Band-edge offsets and photovoltaic device performance. *The Journal of Physical Chemistry C* **2008,** *112* (8), 3142-3151.
75. Zhu, X.; Kahn, A., Electronic structure and dynamics at organic donor/acceptor interfaces. *MRS bulletin* **2010,** *35* (06), 443-448.
76. W., M., *Electronic Properties of Semiconductor Interfaces*. Springer-Verlag: Berlin, 2004.
77. Vázquez, H.; Gao, W.; Flores, F.; Kahn, A., Energy level alignment at organic heterojunctions: Role of the charge neutrality level. *Physical Review B* **2005,** *71* (4), 041306.
78. Shen, Y. R., *The Principles of Nonlinear Optics*. John Wiley and Sons, Inc.: 1984.
79. Aliaga, C.; Santos, C. S.; Baldelli, S., Surface chemistry of room-temperature ionic liquids. *Physical Chemistry Chemical Physics* **2007,** *9* (28), 3683-3700.
80. Brindza, M. R.; Walker, R. A., Differentiating Solvation Mechanisms at Polar Solid/Liquid Interfaces. *Journal of the American Chemical Society* **2009,** *131* (17), 6207-6214.
81. Gopalakrishnan, S.; Liu, D. F.; Allen, H. C.; Kuo, M.; Shultz, M. J., Vibrational spectroscopic studies of aqueous interfaces: Salts, acids, bases, and nanodrops. *Chemical Reviews* **2006,** *106* (4), 1155-1175.
82. Jena, K. C.; Hore, D. K., Variation of Ionic Strength Reveals the Interfacial Water Structure at a Charged Mineral Surface. *Journal of Physical Chemistry C* **2009,** *113* (34), 15364-15372.
83. Lu, G. Q.; Lagutchev, A.; Dlott, D. D.; Wieckowski, A., Quantitative vibrational sum-frequency generation spectroscopy of thin layer electrochemistry: CO on a Pt electrode. *Surface Science* **2005,** *585* (1-2), 3-16.

84. Nihonyanagi, S.; Ishiyama, T.; Lee, T.; Yamaguchi, S.; Bonn, M.; Morita, A.; Tahara, T., Unified Molecular View of the Air/Water Interface Based on Experimental and Theoretical chi((2)) Spectra of an Isotopically Diluted Water Surface. *Journal of the American Chemical Society* **2011,** *133* (42), 16875-16880.
85. Roke, S.; Kleyn, A. W.; Bonn, M., Femtosecond sum frequency generation at the metal-liquid interface. *Surface Science* **2005,** *593* (1-3), 79-88.
86. Stiopkin, I. V.; Weeraman, C.; Pieniazek, P. A.; Shalhout, F. Y.; Skinner, J. L.; Benderskii, A. V., Hydrogen bonding at the water surface revealed by isotopic dilution spectroscopy. *Nature* **2011,** *474* (7350), 192-195.
87. Wang, H. F.; Gan, W.; Lu, R.; Rao, Y.; Wu, B. H., Quantitative spectral and orientational analysis in surface sum frequency generation vibrational spectroscopy (SFG-VS). *International Reviews in Physical Chemistry* **2005,** *24* (2), 191-256.
88. Hommel, E. L.; Allen, H. C., The air-liquid interface of benzene, toluene, m-xylene, and mesitylene: a sum frequency, Raman, and infrared spectroscopic study. *Analyst* **2003,** *128* (6), 750-755.
89. Kawaguchi, T.; Shiratori, K.; Henmi, Y.; Ishiyama, T.; Morita, A., Mechanisms of Sum Frequency Generation from Liquid Benzene: Symmetry Breaking at Interface and Bulk Contribution. *Journal of Physical Chemistry C* **2012,** *116* (24), 13169-13182.
90. Peremans, A.; Caudano, Y.; Thiry, P. A.; Dumas, P.; Zhang, W. Q.; LeRille, A.; Tadjeddine, A., Electronic tuning of dynamical charge transfer at an interface: K doping of C-60/Ag(111). *Physical Review Letters* **1997,** *78* (15), 2999-3002.
91. Silien, C.; Caudano, Y.; Longueville, J. L.; Bouzidi, S.; Wiame, F.; Peremans, A.; Thiry, P. A., HREELS, IR and SFG investigation of undoped and doped adsorbed fullerenes. *Surface Science* **1999,** *427-28*, 79-84.
92. Caudano, Y.; Peremans, A.; Thiry, P. A.; Dumas, P.; Tadjeddine, A., Vibrational investigation of chemisorbed C-60 by infrared-visible sum frequency generation spectroscopy. *Surface Science* **1997,** *377* (1-3), 1071-1075.
93. Humbert, C.; Caudano, Y.; Dreesen, L.; Sartenaer, Y.; Mani, A. A.; Silien, C.; Lemaire, J. J.; Thiry, P. A.; Peremans, A., Self-assembled organic and fullerene monolayers characterisation by two-colour SFG spectroscopy: a pathway to meet doubly resonant SFG process. *Applied Surface Science* **2004,** *237* (1-4), 462-468.
94. Wei, Q. S.; Tajima, K.; Tong, Y. J.; Ye, S.; Hashimoto, K., Surface-Segregated Monolayers: A New Type of Ordered Monolayer for Surface Modification of Organic Semiconductors. *Journal of the American Chemical Society* **2009,** *131* (48), 17597-17604.
95. Rumpel, A.; Novak, M.; Walter, J.; Braunschweig, B.; Halik, M.; Peukert, W., Tuning the Molecular Order of C-60 Functionalized Phosphonic Acid Monolayers. *Langmuir* **2011,** *27* (24), 15016-15023.
96. Kern, W., *Handbook of Semiconductor Wafer Cleaning Technology: Science, Technology, and Applications Material Science and Process Technology Series*. Noyes Publications: Park Ridge, NJ, 1993.
97. O'Brien, D. B.; Anglin, T. C.; Massari, A. M., Surface Chemistry and Annealing-Driven Interfacial Changes in Organic Semiconducting Thin Films on Silica Surfaces. *Langmuir* **2011,** *27* (22), 13940-13949.
98. Reinhardt, K. A. K., W. Eds., *Handbook of Silicon Wafer Cleaning Technology*. 2nd ed.; William Andrew: Norwich, 2008.

99. Anttila, O. J.; Tilli, M. V., Metal Contamination Removal on Silicon-wafers Using Dilute Acidic Solutions. *Journal of the Electrochemical Society* **1992,** *139* (6), 1751-1756.
100. Frisch, M. J.; Trucks, G. W.; Schlegel, H. B.; Scuseria, G. E.; Robb, M. A.; Cheeseman, J. R.; Scalmani, G.; Barone, V.; Mennucci, B.; Petersson, G. A.; Nakatsuji, H.; Caricato, M.; Li, X.; Hratchian, H. P.; Izmaylov, A. F.; Bloino, J.; Zheng, G.; Sonnenberg, J. L.; Hada, M.; Ehara, M.; Toyota, K.; Fukuda, R.; Hasegawa, J.; Ishida, M.; Nakajima, T.; Honda, Y.; Kitao, O.; Nakai, H.; Vreven, T.; Montgomery Jr., J. A.; Peralta, J. E.; Ogliaro, F.; Bearpark, M. J.; Heyd, J.; Brothers, E. N.; Kudin, K. N.; Staroverov, V. N.; Kobayashi, R.; Normand, J.; Raghavachari, K.; Rendell, A. P.; Burant, J. C.; Iyengar, S. S.; Tomasi, J.; Cossi, M.; Rega, N.; Millam, N. J.; Klene, M.; Knox, J. E.; Cross, J. B.; Bakken, V.; Adamo, C.; Jaramillo, J.; Gomperts, R.; Stratmann, R. E.; Yazyev, O.; Austin, A. J.; Cammi, R.; Pomelli, C.; Ochterski, J. W.; Martin, R. L.; Morokuma, K.; Zakrzewski, V. G.; Voth, G. A.; Salvador, P.; Dannenberg, J. J.; Dapprich, S.; Daniels, A. D.; Farkas, Ö.; Foresman, J. B.; Ortiz, J. V.; Cioslowski, J.; Fox, D. J. *Gaussian 09 Revision D.01*, Gaussian, Inc.: Wallingford, CT, USA, 2009.
101. Schettino, V.; Pagliai, M.; Cardini, G., The infrared and Raman spectra of fullerene C-70. DFT calculations and correlation with C-60. *Journal of Physical Chemistry A* **2002,** *106* (9), 1815-1823.
102. Schettino, V.; Pagliai, M.; Ciabini, L.; Cardini, G., The vibrational spectrum of fullerene C-60. *Journal of Physical Chemistry A* **2001,** *105* (50), 11192-11196.
103. Zhuang, X.; Miranda, P. B.; Kim, D.; Shen, Y. R., Mapping molecular orientation and conformation at interfaces by surface nonlinear optics. *Physical Review B* **1999,** *59* (19), 12632-12640.
104. Moad, A. J.; Simpson, G. J., A unified treatment of selection rules and symmetry relations for sum-frequency and second harmonic spectroscopies. *Journal of Physical Chemistry B* **2004,** *108* (11), 3548-3562.
105. Chase, B.; Herron, N.; Holler, E., Vibrational Spectroscopy of C_{60} and C_{70} Temperature-dependent Studies. *Journal of Physical Chemistry* **1992,** *96* (11), 4262-4266.
106. Kuzmany, H.; Pichler, T.; Winkler, R., Equilibrium Phases in Alkali-metal Doped C_{60} Films and Single-crystals from In-situ IR-reflectivity. *Synthetic Metals* **1995,** *70* (1-3), 1329-1332.
107. Bethune, D. S.; Meijer, G.; Tang, W. C.; Rosen, H. J.; Golden, W. G.; Seki, H.; Brown, C. A.; Devries, M. S., Vibrational Raman and Infrared-spectra of Chromatographically Separated C_{60} and C_{70} Fullerene Clusters. *Chemical Physics Letters* **1991,** *179* (1-2), 181-186.
108. Bethune, D. S.; Meijer, G.; Tang, W. C.; Rosen, H. J., The Vibrational Raman Spectra of Purified Solid Films of C_{60} and C_{70}. *Chemical Physics Letters* **1990,** *174* (3-4), 219-222.
109. Dresselhaus, M. S.; Dresselhaus, G.; Eklund, P. C., Fullerenes. *Journal of Materials Research* **1993,** *8* (8), 2054-2097.
110. Winkler, R.; Pichler, T.; Kuzmany, H., Vibrational Analysis of IR Reflection-transmission from Songle-crystal C_{60}. *Zeitschrift Fur Physik B-Condensed Matter* **1994,** *96* (1), 39-45.

111. Merrick, J. P.; Moran, D.; Radom, L., An evaluation of harmonic vibrational frequency scale factors. *Journal of Physical Chemistry A* **2007,** *111* (45), 11683-11700.
112. Wang, X. Q.; Wang, C. Z.; Ho, K. M., 1st-principles Study of Vibrational-modes in Icosahedral C_{60}. *Physical Review B* **1993,** *48* (3), 1884-1887.
113. Liu, Y. L.; Jiang, Y. J.; Liu, J. Q.; Mo, Y. J.; Xie, S. S.; Zhang, Z. B.; Quan, S. F., Fundamental and Higher-order Raman Spectra of C_{60} Films. *Physical Review B* **1994,** *49* (7), 5058-5061.
114. Akers, K. L.; Douketis, C.; Haslett, T. L.; Moskovits, M., Raman Spectroscopy of C_{60} Solid Films - A Tale of 2 Spectra. *Journal of Physical Chemistry* **1994,** *98* (42), 10824-10831.
115. Matus, M.; Kuzmany, H., Raman Spectra of Single-crystal C_{60}. *Applied Physics a-Materials Science & Processing* **1993,** *56* (3), 241-248.
116. Rao, A. M.; Zhou, P.; Wang, K. A.; Hager, G. T.; Holden, J. M.; Wang, Y.; Lee, W. T.; Bi, X. X.; Eklund, P. C.; Cornett, D. S.; Duncan, M. A.; Amster, I. J., Photoinduced Polymerization of Solid C_{60} Films. *Science* **1993,** *259* (5097), 955-957.
117. O'Brien, D. B.; Massari, A. M., Simulated vibrational sum frequency generation from a multilayer thin film system with two active interfaces. *Journal of Chemical Physics* **2013,** *138* (15), 154708.
118. O'Brien, D. B.; Massari, A. M., Modeling multilayer thin film interference effects in interface-specific coherent nonlinear optical spectroscopies. *Journal of the Optical Society of America B-Optical Physics* **2013,** *30* (6), 1503-1512.
119. O'Brien, D. B.; Massari, A. M., Experimental evidence for an optical interference model for vibrational sum frequency generation on multilayer organic thin film systems. I. Electric dipole approximation. *Journal of Chemical Physics* **2015,** *142* (2), 024703.
120. O'Brien, D. B.; Massari, A. M., Experimental evidence for an optical interference model for vibrational sum frequency generation on multilayer organic thin film systems. II. Consideration for higher order terms. *Journal of Chemical Physics* **2015,** *142* (2), 024704.
121. Kitamura, R.; Pilon, L.; Jonasz, M., Optical constants of silica glass from extreme ultraviolet to far infrared at near room temperature. *Applied Optics* **2007,** *46* (33), 8118-8133.
122. Palik, E. D., *Handbook of optical constants of solids*. Academic Press: San Diego, 1998; Vol. 1&2.
123. Richter, A.; Sturm, J., Dielectric and Optical Properties of C_{60} Material Studied by Ellipsometry and Quantitative IR and UV/Vis Spectroscopy. *Applied Physics a-Materials Science & Processing* **1995,** *61* (2), 163-170.
124. Toll, J. S., Causality and the Dispersion Relation: Logical Foundations. *Physical Review* **1956,** *104* (6), 1760-1770.
125. Duclos, S. J.; Haddon, R. C.; Glarum, S.; Hebard, A. F.; Lyons, K. B., Raman Studies of Alakli-metal Doped AXC_{60} Films (A = Na, K, Rb, and Cs, X = 0, 3 and 6). *Science* **1991,** *254* (5038), 1625-1627.
126. Wang, K. A.; Wang, Y.; Zhou, P.; Holden, J. M.; Ren, S. L.; Hager, G. T.; Ni, H. F.; Eklund, P. C.; Dresselhaus, G.; Dresselhaus, M. S., Raman-acattering in C_{60} and Alakli metal-doped C_{60} Films. *Physical Review B* **1992,** *45* (4), 1955-1958.
127. Giannozzi, P.; Andreoni, W., Effects of doping on the vibrational properties of C-60 from first principles: K6C60. *Physical Review Letters* **1996,** *76* (26), 4915-4918.

128. Kohanoff, J.; Andreoni, W.; Parrinello, M., A Possible New Highly Stable Fulleride Cluster - $Li_{12}C_{60}$. *Chemical Physics Letters* **1992,** *198* (5), 472-477.
129. Prassides, K.; Christides, C.; Thomas, I. M.; Mizuki, J.; Tanigaki, K.; Hirosawa, I.; Ebbesen, T. W., Crystal Sctructure, Bonding, and Phase Transition of the Superconducting Na_2CsC_{60} Fulleride. *Science* **1994,** *263* (5149), 950-954.
130. Tasker, P. W., Stability of Ionic Crystal Surfaces. *Journal of Physics C-Solid State Physics* **1979,** *12* (22), 4977-4984.
131. Miller, J. D.; Hiskey, J. B., Electrokinetic behavior of fluorite as influenced by surface carbonation. *Journal of Colloid and Interface Science* **1972,** *41* (3), 567-573.
132. Khatib, R.; Backus, E. H. G.; Bonn, M.; Perez-Haro, M.-J.; Gaigeot, M.-P.; Sulpizi, M., Water orientation and hydrogen-bond structure at the fluorite/water interface. *Scientific Reports* **2016,** *6*, 24287.
133. Dimitrakopoulos, C. D.; Malenfant, P. R. L., Organic thin film transistors for large area electronics. *Advanced Materials* **2002,** *14* (2), 99-117.
134. Forrest, S. R., The path to ubiquitous and low-cost organic electronic appliances on plastic. *Nature* **2004,** *428* (6986), 911-918.
135. Rogers, J. A.; Someya, T.; Huang, Y. G., Materials and Mechanics for Stretchable Electronics. *Science* **2010,** *327* (5973), 1603-1607.
136. Crone, B.; Dodabalapur, A.; Lin, Y. Y.; Filas, R. W.; Bao, Z.; LaDuca, A.; Sarpeshkar, R.; Katz, H. E.; Li, W., Large-scale complementary integrated circuits based on organic transistors. *Nature* **2000,** *403* (6769), 521-523.
137. Wang, C. L.; Dong, H. L.; Hu, W. P.; Liu, Y. Q.; Zhu, D. B., Semiconducting pi-Conjugated Systems in Field-Effect Transistors: A Material Odyssey of Organic Electronics. *Chemical Reviews* **2012,** *112* (4), 2208-2267.
138. Feringa, B. L.; Jager, W. F.; Delange, B., Organic Materials for Reversible Optical Data Storage. *Tetrahedron* **1993,** *49* (37), 8267-8310.
139. Nalwa, H. S.; Kasai, H.; Okada, S.; Oikawa, H.; Matsuda, H.; Kakuta, A.; Mukoh, A.; Nakanishi, H., Fabrication of Organic Nanocrystals for Electronics and Photonics. *Advanced Materials* **1993,** *5* (10), 758-760.
140. Almohamad, A.; Smith, C. W.; Alsaffar, I. S.; Slifkin, M. A., Thin Organic Films for Electronics Applications. *Thin Solid Films* **1990,** *189* (1), 175-181.
141. Pethrick, R. A., Molecular Electronics - Electronic Applications of Organic Molecules and Polymers. *Interdisciplinary Science Reviews* **1987,** *12* (3), 278-284.
142. Thompson, B. C.; Frechet, J. M. J., Organic photovoltaics - Polymer-fullerene composite solar cells. *Angewandte Chemie International Edition* **2008,** *47* (1), 58-77.
143. Martin, R. E.; Diederich, F., Linear Monodisperse π-Conjugated Oligomers: Model Compounds for Polymers and More. *Angewandte Chemie International Edition* **1999,** *38* (10), 1350-1377.
144. Kanibolotsky, A. L.; Perepichka, I. F.; Skabara, P. J., Star-shaped [small pi]-conjugated oligomers and their applications in organic electronics and photonics. *Chemical Society Reviews* **2010,** *39* (7), 2695-2728.
145. Wegner, K. M. l. G., *Electronic materials : the oligomer approach*. Weinheim ; New York : Wiley-VCH 1998; Vol. xxvii.
146. Allard, S.; Forster, M.; Souharce, B.; Thiem, H.; Scherf, U., Organic semiconductors for solution-processable field-effect transistors (OFETs). *Angewandte Chemie International Edition* **2008,** *47* (22), 4070-4098.

147. Horowitz, G.; Hajlaoui, R.; Fichou, D.; El Kassmi, A., Gate voltage dependent mobility of oligothiophene field-effect transistors. *Journal of Applied Physics* **1999,** *85* (6), 3202-3206.
148. Torsi, L.; Lovinger, A. J.; Crone, B.; Someya, T.; Dodabalapur, A.; Katz, H. E.; Gelperin, A., Correlation between oligothiophene thin film transistor morphology and vapor responses. *Journal of Physical Chemistry B* **2002,** *106* (48), 12563-12568.
149. Horowitz, G.; Hajlaoui, M. E.; Hajlaoui, R., Temperature and gate voltage dependence of hole mobility in polycrystalline oligothiophene thin film transistors. *Journal of Applied Physics* **2000,** *87* (9), 4456-4463.
150. Koezuka, H.; Tsumura, A.; Ando, T., Field-effect transistor with polythiophene thin film. *Synthetic Metals* **1987,** *18* (1), 699-704.
151. Tsumura, A.; Koezuka, H.; Ando, T., Macromolecular electronic device: Field-effect transistor with a polythiophene thin film. *Applied Physics Letters* **1986,** *49* (18), 1210-1212.
152. Tamayo, A. B.; Dang, X. D.; Walker, B.; Seo, J.; Kent, T.; Nguyen, T. Q., A low band gap, solution processable oligothiophene with a dialkylated diketopyrrolopyrrole chromophore for use in bulk heterojunction solar cells. *Applied Physics Letters* **2009,** *94* (10), 3.
153. Ahmed, E.; Ren, G. Q.; Kim, F. S.; Hollenbeck, E. C.; Jenekhe, S. A., Design of New Electron Acceptor Materials for Organic Photovoltaics: Synthesis, Electron Transport, Photophysics, and Photovoltaic Properties of Oligothiophene-Functionalized Naphthalene Diimides. *Chemistry of Materials* **2011,** *23* (20), 4563-4577.
154. Shuttle, C. G.; Hamilton, R.; O'Regan, B. C.; Nelson, J.; Durrant, J. R., Charge-density-based analysis of the current–voltage response of polythiophene/fullerene photovoltaic devices. *Proceedings of the National Academy of Sciences* **2010,** *107* (38), 16448-16452.
155. Glenis, S.; Horowitz, G.; Tourillon, G.; Garnier, F., Electrochemically grown polythiophene and poly(3-methylthiophene) organic photovoltaic cells. *Thin Solid Films* **1984,** *111* (2), 93-103.
156. Fichou, D., *Handbook of oligo- and polythiophenes*. Weinheim ; New York : Wiley-VCH: 1999; Vol. xxiv.
157. Moser, A.; Salzmann, I.; Oehzelt, M.; Neuhold, A.; Flesch, H.-G.; Ivanco, J.; Pop, S.; Toader, T.; Zahn, D. R. T.; Smilgies, D.-M.; Resel, R., A disordered layered phase in thin films of sexithiophene. *Chemical Physics Letters* **2013,** *574*, 51-55.
158. Radziwon, M.; Madsen, M.; Balzer, F.; Resel, R.; Rubahn, H.-G., Growth of α-sexithiophene nanostructures on C60 thin film layers. *Thin Solid Films* **2014,** *558*, 165-169.
159. Ivanco, J.; Krenn, J. R.; Ramsey, M. G.; Netzer, F. P.; Haber, T.; Resel, R.; Haase, A.; Stadlober, B.; Jakopic, G., Sexithiophene films on clean and oxidized Si(111) surfaces: Growth and electronic structure. *Journal of Applied Physics* **2004,** *96* (5), 2716-2724.
160. Loi, M. A.; da Como, E.; Dinelli, F.; Murgia, M.; Zamboni, R.; Biscarini, F.; Muccini, M., Supramolecular organization in ultra-thin films of [alpha]-sexithiophene on silicon dioxide. *Nature Materials* **2005,** *4* (1), 81-85.
161. Koini, M.; Haber, T.; Berkebile, S.; Koller, G.; Ramsey, M. G.; Resel, R.; Oehzelt, M., Growth of sexithiophene crystals on Cu(1 1 0) and Cu(1 1 0)-(2×1)O stripe

phase—The influence of surface corrugation. *Journal of Crystal Growth* **2009,** *311* (5), 1364-1369.
162. Servet, B.; Horowitz, G.; Ries, S.; Lagorsse, O.; Alnot, P.; Yassar, A.; Deloffre, F.; Srivastava, P.; Hajlaoui, R., Polymorphism and Charge Transport in Vacuum-Evaporated Sexithiophene Films. *Chemistry of Materials* **1994,** *6* (10), 1809-1815.
163. Siegrist, T.; Fleming, R. M.; Haddon, R. C.; Laudise, R. A.; Lovinger, A. J.; Katz, H. E.; Bridenbaugh, P.; Davis, D. D., The crystal structure of the high-temperature polymorph of α–hexathienyl (α–6T/HT). *Journal of Materials Research* **1995,** *10* (9), 2170-2173.
164. Lorch, C.; Banerjee, R.; Frank, C.; Dieterle, J.; Hinderhofer, A.; Gerlach, A.; Schreiber, F., Growth of Competing Crystal Phases of α-Sexithiophene Studied by Real-Time in Situ X-ray Scattering. *The Journal of Physical Chemistry C* **2015,** *119* (1), 819-825.
165. O'Brien, D. B.; Massari, A. M., Experimental evidence for an optical interference model for vibrational sum frequency generation on multilayer organic thin film systems. I. Electric dipole approximation. *Journal of Chemical Physics* **2015,** *142* (2).
166. Kearns, P. M.; Sohrabpour, Z.; Massari, A. M., Frequency comb SFG: a new approach to multiplex detection. *Optical Express* **2016,** *24* (17), 19863-19870.
167. Wynands, D.; Erber, M.; Rentenberger, R.; Levichkova, M.; Walzer, K.; Eichhorn, K. J.; Stamm, M., Spectroscopic ellipsometry characterization of vacuum-deposited organic films for the application in organic solar cells. *Organic Electronics* **2012,** *13* (5), 885-893.
168. Furukawa, Y.; Akimoto, M.; Harada, I., Vibrational Key Bands and Electrical Conductivity of Polythiophene. *Synthetic Metals* **1987,** *18* (1-3), 151-156.
169. Horowitz, G.; Bachet, B.; Yassar, A.; Lang, P.; Demanze, F.; Fave, J. L.; Garnier, F., Growth and Characterization of Sexithiophene Single Crystals. *Chemistry of Materials* **1995,** *7* (7), 1337-1341.
170. Lang, P.; Hajlaoui, R.; Garnier, F.; Desbat, B.; Buffeteau, T.; Horowitz, G.; Yassar, A., IR Spectroscopy Evidence for a Substrate-dependent Organization of Sexithiophene Thin Films Vacuum-evaporated onto SiH/Si and SiO_2/Si. *Journal of Physical Chemistry* **1995,** *99* (15), 5492-5499.
171. Louarn, G.; Buisson, J. P.; Lefrant, S.; Fichou, D., Vibrational Studies of a Series of .alpha.-Oligothiophenes as Model Systems of Polythiophene. *The Journal of Physical Chemistry* **1995,** *99* (29), 11399-11404.
172. Brillante, A.; Bilotti, I.; Albonetti, C.; Moulin, J. F.; Stoliar, P.; Biscarini, F.; de Leeuw, D. M., Confocal Raman Spectroscopy of α-Sexithiophene: From Bulk Crystals to Field-Effect Transistors. *Advanced Functional Materials* **2007,** *17* (16), 3119-3127.
173. O'Brien, D. B. Solving the two-interface problem in vibrational sum frequency generation spectroscopy applied to multilayer thin film systems. University of Minnesota - Twin Cities, Minneapolis, 2014.
174. Loi, M. A.; Da Como, E.; Dinelli, F.; Murgia, M.; Zamboni, R.; Biscarini, F.; Muccini, M., Supramolecular organization in ultra-thin films of alpha-sexithiophene on silicon dioxide. *Nature Materials* **2005,** *4* (1), 81-85.
175. Servet, B.; Ries, S.; Trotel, M.; Alnot, P.; Horowitz, G.; Garneir, F., X-ray Determination of the Crystal Structure and Orientation of Vacuum-evaporated Sexithiophene Films. *Advanced Materials* **1993,** *5* (6), 461-464.

176. Lovinger, A. J.; Davis, D. D.; Ruel, R.; Torsi, L.; Dodabalapur, A.; Katz, H. E., Morphology of Alpha-Hexathienyl Thin Film Transistor Films. *Journal of Materials Research* **1995,** *10* (11), 2958-2962.
177. A.- L. Barabási, H. E. S., *Fractal Concepts in Surface Growth*. Cambridge University Press: Cambridge, UK, 1995.
178. Leclere, P.; Surin, M.; Viville, P.; Lazzaroni, R.; Kilbinger, A. F. M.; Henze, O.; Feast, W. J.; Cavallini, M.; Biscarini, F.; Schenning, A.; Meijer, E. W., About oligothiophene self-assembly: From aggregation in solution to solid-state nanostructures. *Chemistry of Materials* **2004,** *16* (23), 4452-4466.
179. Biscarini, F.; Greco, O.; Lauria, A.; Zamboni, R.; Taliani, C., Orientational ordering of domains in vacuum-grown oligomer thin films: A Scanning Force Microscopy study. *Molecular Crystals and Liquid Crystals Science and Technology-Section A-Molecular Crystals and Liquis Crystals* **1996,** *290*, 203-212.
180. Bohme, O.; Ziegler, C.; Gopel, W., Highly Ordered Ultra-thin Alpha-5-thiophene Films on SiO_2 and Si(100) + O(N_2O). *Synthetic Metals* **1994,** *67* (1-3), 87-92.
181. Tibbits, T. N.; Beutel, P.; Grave, M.; Karcher, C.; Oliva, E.; Siefer, G.; Wekkeli, A.; Schachtner, M.; Dimroth, F.; Bett, A. W. In *New efficiency frontiers with wafer-bonded multi-junction solar cells*, Proceedings of the 29th European Photovoltaic Solar Energy Conference and Exhibition, 2014; pp 1-4.
182. Hoppe, H.; Sariciftci, N. S., Organic solar cells: An overview. *Journal of Materials Research* **2004,** *19* (7), 1924-1945.
183. Tang, C. W.; Albrecht, A. C., Photovoltaic effects of metal–chlorophyll-a–metal sandwich cells. *The Journal of Chemical Physics* **1975,** *62* (6), 2139-2149.
184. Peumans, P.; Bulović, V.; Forrest, S. R., Efficient photon harvesting at high optical intensities in ultrathin organic double-heterostructure photovoltaic diodes. *Applied Physics Letters* **2000,** *76* (19), 2650-2652.
185. Roman, L. S.; Mammo, W.; Pettersson, L. A. A.; Andersson, M. R.; Inganäs, O., High Quantum Efficiency Polythiophene. *Advanced Materials* **1998,** *10* (10), 774-777.
186. Halls, J. J. M.; Friend, R. H., The photovoltaic effect in a poly(p-phenylenevinylene)/perylene heterojunction. *Synthetic Metals* **1997,** *85* (1), 1307-1308.
187. Anglin, T. C.; Speros, J. C.; Massari, A. M., Interfacial Ring Orientation in Polythiophene Field-Effect Transistors on Functionalized Dielectrics. *The Journal of Physical Chemistry C* **2011,** *115* (32), 16027-16036.
188. Sze, S. M., *Physics of Semiconductors*. John Wiley & Sons: New York, 1981.
189. Murgia, M.; Biscarini, F.; Cavallini, M.; Taliani, C.; Ruani, G., Intedigitated p-n junction: a route to improve the efficiency in organic photovoltaic cells. *Synthetic Metals* **2001,** *121* (1-3), 1533-1534.
190. Ruani, G.; Fontanini, C.; Murgia, M.; Taliani, C., Weak intrinsic charge transfer complexes: A new route for developing wide spectrum organic photovoltaic cells. *Journal of Chemical Physics* **2002,** *116* (4), 1713-1719.
191. Toccoli, T.; Boschetti, A.; Corradi, C.; Guerini, L.; Mazzola, M.; Iannotta, S., Co-deposition of phthalocyanines and fullerene by SuMBE: characterization and prototype devices. *Synthetic Metals* **2003,** *138* (1-2), 3-7.
192. Arkhipov, V. I.; Heremans, P.; Bassler, H., Why is exciton dissociation so efficient at the interface between a conjugated polymer and an electron acceptor? *Applied Physics Letters* **2003,** *82* (25), 4605-4607.

193. Pettersson, L. A. A.; Roman, L. S.; Inganäs, O., Modeling photocurrent action spectra of photovoltaic devices based on organic thin films. *Journal of Applied Physics* **1999,** *86* (1), 487-496.
194. Fichou, D.; Horowitz, G.; Xu, B.; Garnier, F., Low temperature optical absorption of polycrystalline thin films of α-quaterthiophene, α-sexithiophene and α-octithiophene, three model oligomers of polythiophene. *Synthetic Metals* **1992,** *48* (2), 167-179.
195. Méndez, H.; Heimel, G.; Winkler, S.; Frisch, J.; Opitz, A.; Sauer, K.; Wegner, B.; Oehzelt, M.; Röthel, C.; Duhm, S.; Többens, D.; Koch, N.; Salzmann, I., Charge-transfer crystallites as molecular electrical dopants. *Nature Communications* **2015,** *6*, 8560.
196. Wang, M.; Wang, X., P3HT/ZnO bulk-heterojunction solar cell sensitized by a perylene derivative. *Solar Energy Materials and Solar Cells* **2008,** *92* (7), 766-771.
197. Heidel, T. D.; Hochbaum, D.; Sussman, J. M.; Singh, V.; Bahlke, M. E.; Hiromi, I.; Lee, J.; Baldo, M. A., Reducing recombination losses in planar organic photovoltaic cells using multiple step charge separation. *Journal of Applied Physics* **2011,** *109* (10), 104502.
198. Yu, G.; Gao, J.; Hummelen, J. C.; Wudl, F.; Heeger, A. J., Polypmer Photovoltaic Cells - Enhanced Efficiencies via a Netwoek of Internal Donor-Acceptor Heterojunctions. *Science* **1995,** *270* (5243), 1789-1791.
199. Granstrom, M.; Petritsch, K.; Arias, A. C.; Lux, A.; Andersson, M. R.; Friend, R. H., Laminated fabrication of polymeric photovoltaic diodes. *Nature* **1998,** *395* (6699), 257-260.
200. Yang, F.; Shtein, M.; Forrest, S. R., Controlled growth of a molecular bulk heterojunction photovoltaic cell. *Nature Materials* **2005,** *4* (1), 37-41.
201. Ghani, F.; Bochukov, I.; Fostiropoulos, K.; Riegler, H., Hybrid solution/vacuum-processed bilayer heterojunction organic solar cells: Structural characterization and performance. *Thin Solid Films* **2012,** *525*, 177-181.
202. Wang, J. C.; Ren, X. C.; Shi, S. Q.; Leung, C. W.; Chan, P. K. L., Charge accumulation induced S-shape J–V curves in bilayer heterojunction organic solar cells. *Organic Electronics* **2011,** *12* (6), 880-885.
203. Xie, L.; Yoon, S.; Cho, Y. J.; Kim, K., Effective protection of sequential solution-processed polymer/fullerene bilayer solar cell against charge recombination and degradation. *Organic Electronics* **2015,** *25*, 212-218.